INTRAOPERATIVE FOURIER DOMAIN OPTICAL COHERENCE TOMOGRAPHY FOR MICROSURGERY GUIDANCE AND ASSESSMENT

by

Yong Huang

A dissertation submitted to The Johns Hopkins University in conformity with the requirements for the degree of Doctor of Philosophy.

Baltimore, Maryland

September, 2013

Abstract

In this dissertation, advanced high-speed Fourier domain optical coherence tomography (FD-OCT)systems were investigated and developed. Several real-time, high-resolution functional Spectral-domain OCT (SD-OCT) systems capable of imaging and sensing blood flow and motion were designed and developed.

The system were designed particularly for microsurgery guidance and assessment. The systems were tested for their ability to assessing microvascular anastomosis and vulnerable plaque development.

An all fiber-optic common-path optical coherence tomography (CP-OCT) system capable of measuring high-resolution optical distances, was built and integrated into different imaging modalities. First, a novel non-contact accurate *in-vitro* intra-ocular lens power measurement method was proposed and validated based on CP-OCT. Second, CP-OCT was integrated with a fiber bundle based confocal microscope to achieve motion-compensated imaging. Distance between the probe and imaged target was monitored by the CP-OCT system in real-time.The distance signal from the CP-OCT system was routed to a high speed, high resolution linear motor to

compensate for the axial motion of the sample in a closed-loop control. Finally a motion-compensated hand-held common-path Fourier domain optical coherence tomography probe was developed for image-guided intervention. Both phantom and *ex vivo* models were used to test and evaluate the probe.

As the data acquisition speed of current OCT systems continue to increase, the means to process the data in real-time are in critically needed. Previous graphics processing unit accelerated OCT signal processing methods have shown their potential to achieve real-time imaging. In this dissertation, algorithms to perform real-time reference A-line subtraction and saturation artifact removal were proposed, realized and integrated into previously developed FD-OCT system CPU-GPU heterogeneous structure. Fourier domain phase resolved Doppler OCT (PRDOCT) system capable of real-time simultaneous structure and flow imaging based on dual GPUs was also developed and implemented.

Finally, systematic experiments were conducted to validate the system for surgical applications. FD-OCT system was used to detect atherosclerotic plaque and drug efficiency test in mouse model. Application of PRDOCT for both suture and cuff based microvascular anastomosis guidance and assessment was extensively stuided in rodent model.

ABSTRACT

Thesis Advisor:	Prof.Dr. Jin U.Kang	(Dissertation Reader)
Committee Members:	Prof.Dr. Amy Foster	(Dissertation Reader)
	Prof.Dr. Xingde Li	
	Prof.Dr. Mark Foster	

Acknowledgments

First of all, I owe my deepest gratitude to my advisor, Dr.Jin U.Kang for giving me the opportunity to work on such an exciting project at Hopkins. His patient guidance helped me obtain a sound understanding of engineering research and cultivated me to become highly self-motivated and independent. I am grateful to his mentorship, appreciation, understanding and encouragement in the past four years.

I am sincerely grateful to my dissertation committee members, Dr. Amy Foster , Dr. Mark Foster and Dr. Xingde Li for their generous help on my research. Special thanks to Dr. Amy Foster for her constructive reviews on my dissertation. Thanks to Dr. Trac Tran for being my proposal committee member. Special thanks to Dr. Xinge Li for also being my GBO committee member. As another great master in the OCT research at Hopkins, he sets a model for us junior researchers to follow.

I would also like to thank Dr. Emad Boctor, Dr. Iulian, Dr. Peter Gehlbach for being my GBO committee members. Besides I would like to express my special thanks to all of my collaborators. Without their contribution, all these results couldn't have been possible.

ACKNOWLEDGMENTS

I also deeply appreciate the help and contributions from my colleagues who have educated and encouraged me a lot: Dr. Russell Taylor, Dr.Jae Ho Han, Dr. Xuan Liu, Dr. Kang Zhang, Dr. Yi Yang, Dr. Mingtao Zhao, Dr. Cheol Song, Dr. Beibei Zhang, Mr. Ching Lin, Mr. Jaepyeong Cha, Mr. Gyeongwoo Cheon, Mr. Chuyang Ye and Mr. Jianqiao Feng in Johns Hopkins University. Dr.Gustavo Pradilla, Dr. Betty Tyler and Mr. Robert Wicks, Miss Lee Hwang in Johns Hopkins School of Medicine; Dr. Ilko Ilev, Dr.Do-Hyun Kim in U.S. Food and Drug Administration.

Finally I would like to thank all my family members for their support and encouragement all over the years.

Dedication

To my family,mentors and friends!

Contents

List of Tables

List of Figures

Chapter 1

Introduction

1.1 Intraoperative Fourier Domain Optical Coherence Tomography for Microsurgery

Generally surgeries requiring the use of operating microscope are termed microsurgeries. Microsurgeries are typically performed in small, confined and not fully accessible spaces. Microsurgeries involving delicate structures, such as retina and microvasculature, such surgeries pose a very challenging surgical environment for surgeons. Access and visualization difficulties are further magnified by the small dimensions, on the order of tens or hundreds of microns.. Microsurgical technique currently involves visualization of the surgical target in the (X,Y) plane on the tissue surface

using a high quality binocular surgical microscope. The ability to view critical parts of a tissue and to work in micron proximity to fragile tissue surfaces requires excellent visibility, precision micro-instruments, and a highly skilled surgeon. At present the surgeon must function within the human physiological limits to visualize targets, guide microsurgical tools and execute all surgical objectives. Anastomosis of small blood vessels (typically with diameter less than 1 mm),for example, a surgical microscope is used to increase the visualization of vessel for the surgeon to accurately place six to eight sutures along the vessel or nerve wall circumferentially. These techniques enable transfer of a tissue from one part of the body to another and re-attachment of injured parts. Intraoperative surgical guidance using a surigcal imaging modality that provides an in-depth view and three-dimensional (3D) imaging can potentially improve outcome.

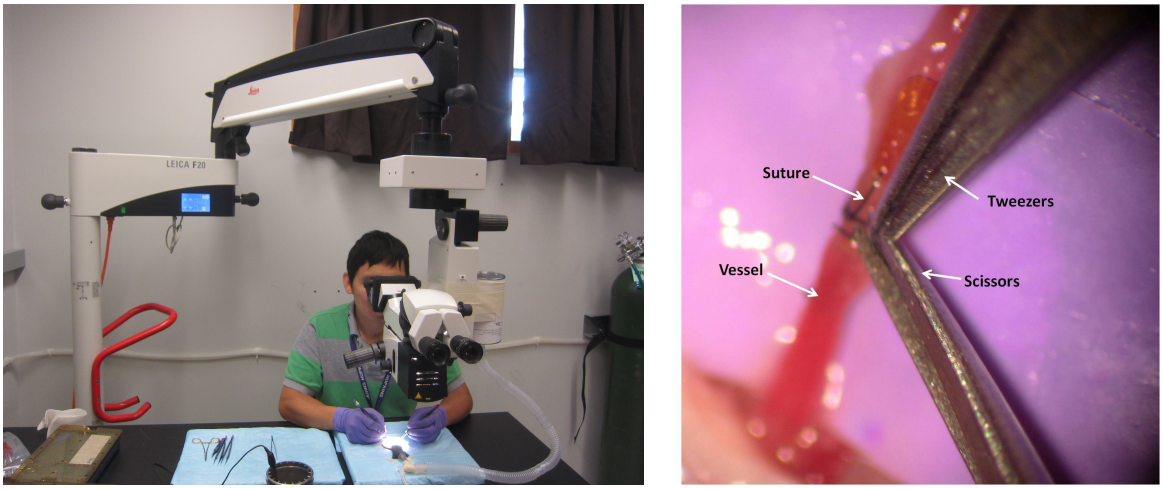

(A) (B)

Figure 1.1: (A)Surgeon performing microvascular anastomosis with surgical microscope; (B) Typical microscope view of the anastomosis procedure

Optical coherence tomography(OCT) is a well-established, noninvasive optical imaging technology that can provide high-speed, high-resolution, three-dimensional images of biological samples. Since its invention in the early 1990s, OCT has been widely used for diagnosis, therapy monitoring, and ranging [1]. The ability of OCT to view anatomic relationships in three dimensions and in high resolution has made intraoperative use of OCT a natural application for this imaging system [2]. Clinically, the intraoperative period starts when the patient is transferred to the operating room bed and ends with the transfer of a patient to the post anesthesia care unit (PACU). The operation is performed at this stage. In addition to its role in diagnosis and management of clinical disease, OCT imaging has found an important role in preoperative surgical planning and our understandings of postoperative healing processes. OCT imaging has enable visualization of anatomic pathology difficult to detect clinically.

OCT has several advantages over other well-developed imaging modalities, such as X-ray computed tomography (CT), magnetic resonance imaging (MRI) and ultrasound sonogram (US). These established modalities have been widely utilized for image guided intervention (IGI), from gathering preoperative data, generally in the form of tomographic images to accounting for differences between preoperative data and the intra-operative reality [3].

Table 1.1 compared OCT with other imaging modalities in term of the spatial resolution, imaging capabilities and image modes etc. As listed in Table 1.1, OCT is a promising solution that offers micron level resolution and 3D imaging capability.

Table 1.1: Comparison of commonly used IGI modalities with OCT

Imaging Modality	**MRI**	**CT**	**US**	**OCT**
Spatial Resolution	1-3 mm	0.4-3 mm	0.5-1 mm	1-10 μm
Imaging Modes	2D&3D	2D&3D	1D&2D&3D	1D&2D&3D
Real-time	Limited	Limited	Yes	Yes
Imaging Range	Whole Body	Whole Body	10-20 cm	1-10 mm
Non-Contact	Yes	Yes	No	Yes

Although the image depth of OCT is small compared to other modalities, the depth is sufficient for providing guidance and assessment for microsurgery since the size of critical surgical site of a microsurgery is usually around several millimeters at most. MRI and CT having resolution around millimeter and slow imaging speed prohibits their application in microsurgery. OCT is analogous to ultrasound sonogram. Instead of using light and detect the echo back in US, near infrared light is used and interferometry method is applied to detect the back scattering light. The advantage of light is that the acquired images exhibit much higher resolution compared to US although OCT exhibit decreased imaging depth. There are three different imaging modes in OCT, A-scan, B-scan and C-scan as shown in Figure 1.1.

Early OCT instruments used a low-coherence light source and an interferometer with a scanning reference delay arm. This method of low-coherence interferometry using as time domain scanning iscalled time domain OCT (TD-OCT) [4]. However, it is also possible to perform detection in the Fourier domain by measuring the interference spectrum. This concept was first proposed by Fercher et al. in 1995 [5]. There are two types of Fourier domain detection. One is known as spectral domain OCT (SD-OCT) and the other is known as swept source OCT (SS-OCT). These

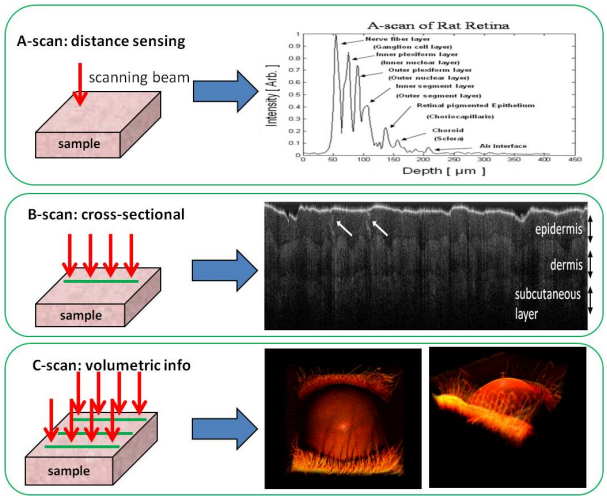

Figure 1.2: Fundamental imaging modes of OCT

two system configuration will be explained in detail in following chapters. With the advantage of sensitivity and imaging speed over TD-OCT, FD-OCT boosted a lot more interesting applications, intraoperative imaging being one of them. From imaging speed of hundreds of A-scans/s in TD-OCT [6] to over 100,000 A-scans/s [7–9] and even Mega-A-scans/s [10, 11] in FD-OCT, real-time, three-dimensional surgical intervention has become more and more practical and powerful. Meanwhile, functionalities of OCT have also been enriched over time, such as polarization sensitive OCT (PS-OCT) and phase resolved Doppler OCT to visualize tissue microcirculation (PRDOCT). Ophthalmology has seen the major focus of OCT developments over the years, from hand-held OCT to microscope-mounted OCT and from retinal imaging to anterior segment imaging.

We are currently in the midst of a revolution in surgical imaging. Ultrahigh speed real-time three-dimensional OCT imaging has provided valuable information

for surgical operation and shown great potential. Continued effort will be made toward seamless integration of real-time intraoperative imaging which will undoubtedly revolutionize surgical practice within the next few years.

1.2 Real-time FD-OCT based on GPU

For intraoperative imaging, fast data acquisition, real-time signal processing and visualization are important are important attributes. Visualization is one of the primary interfaces between an interventionalist and his/her patient. This interface is the result of final integration of several distinct data streams. A real-time system must meet two strict constraints: first it has processes that are guaranteed to finish in a given time; second, the processes are interruptible. By meeting these two contraints, a real-time system can schedule the execution of processes to ensure that certain actions will be executed with a given periodicity subject to a limited tolerance [3].

With the ever increasing speed of FDOCT system due to faster swept laser and faster line-scan cameras, FDOCT significantly increased the computational burden of the image reconstruction, as an inverse Fourier transform needs to be applied to each line sampled and even wavelength to wavenumber re-sampling need to be performed to before FFT for most SD-OCT systems. Most of current FD-OCT systems operate under the “post-processing“ mode, which means large volume data was acquired and saved in computer hardware first, a separate signal processing will render the result

out later. Like ultrasound, optical imaging can output the acquired data directly, but real-time signal processing requires sophisticated computer hardware. Several parallel computing methods have been applied to improve the A-scan data processing rate, such as field-programmable gate array (FPGA) [12, 13] and multi-core CPU parallel processing [14, 15]. Compared to FPGA and multi-core processing methods, GPU acceleration is more cost-effective in terms of price/performance ratio and convenience of system integration.

Constant demand for greater realism in computer games has driven the evolution of powerful GPUs. During the past few decades, the computational performance of GPUs has increased much more quickly than that of central processing unit (CPUs). Theoretical performance of the GPU can be tens of times better than that of CPU based on its single instruction multiple data (SIMD) design. While both CPUs and GPUs can manage thousands of threads concurrently via time-slicing, a modern CPU can actually make progress on only 4-12 in parallel compared to over a thousand threads at a time in GPU. The performance of GPU implementations greatly depends on how easy it is to make a parallel adaptation of a given algorithm. FD-OCT signal processing are massively parallel by nature as each A-scan within a frame could be processed independently. But not all the algorithms are suited for parallel implementation. In many cases a hybrid CPU-GPU implementation is necessary and yields the best performance. The evolution of GPU programming models and available tools have greatly simplified the GPU based software development. At the

early stage GPUs could only be programmed through computer graphics APIs, such as the open graphics language (OpenGL) or DirectX. The use of GPUs for general purpose computing (GPGPU) has been popular since 2007. The release of the computed unified device architecture (CUDA)programming language made using Nvidia GPUs for more general purpose calculations much easier. Significant computational gains compared to optimized CPU algorithms were reported due to combination of a higher theoretical performance and an easy programming language. However, CUDA can only be used with Nvidia GPUs. The open computing language (OpenCL) is another alternative, which can be used for programming of any hardware, sucha s AMD GPUs, CPUs and FPGA.

Table 1.2: Summary of GPU accelerated FD-OCT

Work	**Authors and Year**
Linear-k system; 2048x1000 (28 fps)	Watanabe and Itagaki 2009 [16]
Nonlinear-k system & 3D visualization	Zhang and Kang 2010 [17]
Nonlinear-k re-sampling	Van der Jeught and Podoleanu 2010 [18]
Zero-filling re-sampling full-range OCT	Watanabe and Koseki 2010 [19]
Non-uniform FFT & full range OCT	Zhang and Kang 2010 [20, 21]
Nonlinear-k 1024x1836 (524 kHz line rate)	Rasakanthan and Tomlins 2011 [22]
Speckle variance OCT	Lee and Yang 2012 [23]
Dispersion encoded full range OCT	Wang and Povazay 2012 [24]
Reference Fixed Pattern Removal	Huang and Kang 2012 [25]
	Watanabe 2012 [26]
2D Doppler OCT	Jeong and Kim 2012 [27]
3D and 4D Doppler OCT	Huang and Kang 2012 [28]
	Sylwestrzak and Targowski 2012 [29]
Megahertz OCT (23 volumes/s, 1024x256x200)	Jian and Sarunic 2013 [30]

GPUs have been adopted rapidly and widely to perform signal processing for FDOCT since 2009. Table 1.2 summarizes all the graphics processing unit related work to accelerate structural and functional imaging of FD-OCT system. From basic

inverse Fourier transform to zero padded interpolation, from structure imaging to flow imaging, Real-time FD-OCT became possible with the aid of GPUs.

In this dissertation cutting-edge CPU-GPU hybrid computing was used to develop ultra-high speed FD-OCT systems capable of real-time data acquisition and processing. Figure 1.3 shows one of the GPUs, Nvidia Geforce GTX 590 graphics card, which has a PCIE-x16 interface, 32-stream multiprocessors with 1024 cores at 1.21 GHz and 3 GB graphics memory, utilized in our system. For the current stage of research, all the GPUs used are Fermi structure based. In future work, advanced Kepler structure based GPUs for more complicated signal processing and image processing are planned. The main contribution of this dissertation consists of real-time reference A-line fixed pattern removal [25] and simultaneous structure and flow imaging [28] to the ever evolving FD-OCT system based on CPU-GPU heterogeneous structure.

Figure 1.3: A Nvidia Geforce GTX 590 as a graphics card manufactured by EVGA

1.3 Organization of Dissertation

This dissertation will present advanced FD-OCT technologies and their applications in medicine. Chapter 2 reviews the fundamental OCT technology principles and signal processing. Chapter 3 presents fixed pattern noise remove and real-time Doppler OCT based on previous GPU accelerated reconstruction and visualization technologies in our lab. Chapter 4 presents the applications of common-path OCT (CP-OCT) for sensing, distance ranging and imaging. Chapter 5 validates GPU-based real-time FD-OCT technologies atherosclerotic plaque and drug efficiency test. Chapter 6 presents PRDOCT guided and assessed microvascular anastomosis in rodent model. Chapter 7 summarizes the dissertation and proposes the future directions.

Chapter 2

Principles of Optical Coherence Tomography

Successful OCT applications are not possible without the in depth knowledge of optics, fiber optics, light-tissue interactions. In this chapter three different aspects of OCT technology are reviewed. Physical properties of coherence and interferometry, light propagation in fiber, dispersion, light scattering and absorption in tissue are discussed and detailed. These are followed by the introduction of general OCT signal processing from the perspective of an imaging system developer.

2.1 Fiber Optics

While fiber optics is the foundation for modern long-distance communication. Charles K.Kang was awarded the Nobel Prize in Physics in 2009 for his groundbreaking achievements concerning the transmission of light in fibers for optical communication. it is also the key techonology for OCT. Without optical fibers, OCT systems would have been much larger and more complicated and less practical than current ones. Free-space OCTs would have put huge limitation in the OCT applications. Fundamental theories about fiber optics will be introduced in this section with an emphasis on the application of fiber optics in OCT.

2.1.1 Light propagation in fiber

A typical optical fiber structure is shown in Figure 2.1(A). The core part is made of highly purified SiO_2 doped with small amount of dopants, such as GeO_2, that increase the refractive index of the core. Surrounding the core part is the cladding region, which is doped with dopants, such as B_2O_3 and F to reduce the refractive index [31]. The outermost layer is the jacket layer that increases the mechanical strength and flexibility of the fiber. Take the 780-HP fiber used for 800 nm band OCT system from Thorlabs.Inc for example, the cladding diameter is 125 μm, and the core diameter is 4.4 μm.

Refractive index of the cladding is smaller than that of the core to confine the light

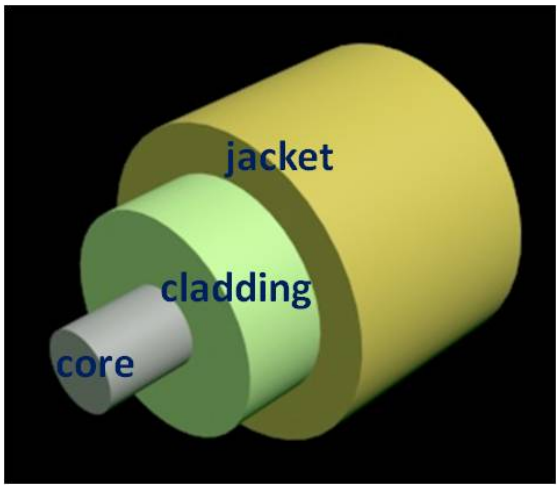

Figure 2.1: Cross-sectional view of an optical fiber

within the fiber. Shown in Figure 2.2 is the refractive index profile of a step-index fiber, $n_1 > n_0$. The material in the core and cladding area is uniform. Here assume the core diameter is $2a$ and the cladding diameter is $2b$. However, the refractive index distribution of the core area can also be gradient, such as Gaussian distribution, the variation is controlled through the doping processing. For the simplicity of analysis, we assume the radius of the cladding layer is infinity.

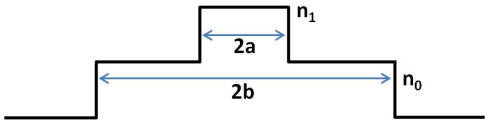

Figure 2.2: Refractive index profile of a step-index fiber

Numerical aperture is an important parameter that describes the fiber property. For a step-index fiber, light that can be transmitted through the fiber encounters total internal reflection at the core and cladding boundary. Choose one such light, as

shown in Figure 2.3, we can have

$$n_1 \sin\psi = n_0 \tag{2.1}$$

At the entrance surface, we have

$$\sin(\theta_0) = n_1 \cos\psi \tag{2.2}$$

θ_0 is the critical angle. From Eq.2.16 and Eq.2.17 we can get the numerical aperture,

$$N.A. \stackrel{\text{def}}{=} \sin\theta_0 = \sqrt{n_1^2 - n_0^2} \tag{2.3}$$

Numerical aperture of the 780-HP fiber is 0.13, which corresponds to a critical angle of 7.5°.

Optical fibers are characterized by their structure and their transmission properties. Optical fibers can be classified into two types: single mode fibers and multimode fibers. The main difference is their core diameter. The normalized frequency V is a dimensionless parameter that relates in a very useful manner the core radius a, the numerical aperture and the operating wavelength ;

$$V = \frac{2\pi a}{\lambda} N.A. \tag{2.4}$$

For a step index fiber, the mode volume is given by $\frac{4V^2}{\pi^2}$. Single mode operation requires that $V < 2.405$, which is the first root of the Bessel function J_0. For OCT imaging, single mode fiber is chose for the following advantage of SMF over the multimode fiber. There is no modal dispersion when the light propagates in the SMF. In addition the output of the single mode fiber can be focused as a small Gaussian spot.

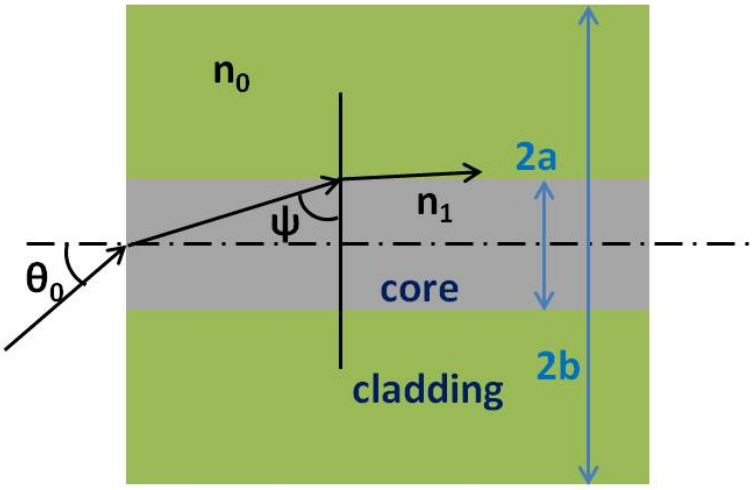

Figure 2.3: Numerical Aperture of step-index fiber

Another advantage of modern silica fiber is that it is of extreme low loss. The main reasons for light attenuation are intrinsic attenuation and extrinsic attenuation. The intrinsic attenuation is caused by the absorption band formed by electrons excitation, molecule vibration, rotation. It is unavoidable physical effect. However, for near infrared band, there attenuation is low. The other is extrinsic attenuation, which is caused mainly by Rayleigh scattering and Mie scattering. Modern fabrication process can reduce the Mie scattering well by making fibers really uniform.

There is a attenuation peak at 1.4 μm due to the residual absorption of OH vibration. Typical attenuation coefficient for 1310 nm is 0.4 dB/km, and 0.2 dB/km for 1550 nm. It goes higher for 800 nm to 950 nm band, which is usually less than 3.5 dB/km, considering the total length used for an OCT system usually less than several meters, the fiber loss is negligible.

2.1.2 Dispersion in Fiber

Light pulse travels through fibers is typically not monochromatic. It covers a certain range of wavelengths. Light of different wavelengths travels at different speed, which will cause the broadening of the pulse. This is dispersion. The refractive index of the fiber and propagation constant are functions of wavelength. Group velocity dispersion (GVD) is the dispersion caused by the group velocity difference of all the frequency components. Expand the propagation constant β near the center frequency ω_0, in a Taylor series, leads to Eq.2.20.

$$\beta(\omega_0) = \beta_0 + \frac{d\beta}{d\omega}|_{\omega_0}(\omega-\omega_0) + \frac{1}{2}\frac{d^2\beta}{d\omega^2}|_{\omega_0}(\omega-\omega_0)^2 = \beta_0+\beta_1(\omega-\omega_0)+0.5\beta_2(\omega-\omega_0)^2 \quad (2.5)$$

The second term in Eq.2.20 is the inverse of the group velocity, defined as:

$$v_g = \frac{1}{(\frac{d\beta}{d\omega}|_{\omega_0})} \quad (2.6)$$

The third term in Eq.2.20 is the GVD term. β_2 is named GVD coefficient. Assume the frequency bandwidth of a pulse is $\Delta\omega$, after propagation through a fiber of length L, the broadening $\Delta\tau$ is

$$\Delta\tau = \frac{d\tau}{d\omega}\Delta\omega = \frac{d}{d\omega}(\frac{L}{\upsilon_g})\Delta\omega = L\frac{d^2\beta}{d\omega^2}\Delta\omega = L\beta_2\Delta\omega. \tag{2.7}$$

Dispersion can be divided into material dispersion and waveguide dispersion. Material dispersion is caused by the dependence of refractive index of material on the wavelength. Waveguide dispersion is caused by the light field distribution over the core and cladding area. Light travels slower in the high refractive index core area than in the low refractive index cladding area.

Dispersion needs to be properly taken care of in the OCT imaging, as mismatch of the dispersion from two arms will cause signal degradation, which will be discussed in the signal procesing of OCT section in this chapter.

2.2 Optical Coherence and Interferometry

Optical coherence theory is a classical optics topic that has been studied extensively over the years. Even though much of the theory is beyond the level of this thesis, some of the basic ideas are nevertheless introduced.

Coherence effects can be divided into two classifications, temporal and spatial. The former relates directly to the finite bandwidth of the source, the latter to its finite extent in space. In effect, the coherence time is the temporal interval over which we can reasonably predict the phase of the lightwave at a given point in space.

2.2.1 The Mutual Coherence Function and the Degree of Coherence

Optical light field could be represented as a complex function. Overlooking the polarization effects, light field can be treated as a scalar. The disturbances at two points in space S_1 and S_2 can be described as $\tilde{E}_1(t)$ and $\tilde{E}_2(t)$. Assuming the wave field is statistically stationary, Equation 2.1 is referred to as the mutual coherence function of the light field at S_1 and S_2. Here τ is the time difference of the light arriving at the positions.

$$\tilde{\Gamma}_{12}(\tau) =< \tilde{E}_1(t+\tau)\tilde{E}_2^*(t) >_T \tag{2.8}$$

$< \cdots >_T$ indicates averaging operation over observation time T. Normalized form of the mutual coherence function is defined as

$$\tilde{\gamma}_{12}(\tau) = \frac{\tilde{\Gamma}_{12}(\tau)}{\sqrt{\Gamma_{11}(0)\Gamma_{22}(0)}} = \frac{< \tilde{E}_1(t+\tau)\tilde{E}_2^*(t) >_T}{\sqrt{< |\tilde{E}_1|^2 >< |\tilde{E}_2|^2 >}} \tag{2.9}$$

and it's defined as the complex degree of coherence.

$$\begin{aligned} |\tilde{\gamma}_{12}| &= 1 \quad \text{coherent limit} \\ |\tilde{\gamma}_{12}| &= 0 \quad \text{incoherent limit} \\ 0 < |\tilde{\gamma}_{12}| &< 1 \quad \text{partial coherence} \end{aligned} \tag{2.10}$$

In situations where S_1 and S_2 coincide, such as at a single detector, $\tilde{\gamma}_{11}(\tau)$ is referred to as complex degree of temporal coherence at certain point for two instances of time separated by an interval τ. Analogously $\tilde{\gamma}_{12}(0)$ is referred to as complex degree of spatial coherence of two points at the same instant in time.

Coherence time $\Delta\tau$ can be defined as the square root of normalized square modulus of $\tilde{\Gamma}_{11}(\tau)$,

$$(\Delta\tau)^2 = \frac{\int_{-\infty}^{\infty} \tau^2 |\tilde{\Gamma}_{11}(\tau)|^2 d\tau}{\int_{-\infty}^{\infty} |\tilde{\Gamma}_{11}(\tau)|^2 d\tau} \tag{2.11}$$

Assume power spectrum of at certain point is $S(\nu)$, the effective spectrum bandwidth $\Delta\nu$ can be defined as

$$(\Delta\nu)^2 = \frac{\int_0^{\infty} (\nu - \bar{\nu})^2 S^2(\nu) d\nu}{\int_0^{\infty} S^2(\nu) d\nu}, \bar{\nu} = \frac{\int_0^{\infty} \nu S^2(\nu) d\nu}{\int_0^{\infty} S^2(\nu) d\nu} \tag{2.12}$$

$$\bar{\nu} = \frac{\int_0^{\infty} \nu S^2(\nu) d\nu}{\int_0^{\infty} S^2(\nu) d\nu} \tag{2.13}$$

Relationship between self-coherence function and spectral density can be expressed

as

$$\Gamma_{11}(\tau) =< \tilde{E}(t+\tau)\tilde{E}(t)^* >= 4\int_0^\infty S(\nu)e^{-2\pi\nu\tau i}d\tau \tag{2.14}$$

From Eq.2.4 to Eq.2.8, it can be proven that the relationship between coherence time $\Delta\tau$ and effective spectrum bandwidth $\Delta\nu$

$$\Delta\tau\Delta\nu \geq \frac{1}{4\pi} \tag{2.15}$$

Generally $\Delta\tau$ is inverse proportional to $\Delta\nu$, and corresponding coherence length is defined as

$$l_c = c\Delta\tau \approx \frac{c}{\Delta\nu} = \frac{\bar{\lambda}_0^2}{\Delta\lambda_0} \tag{2.16}$$

For OCT, A broadband light source is usually used for imaging to achieve short coherence length thus high resolution, which be revealed soon in this chapter.

2.2.2 Interferometry

Optical interference corresponds to the interaction of two or more light waves yielding a resultant irradiance that deviates from the sum of the component irradiances. For the sake of simplicity, considering two point sources, S_1 and S_2, emitting monochromatic waves of the same frequency in a homogeneous medium. Their separation a be much greater than the λ. The observation point P is located far away from both sources, so that the wavefronts of both sources are planar. Considering

only linearly polarized waves currently,

$$\vec{\boldsymbol{E}}_1(\vec{\boldsymbol{r}}, t) = \vec{\boldsymbol{A}}_{01} \cos(\vec{\boldsymbol{k}}_1 \cdot \vec{r} - \omega t + \varepsilon_1) \tag{2.17}$$

$$\vec{\boldsymbol{E}}_2(\vec{\boldsymbol{r}}, t) = \vec{\boldsymbol{A}}_{02} \cos(\vec{\boldsymbol{k}}_2 \cdot \vec{r} - \omega t + \varepsilon_2) \tag{2.18}$$

Irradiance at P is given by

$$I = \epsilon \upsilon < \vec{\boldsymbol{E}}^{\mathbf{2}} >_T = \epsilon \upsilon < (\vec{\boldsymbol{E}}_1 + \vec{\boldsymbol{E}}_2) \cdot (\vec{\boldsymbol{E}}_1 + \vec{\boldsymbol{E}}_2) >_T \tag{2.19}$$

$$I = I_1 + I_2 + I_{12}, I_1 = < \vec{\boldsymbol{E}}_1^2 >_T, I_2 = < \vec{\boldsymbol{E}}_2^2 >_T, I_{12} = 2 < \vec{\boldsymbol{E}}_1 \cdot \vec{\boldsymbol{E}}_2 >_T \tag{2.20}$$

I_{12} is known as the interference term. It can be deduced that,

$$I_{12} = \vec{\boldsymbol{A}}_{01} \cdot \vec{\boldsymbol{A}}_{02} \cos(\delta), \delta = \vec{\boldsymbol{k}}_1 \cdot \boldsymbol{r} - \vec{\boldsymbol{k}}_2 \cdot \boldsymbol{r} + \varepsilon_1 - \varepsilon_2 \tag{2.21}$$

From Eq.2.14, we can see that there is no interference if $\vec{\boldsymbol{A}}_{01}$ is perpendicular to $\vec{\boldsymbol{A}}_{02}$. There are two other conditions to met. First, two beams must have very nearly the same frequency. Second, phase difference between two sources needs to remain constant. Such sources are coherent.

The main problem in producing interference is the sources must be coherent. Inde-

pendent, adequately coherent sources other than modern lasers don't exist. There are two methods to produce interferometers: wavefront-splitting and amplitude-splitting. Famous Young's Experiment and Fresnel double prism utilizes wavefront-splitting method to create coherence sources. There are a good number of amplitude-splitting interferometers that uses mirrors and beamsplitters to create coherent sources. I am going to review several of such in detail as they are closely related to OCT technology.

2.2.2.1 Interferometers

Michelson interferometer is by far the best known and historically the most important. Figure 2.4 illustrates the basic configuration of a Michelson interferometer. Most of optical coherence tomography are essentially Michelson interferometer based. Lights coming out of the light source is divided into two arms by a beam-splitter and reflected back and united again at the detector surface. The optical path length (OPL) difference between these two arms cause certain phase delay thus create interference.

Mach-Zehnder interferometer is shown in Figure 2.5. Output of a coherent light source, is split into two beams by the first beam splitter. These two beams combine together at the second beam splitter and interfere with each other at the detector. According to Eq.2.14, assume the optical path length difference is ΔL, the interference term is $\cos(k\Delta L)$. When the wavelength of the light source is swept over a certain

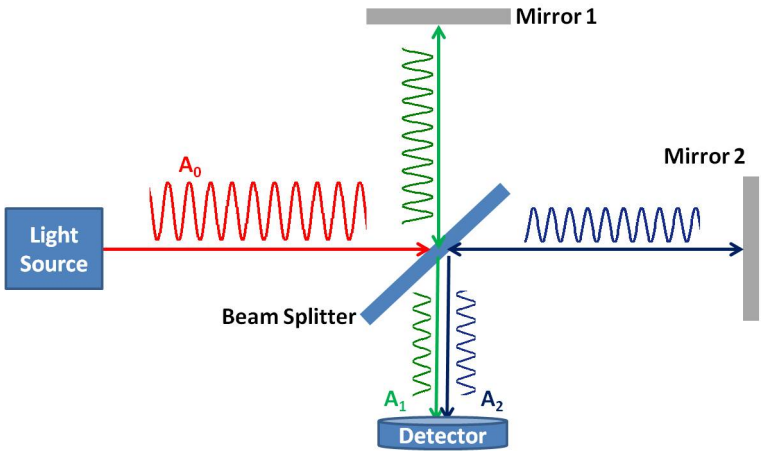

Figure 2.4: Michelson interferometer

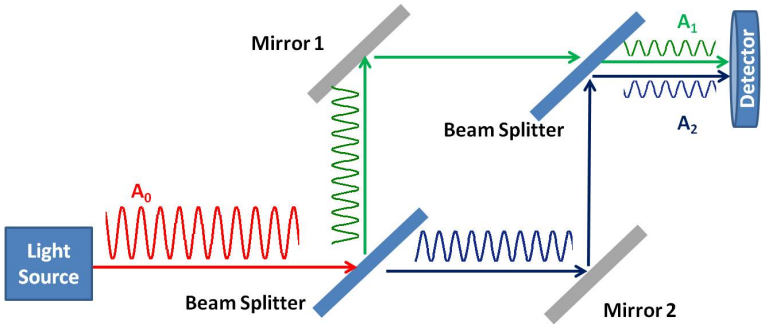

Figure 2.5: Mach-Zehnder interferometer

range, the zero points of the interference term corresponds to

$$k_m \Delta L = \frac{\pi}{2} + m\pi, m = 0, \pm 1, \pm 2, \cdots \tag{2.22}$$

The spacing between each k_m is $\Delta k = \frac{\pi}{\Delta L}$, which is a constant and is used for most swept source based OCT (SS-OCT) to provide equal-spaced sampling signal clock [**?**].

Figure 2.6 illustrates the schematic of Fizeau interferometer. It is commonly used for measuring the shape an optical surface. Light reflected from the investigated sur-

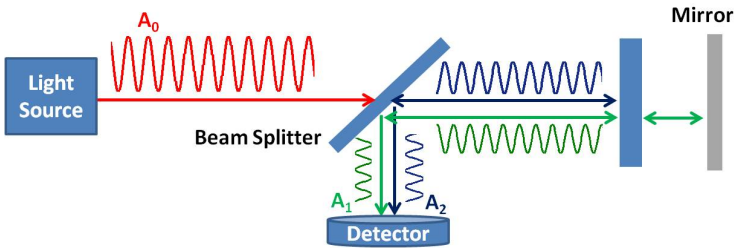

Figure 2.6: Fizeau interferometer

face interferes with the light coming from a standard reference piece. The key feature of Fizeau interferometer is that two interfered light beams share the same optical path, which serves as the basic idea for common-path optical coherence tomography (CP-OCT). Detailed description of CP-OCT will be provided in later chapters.

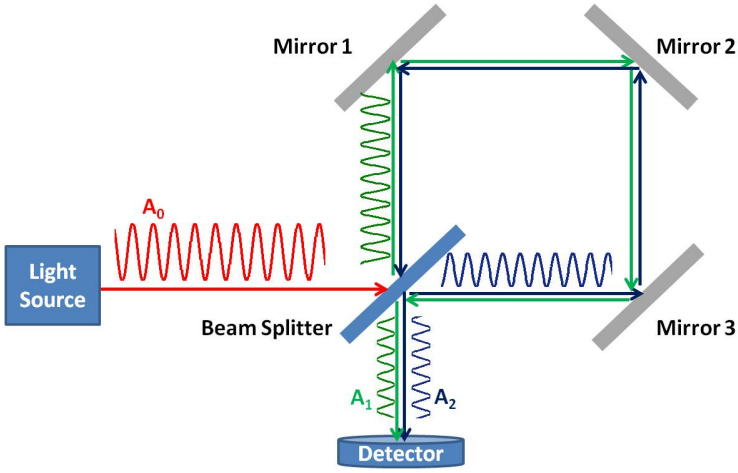

Figure 2.7: Sagnac interferometer

Sagnac interferometer, shown in Figure 2.7, can be used for rotation sensing, such as a gyroscope. Rotation of the interferometer will cause certain phase difference between two beams that travel in opposite directions inside the interferometer. For rotation sensing, the light source needs to be of high power and have very short

coherence length, which is very similar to the requirement for OCT light source.

2.3 Principles of OCT

Figure 2.8illustrates the schematic of a Michelson interferometer based OCT system. Light coming out of a broadband light source is divided into two arms: one is the reference arm with pathlength measured from the beamsplitter z_R; the other is the sample arm with pathlength measured from the beamsplitter z_S. The sample under investigation interrogation is characterized by its depth-dependent electric field reflectively profile along the sample beam axis $r_S(z_S)$. In general $r_S(z_S)$ is continuous, resulting from the continuously varying refractive index of biological tissues or other samples. It may also be complex, encoding the phase as well as the amplitude of each reflection.

As an illustrative example, $r_S(z_S)$ can be expressed in a series of N discrete, real delta function reflections of the form:

$$r_S(z_S) = \sum_{n=1}^{N} r_{Sn}\delta(z_S - z_{Sn}) \tag{2.23}$$

Each reflection is characterized by its electric field reflectivity $r_{Sn}$and path length from the beam splitter of z_{Sn}. Power reflectivity of each reflector is given by $R_{Sn} = |r_{Sn}|^2$. Reconstruction of the function $\sqrt{R_S(z_S)}$ from noninvasive interferometric measurement is the goal of low coherence interferometry in OCT [1].

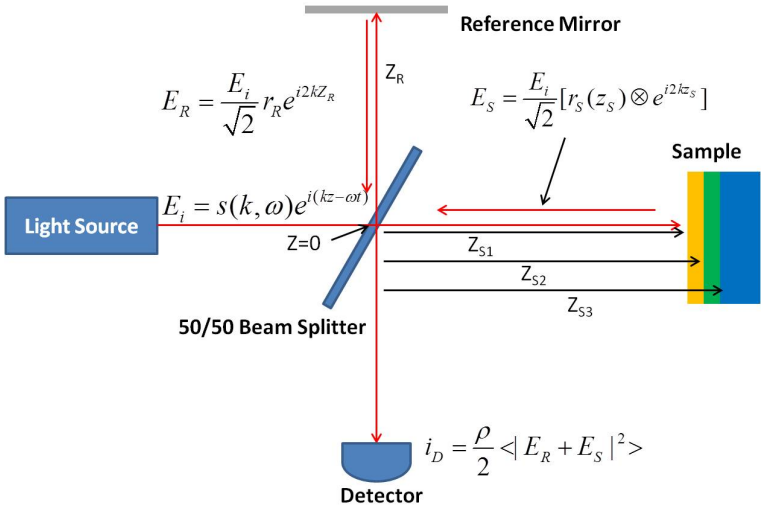

Figure 2.8: Schematic of a Michelson interferometer used in OCT

To better illustrate the theory of OCT, assume the origin of the light propagation is at the beam splitter and the electrical field after beam splitter is

$$E_i = s(k,\omega)e^{i(kz-\omega t)} \tag{2.24}$$

Light coming back from the reference and sample arm will interference with each other at the detector surface.Let the distance from the beam splitter to the detector to be l. We can have the electrical field of the reference and sample as following:

$$E_R = \frac{E_i}{\sqrt{2}} r_R e^{i2kz_R} e^{ikl} \tag{2.25}$$

$$E_S = \frac{E_i}{\sqrt{2}}[r_S \otimes e^{i2kz_S}]e^{ikl} \tag{2.26}$$

Here r_R is the reflectivity of the reference mirror. r_S is described in Eq.(2.23)

Photo current $I_D(k,\omega)$ generated from the detector can be expressed as the time averaging form as

$$I_D(k,\omega) = \frac{\rho}{2} < |E_R + E_S|^2 >= \frac{\rho}{2} < (E_R + E_S)(E_R + E_S)^* > \tag{2.27}$$

Plug in Eq.(2.25) and Eq.(2.26)into Eq.(2.27), we can get

$$I_D(k,\omega) = \frac{\rho}{2} < |\frac{s(k,\omega)}{\sqrt{2}} r_R e^{i(2kz_R - \omega t)} + \frac{s(k,\omega)}{\sqrt{2}} \sum_{n=1}^{N} r_{Sn} e^{i(2kz_{Sn} - \omega t)}|^2 > \tag{2.28}$$

As angular frequency ω oscillates much faster than the response time of any practical detector. Eq.(2.28) can be deduced to temporally invariant as

$$\begin{aligned} I_D(k) &= \tfrac{\rho}{4}[S(k)(R_R + \textstyle\sum_{n=1}^{N} R_{Sn})] \\ &+ \tfrac{\rho}{4}[S(k) \textstyle\sum_{n=1}^{N} \sqrt{R_R R_{Sn}} (e^{i2k(z_R - z_{Sn}} + e^{-i2k(z_R - z_{Sn})}] \\ &+ \tfrac{\rho}{4}[S(k) \textstyle\sum_{n\neq m=1}^{N} \sqrt{R_{Sm} R_{Sn}} (e^{i2k(z_{Sm} - z_{Sn}} + e^{-i2k(z_{Sm} - z_{Sn})}] \end{aligned} \tag{2.29}$$

Here $S(k) =< |s(k,\omega)|^2 >$, is the power spectrum of the light source, which is the similar to previously mentioned $S(\nu)$, wavenumber k instead of frequency ν is used for the convenience of conventional OCT analysis.

2.3.1 Time Domain OCT

In traditional time domain OCT (TD-OCT), $I_D(k)$ is captured on a single detector and the reference mirror z_R needs to be scanned to reconstruct one A-scan signal. The result is obtained by integration of Eq.(2.29) over all k.

$$I_D(z_R) = \frac{\rho}{4}[I_R + \sum_{n=1}^{N} I_{Sn}] + \frac{\rho}{2}\sum_{n=1}^{N} Re< E_R(t+\tau)E_{Sn}^*(t) > \tag{2.30}$$

Take one item out of the second summation for analysis purpose. From Eq.(2.14), we can get the following:

$$Re< E_R(t+\tau)E_{Sn}^*(t) > = \sqrt{R_{Sn}R_R}|\tilde{\Gamma}_{Source}(\tau)|\cos[k_0\Delta z + \phi] \tag{2.31}$$

Here we assume that the central frequency of the light source is much larger than the bandwidth Δk. k_0 is the central wavenumber of the light source and $\tau = \Delta z/c = 2(z_R - z_{Sn})/c, c$ is the speed of light. $\tilde{\Gamma}_{Source}(\tau)$ is the complex temporal coherence function of the light source with argument ϕ. The relationship between $S(k)$ and $\tilde{\Gamma}_{Source}(\tau)$ is essentially a Fourier transform from Eq.(2.14). Usually it is a reasonable approximation to treat the spectrum of the light source as Gaussian.

$$S(k) = \frac{1}{\Delta k\sqrt{\pi}}\exp[-(\frac{k-k_0}{\Delta k})^2] \tag{2.32}$$

Here Δk is the full width half maximum (FWHM)of the spectrum. From Eq.(2.32) and use $\tau = \Delta z/c$ we can get

$$\tilde{\Gamma}_{Source}(\Delta z) = \exp[-\frac{(\Delta z)^2(\Delta k)^2}{4}]\exp(-ik_0\Delta z) \tag{2.33}$$

Plug Eq.(2.33) and Eq.(2.31) into Eq.(2.30), we can get

$$I_D(z_R) = \frac{\rho}{4}[I_R + \sum_{n=1}^{N} I_{Sn}] + \frac{\rho}{2}\sum_{n=1}^{N}\sqrt{R_{Sn}R_R}e^{-(z_R - z_{Sn})^2(\Delta k)^2}\cos[2k_0(z_R - z_S) + \phi] \tag{2.34}$$

Table 2.1: Theoretical Parameters for Simulation

λ_0	$\Delta\lambda$	$\sqrt{R_R}$	$\sqrt{R_{S1}}$	Z_{S1}	$\sqrt{R_{S2}}$	Z_{S2}	$\sqrt{R_{S3}}$	Z_{S3}
800 nm	100&50&20 nm	0.8	0.25	100 μm	0.15	200 μm	0.3	300 μm

The full width half maximum (FWHM) of the Eq.(2.34) with only one single reflector determines the system resolution,

$$\text{RESOLUTION}_{TD-OCT} = \frac{2\sqrt{\ln 2}}{\Delta k} = \frac{2\ln 2}{\pi}\frac{\lambda_0^2}{\Delta\lambda} \approx 0.44\frac{\lambda_0^2}{\Delta\lambda} \tag{2.35}$$

Here $\Delta\lambda$ is the FWHM of the source spectrum in the wavelength domain. From Eq.(2.35) we can know that higher resolution requires broader band light source.

The first term of Eq.(2.31) is the DC term while the second term is the so called "fringe burst" term. A simulated TD-OCT interferogram is shown in Figure 2.9 with the simulated parameters shown in Table 2.1. We can clearly see the envelope peak lies at the simulated layer position with the height proportional to its reflectivity of

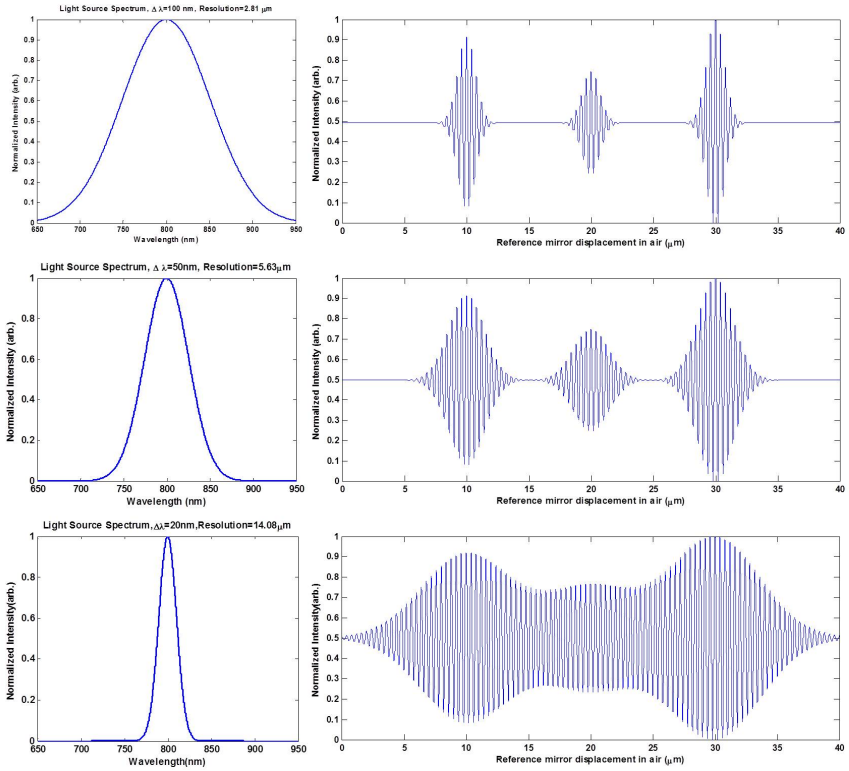

Figure 2.9: A TD-OCT simulation interferogram using parameters given in Table 2.1

that layer. As the light source bandwidth goes smaller, the system resolution gets poorer. Finally when the bandwidth goes down to 20nm, it becomes impossible to distinguish layers that separate with each other 10 μm away, which is below the system theoretical resolution 14.1 μm.

2.3.2 Fourier Domain OCT

From Eq.(2.29) using Euler's rule, $I_D(k)$ will generate a real result for the detector current as a function of wavenumber, commonly known as the "spectral interfero-

gram“.

$$
\begin{aligned}
& i_D(k) = \tfrac{\rho}{4}[S(k)[R_R + \textstyle\sum_{n=1}^{N} R_{Sn}]] && \text{“DC-Term“} \\
& + \tfrac{\rho}{2}[S(k) \textstyle\sum_{n=1}^{N} \sqrt{R_R R_{Sn}} \cos(2k(z_R - z_{Sn})] && \text{“Cross-correlation Term“} \\
& + \tfrac{\rho}{4}[S(k) \textstyle\sum_{n\neq m=1}^{N} \sqrt{R_{Sm} R_{Sn}} \cos(2k(z_{Sm} - z_{Sn}) && \text{“Auto-correlation Term“}
\end{aligned} \tag{2.36}
$$

The Fourier analysis concept depicts that the wave-number dependent detector current $i_D(k)$ is captured and processed using Fourier analysis to reconstruct an approximation of the internal sample reflectivity profile$\sqrt{R_S(z_S}$, which was first proposed by Fercher et al. in 1995 [5]. There are two configurations of the Fourier domain OCT. One is spectral domain OCT (SD-OCT): spectrometer-based OCT, a broadband light source is used and all spectral components of $i_D(k)$ are captured simultaneously on a detector array placed at the output of a spectrometer. The other is swept source OCT (SS-OCT), also called frequency-domain imaging or OFDI), the spectral components of $i_D(k)$ are captured sequentially by recording the signal in a single detector while synchronously sweeping the wavenumber of a narrow band swept-laser source.

After Fourier transform of the Eq.(2.36), we can get

$$
\begin{aligned}
& i_D(z) = \tfrac{\rho}{4}[\gamma(z)[R_R + \textstyle\sum_{n=1}^{N} R_{Sn}]] \\
& + \tfrac{\rho}{4} \textstyle\sum_{n=1}^{N} \sqrt{R_R R_{Sn}} \gamma(z \pm 2(z_R - z_{Sn})) \\
& + \tfrac{\rho}{8} S(k) \textstyle\sum_{n\neq m=1}^{N} \sqrt{R_{Sm} R_{Sn}} \gamma(z \pm 2(z_{Sm} - z_{Sn}))
\end{aligned} \tag{2.37}
$$

$$S(k) = \frac{1}{\Delta k\sqrt{\pi}} e^{-(\frac{k-k_0}{\Delta k})^2} \overset{\text{FT}}{\Longleftrightarrow} \gamma(z) = e^{-\frac{z^2\Delta k^2}{4}} e^{ik_0 z} \tag{2.38}$$

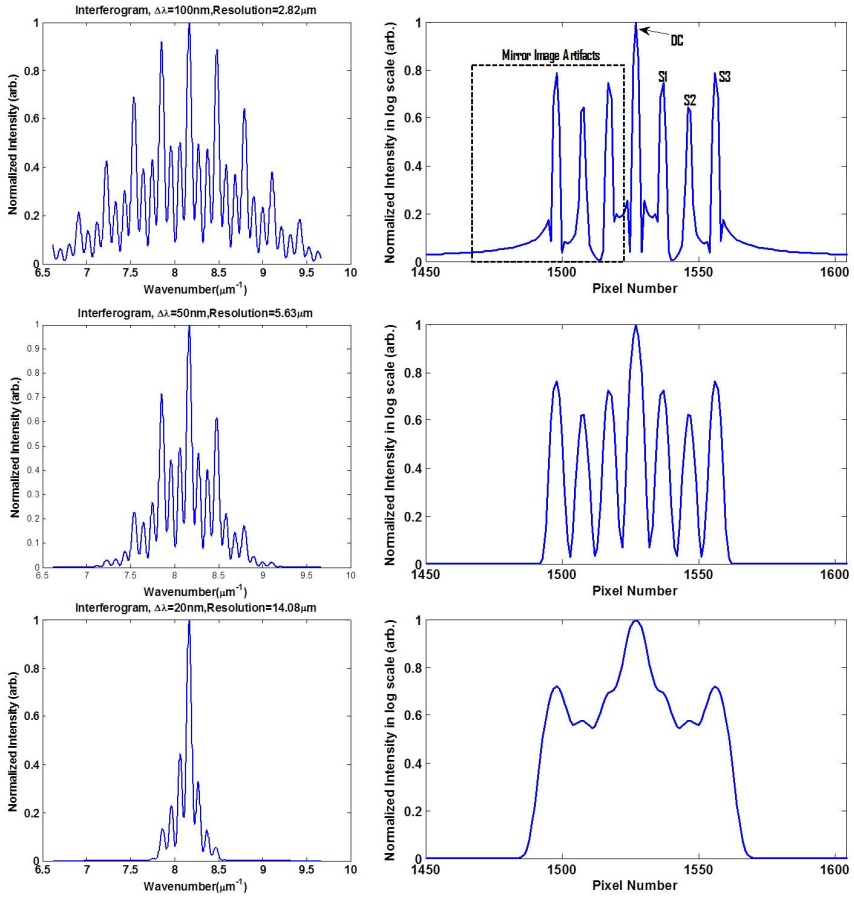

Figure 2.10: A FD-OCT simulation interferogram and processed signal using parameters given in Table 2.1

Based on the same simulation parameters shown in Table 2.1, we can get the Fourier domain signal profile shown in Figure 2.10.

2.3.2.1 Sensitivity

Sensitivity of an FD-OCT system can be expressed as Eq.(2.39) [32].

$$\sum_{FDOCT} = \frac{\frac{1}{N}(\frac{\rho\eta\tau}{h\nu_0}P_0)^2\gamma_r\gamma_s R_r}{\frac{\rho\eta\tau}{h\nu_0}\frac{P_0}{N}\gamma_r R_r[1+\frac{1+\Pi^2}{2}\frac{\rho\eta}{h\nu_0}\frac{P_0}{N}\gamma_r R_r\frac{N}{\Delta\nu_{eff}}]+\sigma_{rec}^2} \tag{2.39}$$

In Eq.(2.39), γ_r and γ_s are the parts of the input power that will exit the interferometer from reference and sample arms; $\rho$is the spectrometer efficiency; η denotes the detector quantum efficiency; τ is CCD integration time; h is the Planck's constant; P_0 is the source power output; Π is the polarization of the source; $\Delta\nu_{eff}$ is the effective spectral line width of light source; N is the number of pixels and σ_{rec} is the RMS receiver noise. There are three terms in the denominator of Eq.(2.39). The first term is caused by shot noise; the second term is the excess noise and the last one is receiver noise.

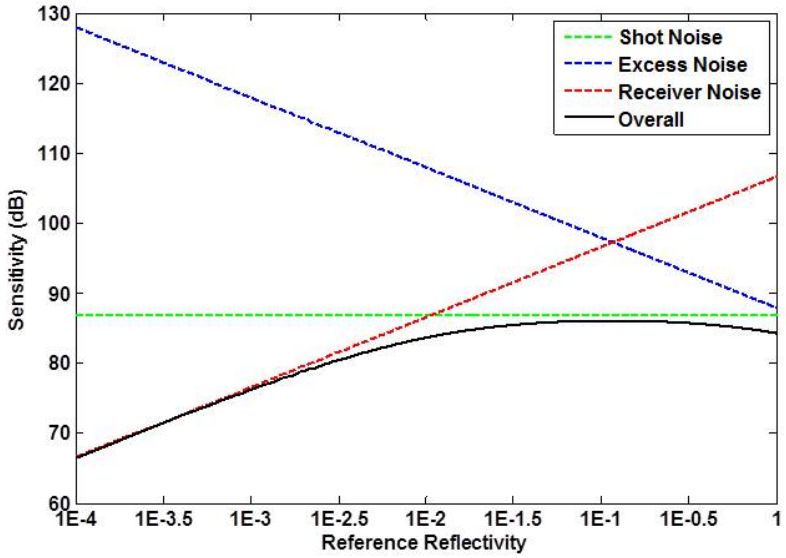

Figure 2.11: Theoretical Sensitivity for one example FD-OCT System

Assume $\Pi = 1; \gamma_r = 0.1; \gamma_s = 0.1; P_0 = 200\mu w; \eta = 0.5; \tau = 14.2\mu s; N = 2048; \rho = 0.8; \sigma_{rec} = 50; \delta\nu_{eff} = 4.4 \times 10^{13} Hz; \lambda_0 = 845nm$,we can get the theoretical sensitivity of one FD-OCT system shown in Figure 2.11. From Figure 2.11, we can know that there is an optimized reference reflectivity for a given FD-OCT system and that once OCT operates in the shot-noise limited regime, further increase of the reference reflectivity contributes little to the system sensitivity.

It also needs to be pointed out that FD-OCT system has superior sensitivity over TD-OCT system.

$$SNR_{FDOCT} = SNR_{TDOCT}\frac{M}{2}; \tag{2.40}$$

Here M is the pixel number of a detector array of the spectrometer or the sampling points in one A-scan. The factor of $M/2$ improvement in FDOCT over TDOCT can be simply improved from the fact that both FDOCT methods sample all depths at the same time, giving a rise to a potential SNR improvement by a factor of M; however, there are redundant data in FD-OCT, which explains the factor of $\frac{1}{2}$ [33].

2.3.2.2 Sensitivity falloff and sampling effects in FD-OCT

When it comes to real experimental setup, instrumentation acquiring the spectral interferogram always has limited spectral resolution, denoted by $\delta_r k$. For example in SS-OCT, the instantaneous line shape of the swept source has certain width and in SD-OCT spectral resolution of the spectrometer is limited due to the finite spacing of CCD/CMOS pixels. This will cause sensitivity fall-off over the depth. The spectral

Table 2.2: Imaging depth of sensitivity falloff in FD-OCT

	Maximum one-side imaging depth	6dB SNR falloff
Wavenumber(k)	$\frac{\pi}{2\delta_s k}$	$\frac{2\ln(2)}{\delta_r k}$
Wavelength(λ)	$\frac{\lambda_0^2}{4\delta_s \lambda}$	$\frac{\ln(2)}{\pi}\frac{\lambda_0^2}{\delta_r \lambda}$

interferogram sampling interval $\delta_s k$ will effect the maximum imaging depth of the system. Both effects are shown in Table 2.2.

2.3.3 Tissue Optics

OCT is a primary imaging modality for biological soft tissue. Light interaction with soft tissue plays an important role in the imaging. Actual OCT imaging depth of OCT is usually smaller than the theoretical maximum imaging range due to the light absorption and scattering in the tissue.

2.3.3.1 Tissue Absorption

Tissue absorption originates from photon interaction with atoms and molecules of the tissue, and is closely dependent on the tissues biological and chemical composition. The absorption coefficient μ_a is defined as the probability of photon absorption in a medium per unit path length. It has a representative of $0.1cm^{-1}$ in biological tissue. The reciprocal of μ_a is referred to as the mean absorption length. According to the definition of the absorption coefficient, light attenuates as it propagates in an

absorbing-only medium according to the following equation:

$$\frac{dI}{I} = -\mu_a dx \tag{2.41}$$

where I denotes the light intensity and x denotes the distance along the light propagation direction. Integrating Eq.(2.41) leads to the well-known Beer law

$$I(x) = I_0 \exp(-\mu_a x) \tag{2.42}$$

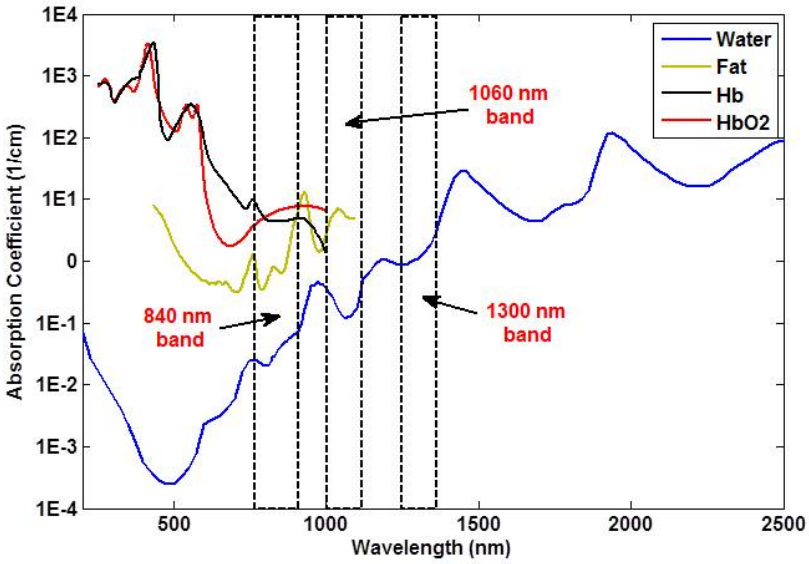

Figure 2.12: Absorption coefficient spectra of biological absorbers.Hb:deoxygenated hemoglobin; HbO_2: oxygenated hemoglobin

The absorption coefficients of some primary absorbing biological tissue components are plotted as a function of wavelength in Figure 2.12. Most of the biologcial

tissues consist of over 75% of water. Three main OCT imaging wavelength band windows are also marked in Figure 2.12.

2.3.3.2 Tissue Scattering

Scattering of light by a spherical particle of any size can be modeled exactly by the Mie theory, which reduces to the simpler Rayleigh theory if the spherical particle is much smaller than the wavelength. The scattering coefficient μ_s is defined as the probability of photon scattering in a medium per unit path length. It has representative value of $100cm^{-1}$ in biological tissue. The reciprocal of μ_s is referred to as the scattering mean free path. For Rayleigh scattering, the scattering cross section meets,

$$\sigma_s \propto \frac{1}{\lambda^4} \tag{2.43}$$

For a medium containing many scatters with number density N_s, the scattering coefficient can be considered as the total cross-sectional area for scattering per unit volume:

$$\mu_s = N_s \sigma_s \tag{2.44}$$

It can be seen that 840 nm band OCT system suffers from a huge blood absorption when dealing with blood vessels, which will create shadowing effect on the image. As the wavelength moves towards 1060nm and 1300nm band, though water absorption becomes higher the scattering coefficient goes down, thus usually longer wavelength

OCT exhibit deeper imaging depth of soft tissue than the 840nm band OCT.

Chapter 3

GPU Accelerated Signal Processing of SD-OCT

3.1 Signal Processing of OCT

For time domain OCT (TD-OCT), from Figure 2.9, while the reference mirror scanned in the reference arm, modulated signal from the detector will be demodulated and recorded to computer for each A-scan. Multiple A-scans form the B-scan frame when the beam gets scanned. Finally processed data is shown as a B-mode image or volumetric image. The imaging speed is limited by the reference mirror scanning speed and acquired signal SNR is lower compared to FD-OCT.

For SD-OCT, raw spectrum from the CCD or CMOS camera is acquired to the computer memory through frame grabber. To get rid of the strong DC component of

the spectrum, a physical reference spectrum, which is acquired with no sample in the sample arm, is subtracted from the raw spectrum. Data got from the spectrometer is linear in the wavelength domain. As $k = 2\pi/\lambda$, it is not linear in wavenumber domain. Though linear-k spectrometer could be generated, it is much complicated and whatever [**?**]. To accelerate the processing speed of Fourier transform FFT algorithm is used. However it requires the raw spectrum data to be linear in the wavenumber domain. Certain interpolation methods need to be applied to get the raw spectrum linear in the wavenumber domain. Usually linear and cubic interpolation is utilized to achieve so. To avoid the interpolation error NUDFT and NUFFT were also utilized by researchers at the sacrifice of processing speed. After Fourier transform of the interferogram, log rescaling of the signal is performed to adjust the dynamic range for better human visualization. Each A-scan within a B-scan or C-scan will be processed the same way independently and repeatedly. When all the processing is done, the computer finally displays the image on the monitor. The imaging speed of SD-OCT system depends on the line period of the spectrometer. Nowadays it usually ranges from 10kHz to 200 kHz.

For SS-OCT, most of the signal processing is the same. Except that there are usually k-clock signals, provided to the data acquisition (DAQ) card for the equal-spaced k signal acquisition. The k-clock signal generation utilizes the Mach-Zehnder interferometer introduced in Chapter 2. The speed of swept lasers could be much higher than SD-OCT. Nowadays it can range from tens of thousand hertz to megahertz.

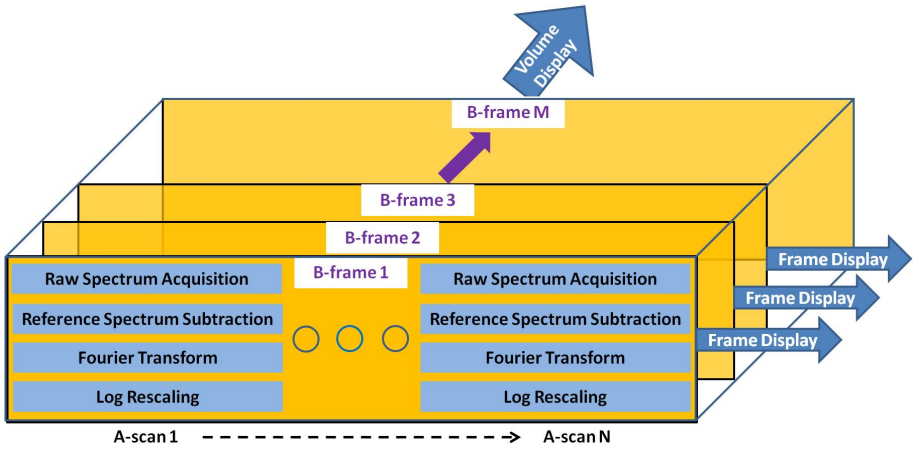

Figure 3.1: OCT Signal Processing Illustration

Figure 3.1 illustrates the OCT signal processing. The processing is frame by frame. All the A-scans within one frame need to be processed in order to perform frame display. The same processing repeats for the following acquired frames, and finally the processed volume data is sent to perform volume display, either through en-face or ray casting based volume rendering. Advanced functional OCT signal processing can also be achieved based on these basic procedures, such as phase resolving which will be introduced later in this chapter and full-range complex conjugate removal processing and numerical dispersion compensation.

As introduced in Chapter 1, GPUs have been demonstrated as a powerful acceleration engine for OCT signal processing and visualization due to the enormous computation power of GPUs and massively parallelism of OCT A-scan data processing. While CPU processes all the A-scans sequentially, GPUs can process multiple A-scans at the same time, which greatly reduces the computation time, shown in Figure 3.2.

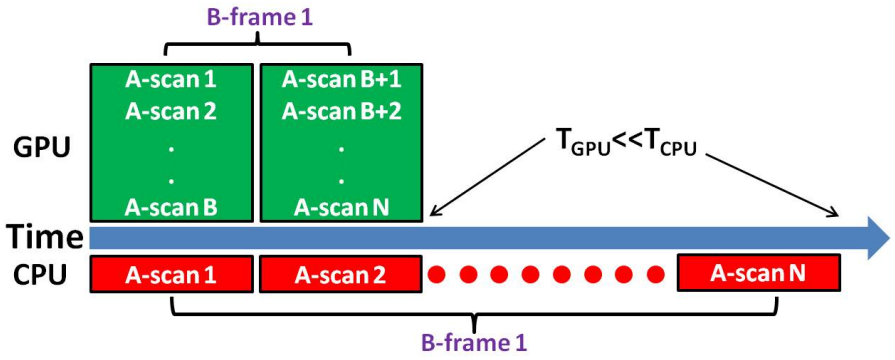

Figure 3.2: OCT Signal Processing Illustration

3.2 Reference A-line Subtraction ans Saturation Correction

Fourier-domain optical coherence tomography (FD-OCT) is a high-speed high-resolution three-dimensional imaging modality widely used in biomedical imaging. For OCT to find applications in the interventional imaging area, real-time image processing and display are required. The presence of the fixed-pattern-noise artifact that forms strong erroneous horizontal lines laying over the image is among the most common noises of FD-OCT [1]. The fixed-pattern-noise artifact can be removed if the reference spectrum of that imaging frame is known. Therefore, in the case of high-resolution OCT imaging of a fixed site, simple subtraction of the reference spectrum from the OCT signal spectra works very effectively. However, the source spectrum shape varies over time; the OCT signal level and the spectra vary frame by frame; the optical phase and polarization can also vary frame to frame. Therefore, an ef-

fective signal processing method that can remove the DC levels due to these changes in real-time from the image data and thus remove the fixed pattern noise is of great importance in improving the quality of OCT images [34, 35]. However, periodically measuring and verifying the reference spectrum for OCT video imaging is highly inconvenient and impractical. Saturation artifacts occur when light reflected back from a highly specular surface generating signals that are over the dynamic range of the data acquisition system [36]. It is not uncommon to see optical coherence tomography images that are corrupted by saturations artifacts for example, in cornea imaging [37, 38], intracoronary imaging [36], and finger pad imaging [39]. Real-time removal of the saturation artifacts will increase the diagnostic and interventional accuracy. Due to the tremendous parallel computing power of GPU, GPU-based OCT processing techniques have recently been shown to be highly effective in accelerating a wide range of OCT signal processing methods such as fast Fourier transform, resampling, discrete Fourier transform, dispersion compensation, 3D rendering in high speed, and high quality real-time FD-OCT imaging [16–18, 21, 22]. In this work, we developed an optimized algorithm for GPU based on the minimum variance mean-line subtraction (MVMS) method which was first proposed by Moon et al [34]to remove the reference fixed pattern artifact. To improve upon and to address a commonly encountered problem with a large fluctuation of the signal intensity, we developed and incorporated an algorithm to also perform automatic detection of the saturated scan lines and correction using linear interpolation of adjacent normal A-scan lines. We op-

timized both methods for the GPU architecture and successfully integrated them with existing GPU-based OCT signal processing to demonstrate real-time fixed-pattern-noise-free and automatic saturation artifact correction FD-OCT video imaging at 70 frames/s for a frame size of 1000 (lateral) 1024 (axial) pixels. The theoretical maximum processing and rendering rate was calculated to be 266,000 A-scans/s.

The proposed method was demonstrated using an in-house developed spectral-domain OCT. The system configuration is shown in Figure 3.3. The customized spectrometer was built using a 12-bit, 70 kHz, 2048 pixel, CCD line-scan (EM4, e2v, USA) as the detector. A superluminescent (SLED) light source with an output power of 10 mW and an effective bandwidth of 105 nm centered at 845 nm which gave the theoretical axial resolution of 3.0 μm in air was used for the experiment. A quad-core @ 2.4GHz Dell Precision T7500 workstation was used to host a frame grabber (NI PCIe-1429, PCIE-x4 interface), and an NVIDIA GeForce GTX 590 GPU (PCIE-x16 interface, 32 stream multiprocessors, 1024 cores at 1.21 GHz, 3 GB graphics memory). Residual dispersion of the system caused by the components, L1, L2, L3, SL, and the optical fibers was compensated numerically through a GPU process described in [12]. All the data acquisition, image processing, and rendering were performed on this multi-thread, CPU-GPU heterogeneous computing system. A customized user interface was designed and programmed through C++ (Microsoft Visual Studio, 2008). CUDA (Computer Unified Device Architecture) 4.0 from NVIDIA (Santa Clara, California) was used to program the GPU for the general purpose computation

[40].

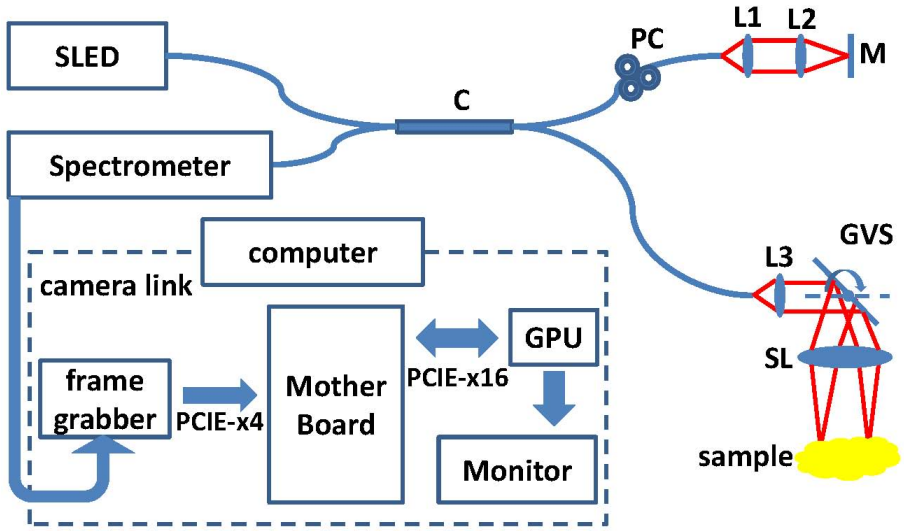

Figure 3.3: System configuration, C: 50-50 broadband fiber coupler; L1, L2, L3: achromatic lenses; M: mirror; GVS: galvanometer pairs; PC: polarization controller; SL: scanning lens

Figure 3.4 shows the data processing flowchart of the OCT system. The acquired data (16-bit unsigned integer format) from the frame grabber was stored in a host pinned or page-locked memory buffer before the GPU processing. This eliminated the need for having to copy the data to the GPU global memory in mapped memory method supported by CUDA 4.0. The GPU processing included cubic resampling, saturation detection, dispersion compensation, FFT, MVMS, log scaling, soft thresholding and saturation correction if necessary to form the final OCT image data. The image data were then copied back to the host memory for the display and for saving. Details of the implementation of the signal processing other than MVMS, saturation detection and correction can be found in [17, 20, 21, 41].

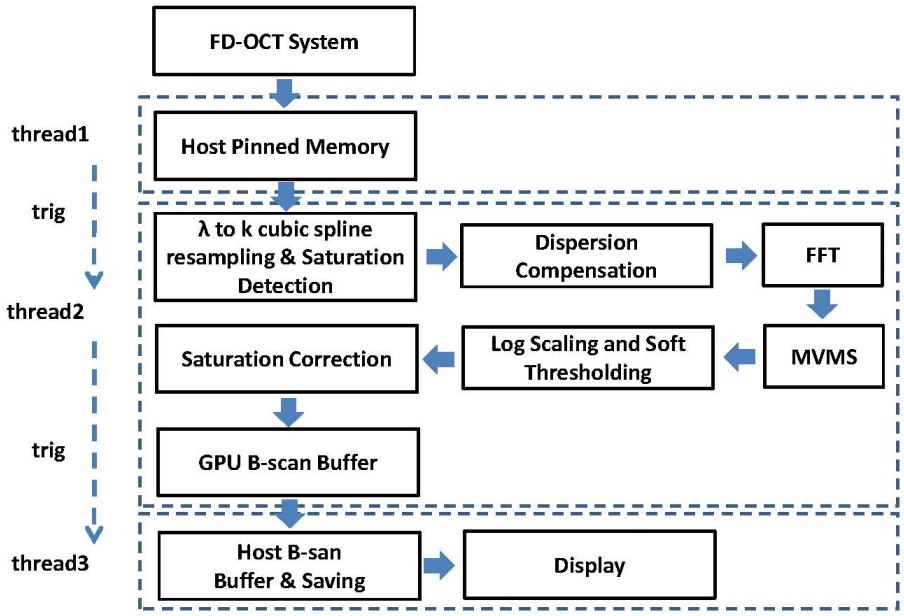

Figure 3.4: Data processing flow chart for standard FD-OCT, Dashed arrows: thread triggering; solid arrows: data stream. Here the entire GPU memory buffers were allocated on the global memory. Thread 1 controls the data acquisition, thread 2 controls the data processing that is all done on GPU, and thread 3 controls the image display. Dashed squares indicate the task of each thread.

In the MVMS scheme, a segment of the minimum variance is selected for its mean value $\mu_\Omega(z)$ to be assigned as the A-line value of that axial position,z.

$$\mu_\Omega(z) = \frac{1}{L}\sum_{l\in\Omega} g_l(z) \tag{3.1}$$

where Ω represents a segment of the A-line data, and L is the number of data points of Ω. $g_l(z)$ is a complex A-line data point obtained after Fourier transform of the

cubic spline interpolated spectrum. The segmental variance, ν_Ω is defined as

$$\nu_\Omega = \frac{1}{L}\sum_{l\in\Omega}(\mathrm{Re}\{g_l\} - \mathrm{Re}\{\mu_\Omega\})^2 + \frac{1}{L}\sum_{l\in\Omega}(\mathrm{Im}\{g_l\} - \mathrm{Im}\{\mu_\Omega\})^2 \tag{3.2}$$

The mean of the segment, whose variance is minimum in a horizontal line, is assigned to the reference A-lin for an axial position of z [34].

To implement this method in real-time on a GPU architecture, a customized data struct composed by three float numbers which are the mean values of the real part, the mean value of the imaginary part, and the variance, respectively, were used. The reference A-line is represented by the data struct unit with a length of half the number of data points in one A-scan spectrum. After a reference A-line was obtained, it was subtracted from the image in the later log scaling and soft thresholding step. To make Eq.(3.1) and Eq.(3.2) more suitable for the GPU thread execution, a recursion method was used to minimize the thread global memory read operation, shown in the following:

$$\mu_{l+1}(z) = \mu_l(z) + \frac{1}{l+1}(g_l(z) - \mu_l(z)) \tag{3.3}$$

$$\nu(z)^2_{l+1} = \nu(z)^2_l + \frac{1}{l+1}[\frac{l}{l+1}(g_{l+1}(z) - \mu_l(z))^2 - \nu(z)^2_l] \tag{3.4}$$

Increasing index l one by one will lead to a final variance and mean value of that segmentation. The recursion method decreases the memory read operation by half. The algorithm was further optimized through block and grid design of the GPU

kernel launch and the optimization of the segmentation numbers for certain lateral A-scan numbers in each frame. For a frame with 1000 lateral pixel size, a block size of 128 threads and a grid size of 128 were found to be optimal. This way each stream multiprocessor has 8 blocks running simultaneously. The segmentation number of 10 was found to be optimum, and the result was based on previous kernel function launch configuration of 5, 10, 20 segmentations.

The saturation detection process was combined with the cubic spline interpolation to make the signal processing seamless. Since the spectrometers dynamic range is 12bit, the outputs are expressed in values between 0 to 4095. Therefore an unsaturated spectrum should have all the values less than 4095. While each A-line spectrum point are being calculated, the number of points within that A-scan that have values equal to 4095 are updated. If the number of points in that A-scan contains more than2 points that are saturated, that A-line spectrum is marked as saturated A-line. This is done by changing the corresponding status flag to false in an array that records the status of each A-line. The saturation correction was performed in the spatial image domain after log rescaling and soft thresholding. The kernel function checks the status of each A-line of the processed frame. If a certain A-line is marked as false, then the program searches the most adjacent upper and bottom A-lines that are marked as true. Then that A-line was corrected by linear interpolation of the upper and bottom A-lines.

CUDA profiler 4.0 from CUDA Toolkit 4.0 was used to analyze the time cost of

each kernel function of our GPU program. We launched 5 sessions of our application, each session ran the application 5 times. All the following time costs are based on the average measured value with standard deviation marked.

The GPU processing time for MVMS based on Eq.(3.1) and Eq.(3.2) was $440\pm0.6\mu s$ and Eq.(3.3) and Eq.(3.4) was 400 ± 0.6 μs for image frame size of 10241000. This simple comparison shows that the proposed recursive MVMS processing method improves the processing speed as we expected, though it is only 10 percentage time cost reduction. To verify the speedup compared to a CPU-based recursion method. The same MVMS processing method based on (3), (4) was implemented on the same workstation where the GPU is hosted using C++ (Microsoft Visual Studio, 2008) and the CPU is the only computing source. The artificial generated frame of complex data is of size of 1024×1000. The CPU-based MVMS was performed with 10 segmentations with 100 points within each. Running the same procedure 1000 times, the averaged time cost was measured to be 55.22 ± 0.54 ms. This shows that GPU-based MVMS method provided 138 times the speed enhancement compared to a CPU-based MVMS method.

The saturation detection step added a very little computation burden to the cubic spline interpolation processing. We measured the time cost of the cubic spline interpolation and cubic spline interpolation combining saturation detection. The additional time cost for the saturation detection was 90 ± 0.15 μs. The saturation correction step costs 36 ± 0.07 μs. Note that this time cost may vary depending on how many

saturated A-lines there are within one frame. The total time cost for the saturation corrected imaging is only $126 \pm 0.22 \mu s$.

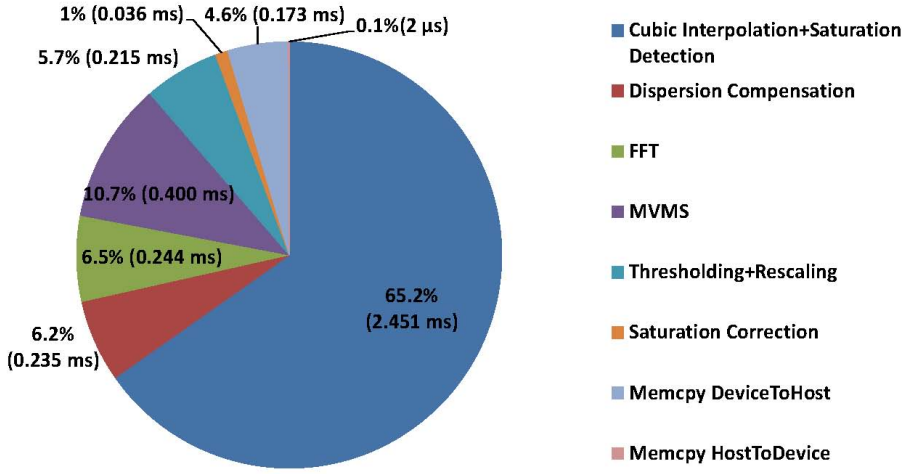

Figure 3.5: Pie Chart of time cost of all system GPU kernel functions.

The time cost for all the system GPU kernel functions for a single image frame size of 1024×1000, corresponding to spectrum data size of 2048×1000, is presented in the Figure 3 pie chart. As can be seen from Figure 3.5, cubic interpolation of the spectrum data was the main GPU computational consumer. Optimization of the cubic interpolation was obtained. By using the pinned memory, the explicit data transfer from host to GPU is negligible. Note that different implementation and optimization might cause various cost time distribution. For our system, MVMS takes 10.5 percentage of the total GPU computing time, saturation detection and correction takes 2.4 percentage and 1 percentage respectively. The total GPU time is 3.76×0.01 ms, which correspond to the maximum imaging speed of 266,000 A-lines/s, which is well above the camera imaging speed of 70,000 A-lines/s and provides enough

room for further GPU accelerated functionality. Our software processing system could benefit significantly from a wavelength swept-source OCT operating with a k-clock and other Fourier Domain OCT systems that are based on k-sampled spectrometer. If cubic interpolation can be saved, the system could potentially run at peak processing speed of 714,000 A-lines/s.

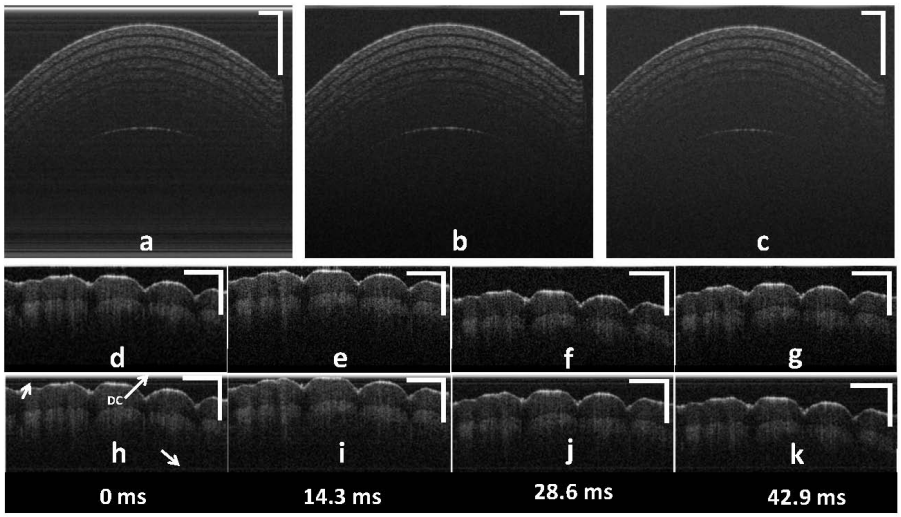

Figure 3.6: Images of layered polymer phantom: a, without reference subtraction; b, real time reference A-line subtraction; c, physical reference spectrum subtraction and real-time in vivo finger tip video imaging (d) (g) with reference correction and (h)-(k) without reference correction (time bar was marked on the bottom, scale bar is 400 m, white arrows indicate several obvious fixed pattern noise).

To demonstrate the effectiveness of MVMS method, we imaged a layered polymer phantom and a human finger and analyzed the result. The result is shown in Figure 3.6. Figure 3.6a is an image without the reference subtraction. One can clearly see the strong horizontal line artifacts running across the image. Figure 3.6b is an image using MVMS processing; Figure 3.6c is an image obtained with the physical reference subtraction. The physical reference was measured before the image acquisition by

blocking the sample arm and was subtracted from the measured spectrum during the image acquisition process. We can clearly see that MVMS processing removes the fixed pattern artifact cleanly and performs better than physical reference subtraction in terms of image visibility. Further analysis of the images shows that the image in Figure 3.6b exhibits 2 dB SNR improvements over the image in Figure 3.6c. The reason for this improvement is that MVMS performed in real-time is more effective in removing the effect of time varying reference spectrum and other DC component during the image acquisition process. Since wavelength dependent absorption and scattering from the imaging sample changes the overall spectrum, physical reference spectrum measured when there is no sample at the sample arm doesnt truly reflect the effective reference spectrum that should be subtracted. We also obtained video sequences of an in vivo human finger tip captured at 70 Hz with and without MVMS processing; and they are shown in Figure 3.6d-4g and Figure 3.6 4h-4k, respectively. One can clearly see that fixed-pattern-artifact was effectively removed in Figure 3.6 4h-4k.

To further demonstrate the effectiveness of the saturation detection and correction, we imaged a layered polymer phantom again. The layer polymer phantom was chose due to its abundance of highly specular reflections along the scanning surface. We also increased the integration time of our system to make the saturation occur more frequently. The result is shown in Figure 3.7. The images are cropped to the first 100 pixels in axial direction to clearly show the saturation artifacts. We scanned

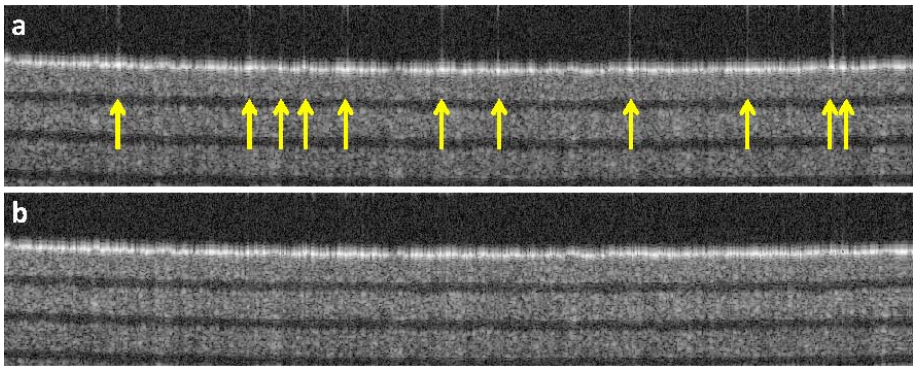

Figure 3.7: Layered polymer phantom imaging (a) without saturation detection and correction (b) with saturation detection and correction (saturated lines are pointed out by yellow arrows).

the same area of interest with and without the saturation detection and correction. Figure 3.7a is the saved image frame without the saturation detection and correction. The saturation areas are marked with yellow arrows on the image. Figure 3.7b is the same image with the saturation detection and correction. We can see clearly that the saturation artifacts have been detected and removed. Here the saturation correction was performed with a linear interpolation. Switching to cubic interpolation will increase the interpolation accuracy but with more time cost. Nevertheless, the cubic interpolation based saturation correction is currently being developed in our laboratory. Note that this method is limited to when saturated artifacts are sparse. When there are large areas of continuous saturation, the interpolation would cause errors. The system integration time and reference level needs to be adjusted dynamically instead.

3.3 Real-time Doppler OCT based on dual GPUs

3.3.1 Introduction

In vivo non-invasive imaging of both microcirculation and tissue structure is a hot area that has attracted significant amounts of interest since it is an indicator of biological functionality and abnormality of tissues. Pioneering work by Z.P. Chen et al. combining the Doppler principle with OCT has enabled high resolution tissue structure and blood flow imaging [42]. Since then, OCT-based flow imaging techniques have evolved into two different approaches: optical coherence angiography (OCA) to detect microvasculature [43–47] and Doppler tomography (ODT) to quantitatively measure blood flow [48–55]. In spectral domain ODT, the magnitude of Fourier transformation of the spectral interference fringes is used to reconstruct cross-sectional, structural image of the tissue sample, while the phase difference between adjacent A-scans is used to extract the velocity information of the flow within the tissue sample.

Real-time imaging of tissue structure and flow information is always desirable and is becoming more urgent as fast diagnosis, therapeutic response, and intraoperative OCT image-guided intervention become established medical practices. In addition, a higher imaging speed can effectively reduce motion artifact for in vivo imaging and

thus significantly improve the quality of ODT images [56, 57]. High speed CCD camera or swept source enables OCT or ODT to have higher signal acquisition speed, or higher temporal resolution of blood flow imaging system which allows for better reconstruction of the time course of dynamic processes. However,due to the large amount of raw data generated by an OCT engine during a high-speed imaging process and heavy computation task for computer systems, real-time display is highly challenging. A graphics processing unit (GPU)-accelerated signal-processing method is a logical solution to this problem due to the way OCT data are acquired and due to the fact that they can be processed in parallel.

In this section we present real-time 3D (2D cross-sectional image plus time) and 4D (3D volume plus time) phase-resolved Doppler OCT (PRDOCT) imaging based on configuration of dual graphics processing units. The dual graphics processing units configuration offers more computation power, dynamic task distribution with more stability, and an increased software-friendly environment when further performance enhancement is required [21]. To achieve real-time PRDOCT, we developed a GPU-based phase-resolving processing algorithm; this was integrated into our current GPU-accelerated processing algorithm, which included cubic wavelength-to-wavenumber domain interpolation, numerical dispersion compensation [41], numerical reference and saturation correction [25], fast Fourier transform, log-rescaling, and soft-thresholding. These processes were performed with the first GPU. Once 4D imaging data were processed, the whole structure volume and flow volume data were trans-

ferred to the second dedicated GPU for ray-casting-based volume rendering. The 3D and 4D imaging mode can be switched easily by customized graphics user interface (GUI). For phase-resolved image processing, we combined a structure image-based mask, thresholding and an average window method to improve the signal-to-noise ratio of the Doppler phase image. Flow and structure volume rendering shares the same model view matrixfor the sake of easy visual registration when ray-casting was performedwith two different customized transfer functions. The model view matrix can be modified interactively through the GUI. This flexibility makes the interpretation of volume images easier, more reliable, and complements a single-view perspective. Real-time 2D simultaneous display of structure and flow images were presented at a frame rate of 70 fps with an image size of 10001024, corresponding to 70K raw spectra per second; To present the 3D image data set, real-time 3D volume rendering of tissue structure and flow imageseach with a size of 512×512 pixelswere presented 64.9 ms after every volume scanning cycle where the acquired volume size was 500×256×512 (X×Y×Z). To the best of our knowledge, this is the first time online simultaneous structure and flow volume visualization have ever been reported. The theoretical maximum processing speed was measured to be 249,000 A-scans per second, which was above our current maximum imaging speed of 70,000 A-scans per second limited by the camera speed. Systematic flow phantom and in vivo chorioallantoic membrane (CAM) of chicken embryo imaging were performed to characterize and test our high-speed Doppler spectral domain OCT imaging platform.

3.3.2 Methods

We integrated the GPU-accelerated Fourier domain PRDOCT method into our previously developed GPU-accelerated OCT data processing methods based on an in-house-developed spectral domain OCT. The hardware system configuration is shown in Figure 3.8. The A-line trigger signal from the frame grabber was routed to the data acquisition (DAQ) card as the clock source to generate the waveform control signal of the scanning galvanometers. We used an A line-scan camera (EM4, e2v, USA) with 12-bit depth, 70 kHz line rate, and 2048 pixels as the spectrometer detector. We used a superluminescent (SLED) light source with an output power of 10 mW and an effective bandwidth of 105 nm centered at 845 nm, which gave an axial resolution of 3.0 m in air for the experiment. The transversal resolution was approximately 12 m, assuming a Gaussian beam profile.

We used a quad-core @2.4 GHz Dell Precision T7500 workstation to host a frame grabber (National Instrument, PCIe-1429, PCIE-x4 interface), a DAQ card (National Instrument, PCI 6211, PCI interface) to control the galvanometer mirrors and two NVIDIA (Santa Clara, California) Geforce series GPUs: One is GTX 590 (PCIE-x16 interface, 32-stream multiprocessors, 1024 cores at 1.21 GHz, 3 GB graphics memory); the other is GTS 450 (PCIE-x16 interface, 4-stream multiprocessors, 192 cores at 1.57 GHz, 1 GB graphics memory). GTS 450 was dedicated to perform volume ray-casting and image rendering while GTX 590 was used to process all the necessary pre-volume rendering data sets for GTS 450. All the scanning control, data

acquisition, image processing, and rendering were performed on this multi-thread, CPU-GPU heterogeneous computing system. A customized user interface was designed and programmed through C++ (Microsoft Visual Studio, 2008). We used computer unified device architecture (CUDA) version 4.0 from NVIDIA to program the GPU for general purpose computations.

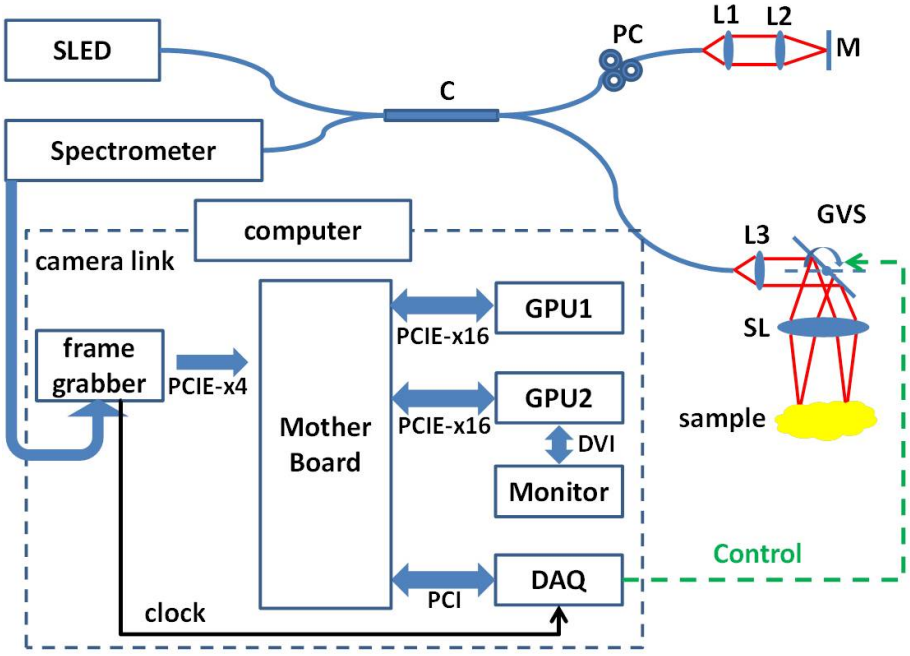

Figure 3.8: System configuration: L1,L3, achromatic collimators; L2, achromatic focal lens; SL, scanning lens; C, 50:50 broadband fiber coupler; GVS, galvanometer pairs; PC, polarization controller, M, reference mirror.

Figure 3.9 shows the data process flowchart of the OCT system. Thread 1 marked by a green box controlled the data acquisition from frame grabber to host memory. Once one frame is ready, thread 2 marked by a yellow box copies the B-scan frame buffer to GPU1 frame buffer and controls GPU1 to perform B-frame structure and phase image processing. Once both images are ready, they are transferred to cor-

responding host buffers for display and to host C-scan buffers for later volume rendering. Thread 2 also controls the DAQ card to generate scanning control signals to galvanometer mirrors using A-line acquisition clocks routed from the frame grabber (not illustrated in Figure 3.9). When the host C-scan volume buffers are ready, thread 3 marked by a red box transfers both the structure volume and phase or velocity volume from the host to device, and commands the GPU2 to perform ray-casting-based volume rendering. Details about the implementation of structure image processing and ray-casting-based volume rendering can be found in our previously reported studies [19, 21,25]. We made further improvement to the ray-casting algorithmincluding a real-time, user-controlled model view matrixto provide multiple view perspectives and customized different transfer functions to structure volume image and flow volume image. Here synchronization and hand-shake between different threads are realized through a software event-based trigger.

After structure image processing, which includes wavelength-to-wavenumber cubic spline interpolation, numerical dispersion compensation, FFT, reference and saturation correction, the complex structure image can be expressed as

$$\tilde{I}(z,x) = A(z,x)\exp[i\varphi(z,x)] \tag{3.5}$$

where $\varphi(z,x)$ is the phase of the analytic signal. The phase difference between adja-

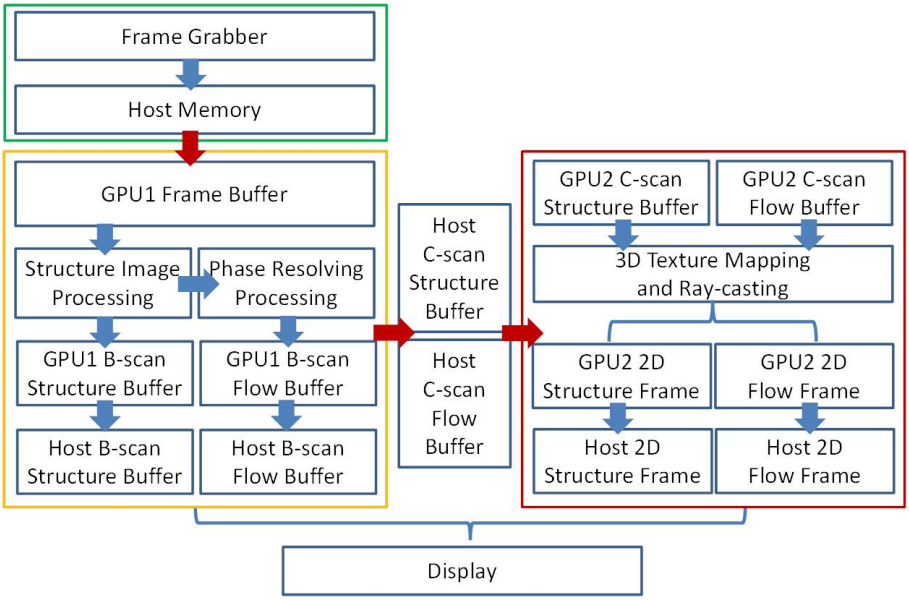

Figure 3.9: Data processing flowchart of the OCT system. Solid arrows: data stream, blue indicates internal GPU or Host data flow red indicates GPU-host data flow; here the entire GPU memory buffers were allocated on global memory. Thread 1 boxed by green controls the OCT data acquisition; thread 2 boxed by yellow controls the GPU1 data processing and galvanometer mirrors; thread 3 boxed by red controls the GPU2 volume rendering processing. Synchronization and hand-shake between threads are realized through a software event-based trigger.

cent A-scans, n and n-1, is calculated:

$$\Delta\varphi(z,x) = \tan^{-1}\left[\frac{Im[\tilde{I}(z,x_n) \bullet \tilde{I}^*(z,x_{n-1})]}{Re[\tilde{I}(z,x_n) \bullet \tilde{I}^*(z,x_{n-1})]}\right] \tag{3.6}$$

Based on the linear relationship between phase difference between adjacent A-lines and velocity, the velocity of flow signal image can be expressed as

$$\upsilon(z,x) = \frac{\lambda\Delta\varphi(z,x)}{4\pi\cos(\theta)\Delta t} \tag{3.7}$$

In this study the camera was running at 70 kHz. We measured our system phase noise level to be 0.065 rad by measuring the standard deviation of the phase of a stationary mirror as a target. The velocity of flowing target projected to the parallel direction of the scanning beam thus was [-14.2, -0.294]$\bigcup$[0.294, 14.2] mm/s. By varying the camera scanning speed, a different velocity range can be achieved based on Eq.(3.7).

The phase-resolving processing box in Fig. 2 consists of the following operations:
1. Generate a structure image intensity level-based binary phase-thresholding mask to filter out the background non-signal area. Most OCT images consist of a relatively large background area that carries no information. The signal intensity in the background area is usually low. By thresholding the structure image intensity, a binary mask with the same size of structure image can be generated. The value of each pixel in the mask was assigned to one if the corresponding structure pixel value has intensity level above the threshold value and to zero if the corresponding structure pixel value has intensity level below the threshold value. The threshold value was currently controlled by the user based on visual judgment. Automatic threshold value generation by statistically analyzing the image intensity will be our future modification.
2. Calculate the phase based on Equation (2) and previously generated binary mask. If the value of a certain position in the mask was zero, we assigned zero phase value to that position instead of performing the phase calculation operation. Otherwise, the phase was calculated according to Equation (2). This mask operation would reduce

the amount of calculation load of the GPU cores.

3. Average the phase images with an averaging window to further improve the signal-to-noise ratio. Here we mapped the phase image to a certain portion of texture memory of the GPU. As the averaging operation used a lot of locality or neighboring values, texture memory would accelerate the data read speed compared to normal global memory of GPU. The window size we used here was 33, which is a commonly used window size for processing Doppler images.

4. Map the phase value to a color scheme. We used a so-called jet color map during our phase-to-color mapping process, which maps to deep red and - to deep blue. In between, the color varies from light red to yellow and green and then light blue. Green color corresponds to zero phase value.

5. Shrink the phase image by half in lateral and axial directions to 500512 pixels to accommodate the display monitor size, which is equivalent to a final 66 average window over the phase image.

Volume rendering is a set of techniques used to display a 2D projection of a 3D discretely sampled data set, which simulates the physical vision process of the human eye in the real world and provides better visualization of the entire 3D image data than 2D slice extraction. Ray-casting is a simple and straightforward method for volume rendering. The principle of ray-casting demands heavy computing duty, so in general real-time volume rendering can only be realized by using hardware acceleration devices like GPU [17]. To render a 2D projection of the 3D data set, a model

view matrixwhich defines the camera position relative to the volumeand an RGBA (red, green, blue, alpha) transfer functionwhich defines the RGBA value for every possible voxel valueare required. In this study the structure and flow velocity volume rendering shared the same modelview matrix controlled by the user for people to easily correlate the structure and flow image. An identical jet color map used when performing the phase value to color mapping with opacity equaling 0.2 was applied as the transfer function for flow velocity volume rendering. Another color map varying from black-red-yellow-green with opacity 1.0 was applied as the transfer function for structure volume rendering. Each volume data set consists of 500×256×512 voxels. Two 512×512 pixel size 2D projection images will be generated after volume rendering.

3.3.3 Results and Discussion

Prior to any structure and Doppler imaging, it was necessary to characterize the phase noise properties of our SD-OCT system. We calculated the phase variation by imaging a stationary mirror at 70 kHz A-scan rate without any averaging process. The result is shown in Figure 3.10 The standard deviation of the Gaussian fitting curve was 65 mrad. This value incorporates both the internal system and external environmental phase noises.

To evaluate the system performance, we first performed a set of experiments using a phantom microchannel having a diameter of 300 μm with bovine milk flowing in it.

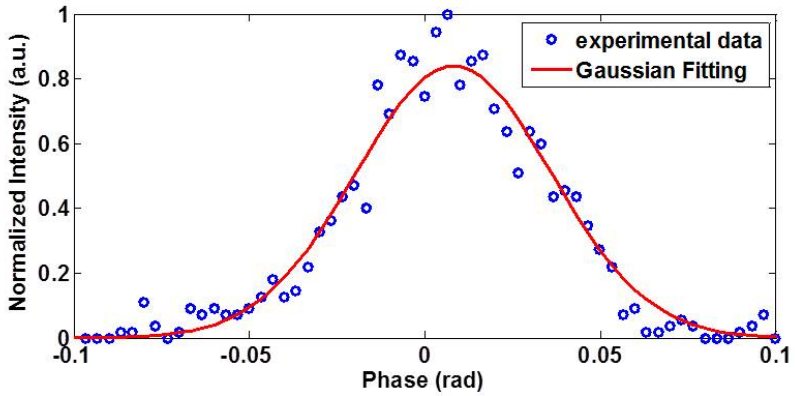

Figure 3.10: Normalized phase noise measured from a stationary mirror.

The microchannel was fabricated by drilling a 300 μm channel on a transparent plastic substrate. The flow speed was controlled by a precision syringe pump. During the experiment we obtained B-scan images, each containing 1000 A-lines covering 0.6 mm.

Figure 3.11 shows the effect of our adopted phase-resolving process described in the Methods section. The pump speed was set at 45 $\mu l/min$ with a Doppler angle of 70°, which corresponded to an actual average flow speed of 8.3 mm/s and 2.8mm/s speed projection on the incident beam. As can be seen in Figure 3.11(a), the raw image contains background having a lot of random phase variation. After filtering out the image with an intensity-based mask, Figure 3.11(b) becomes much cleaner. Then an averaging window 66 was convolved with the image to form the final image, Figure 3.11(c). We can clearly see the signal-to-noise ratio improvement using these processing techniques. Figure 3.11(d) is the result using only the averaging process. We can clearly see the advantage of combining intensity-based masking and averaging.

It is also worthy pointing out that an image with a clean background or high signal-to-noise ratio is critical to the next volume rendering process, as these random and rapid variations of the phase will accumulate due to the nature of the ray-casting process.

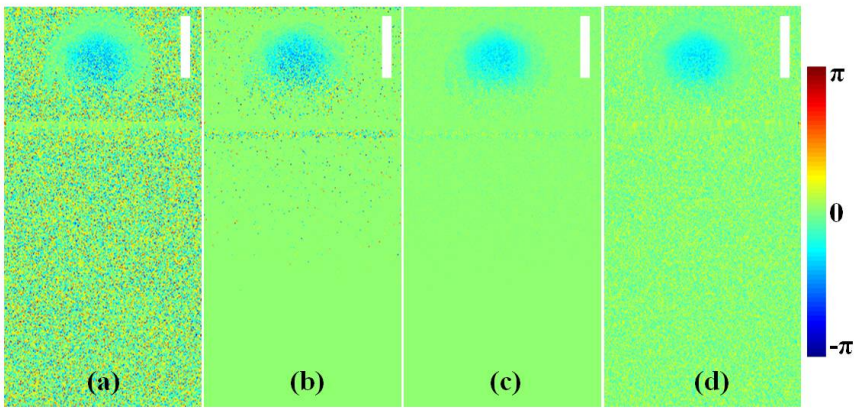

Figure 3.11: Illustration for intensity-based mask and averaging of phase images: (a) raw phase image without any processing, (b) phase image after mask thresholding, (c) phase image after mask thresholding and averaging, (d) phase image after only averaging (scale bar: 300 μm).

Choosing the ideal intensity threshold value to generate the phase mask is important, as a lower threshold value would have less effect on generating a clean background, and a high threshold value would cause structure information lossespecially in situations such as when the intensity is low due to the shadowing effect of blood vessels while the flow speed is high. In this study, the threshold value was manually selected based on visual perception. Setting the pump speed at 0.8 ml/h, Figure 3.12 illustrates the effect of different threshold values. The threshold value was used after the

image intensity was transformed into log-scale. As can be seen from Figure 3.12(a), when the threshold value increased from 5.0 to 5.8, the background became cleaner, as expected. Figure 3.12(b) shows the phase profile along the red line marked in Figure 3.12(a). We can see the decrease in the noise level of the background when the threshold value was increased while the signal region profile was the same; however, we can also see that the area of signal that indicates that the flow region shrank. To further evaluate the quantitative flow speed measurement of our system, we set the pump at five different speeds: 0 $\mu l/min$, 30 $\mu l/min$, 60 $\mu l/min$, 90 $\mu l/min$, and 120 $\mu l/min$. The cropped screen-captured structure and phase images to emphasize the flow region are presented in Figure 3.13(a). As the pump rate increased, we can see the color varied from light blue to deep blue. Experimental phase profile along the center of the microchannel and the parabolic fitting curves are shown in Figure 3.13(b). Note that at 0 $\mu l/min$ pump rate, there was still a small amount of flow signal above our system phase noise level and the profile was almost flat. We suspect that might be due to the gravity caused by moving of the scattering particles.

We then performed 4D simultaneous structure and Doppler flow imaging. The camera was operating at 70 kHz A-line rate. Each B-mode image consisted of 1000 A-scans in the lateral fast X scanning direction. The volume consisted of 256 B-mode images in the lateral slow Y scanning direction. The displayed B-mode structure and flow images were 500×512 pixels; both were reduced by half in X and Z directions. Thus the volume data size was 500×256×512 (X×Y×Z) voxels, corresponding to a

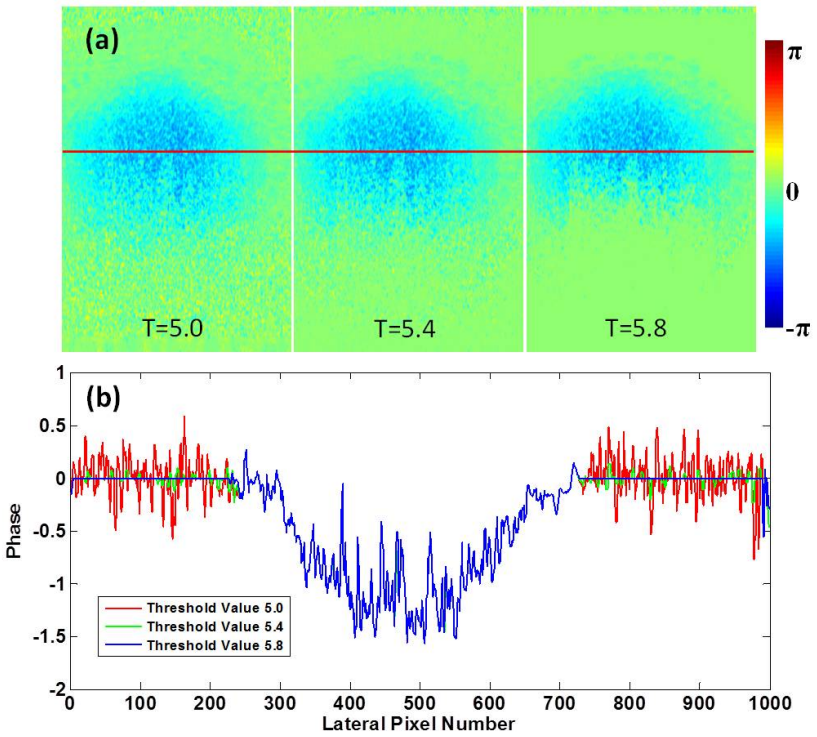

Figure 3.12: (a) phantom flow phase images showing the effect of different thresholding values: 5.0, 5.4 and 5.8 (b) phase profile along the red line in (a).

physical volume size 0.6×1.0×1.2 (X×Y×Z)mm^3 . It takes 3.66s to acquire such volume data. The results are shown in Figure 3.14. The red box is a screen-captured image of our customized program display zone. The name of each image was marked out at the bottom of each. To show the flexibility of our volume rendering method, two more screen-capture imagesdisplaying only the volume velocity and structure image region under isotropic and front vieware also displayed. Since the microchannel was fabricated using a diameter 300 μm drill bit on a transparent plastic substrate, the microchannel was not perfectly circular; we can clearly see from the velocity volume image that the velocity field distribution along the channel direction is not

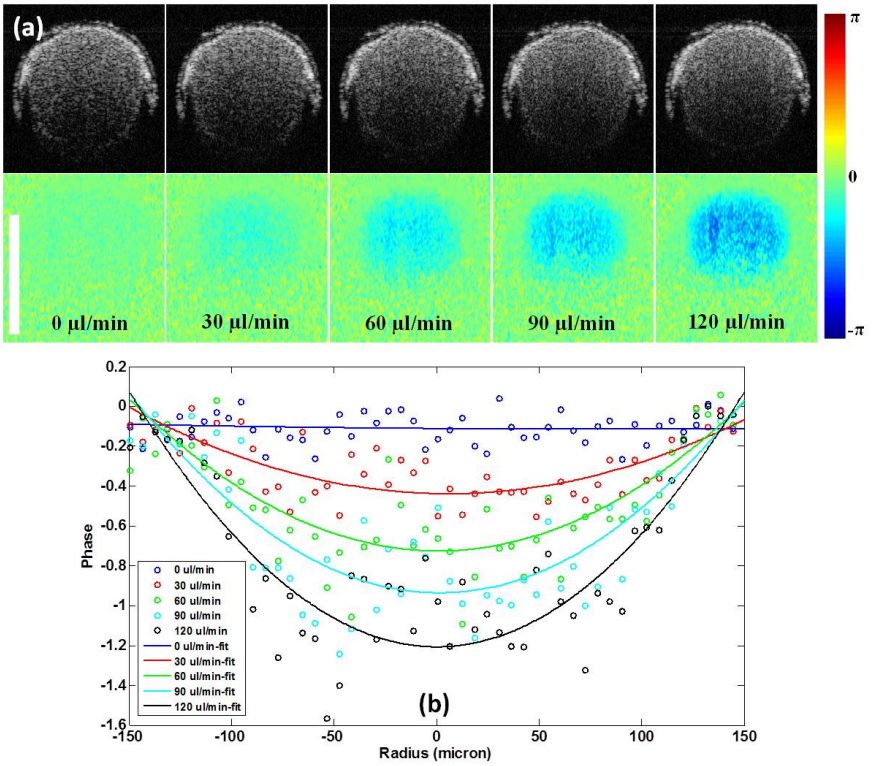

Figure 3.13: (a) Zoomed screen-captured B-mode structure and phase images of a 300 m microchannel with different flow velocities. Doppler angle: 85°. (b) Phase profile along the center of the microchannel with parabolic fitting.

uniform. This could essentially provide much more information than solely two-dimensional cross-sectional images. By sharing the modelview matrix between the flow and structure volume, it was easy to visually correlate these two images.

The time cost of all GPU kernel functions of a previous system data acquisition, processing, and rendering setup is shown in Figure 3.15. CUDA profiler 4.0 from CUDA Toolkit 4.0 was used to analyze the time cost of each kernel function of our GPU program. The data shown in Figure 3.15 are based on an average value of multiple measurements. As shown in Figure 3.15(a), the total time cost for a B-mode

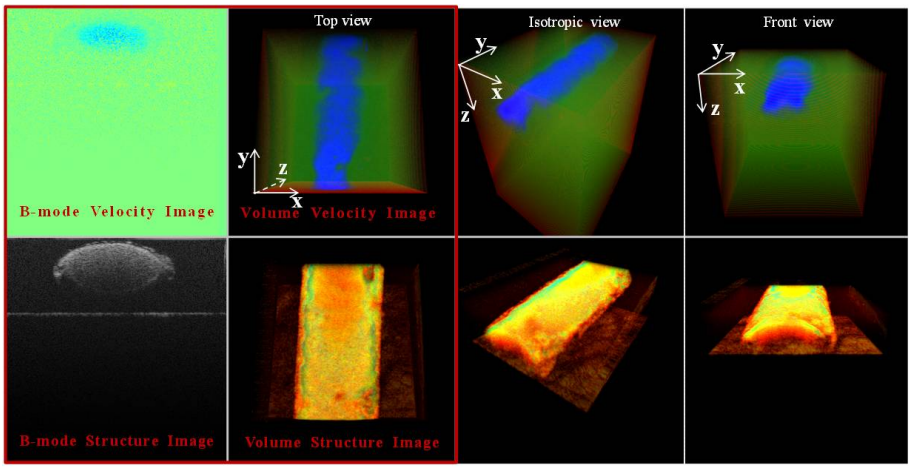

Figure 3.14: Phantom volume rendering: red box indicates the screen-captured image of the program display zone and volume rendering images under top, isotropic, and front views.

image size of 1000×1024, corresponding to 1000×2048 raw spectrum size, was 4.02 ms. Among them, phase calculation, averaging and color mapping took only 0.46 ms, which was about 11.4 percentage of the GPU1 computation time. We did not see too much host-to-device bandwidth limit here. For the volume rendering task on GPU2, however, copying the volume data of both structure and flow from the host to the device took 45.9 ms. The strategy to reduce this memory copy cost includes future hardware upgrades into a higher speed PCI-x16 3.0 from 2.0 host-to-device interface and a more powerful CPU. Instead of copying all the volume data at one timewhich is the case in our current setupanother effective solution would be to divide the copy task into multiple times for example every 20 B-frames while the acquisition was continuing to hide the latency of memory data transfer. Further GPU program optimization using two streams for GPU1 and asynchronous data transfer mode to

hide the data transfer latency will be implemented in our future study. For 64bit operating systems that utilizing multiple GPUs from Tesla series can utilize peer-to-peer memory access function to bypass the host memory transfer. The ray-casting of two volume data sets cost 12.5 ms. Based on the measurement, our system could provide a theoretical maximum imaging speed of 249,000 A-scans per second.

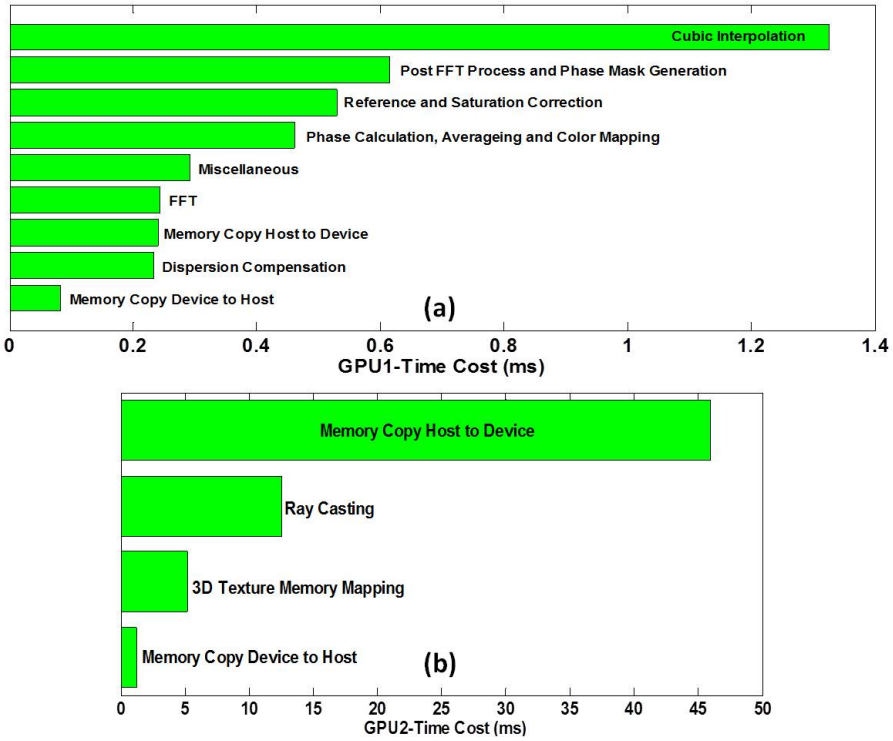

Figure 3.15: Processing time measurement of all GPU kernel functions: (a) GPU1 for a B-mode image size of 1000×1024 pixels and (b) GPU2 for a C-mode volume size of 500×256×512 voxels.

We further tested our system by in vivo imaging of chicken embryo to show the potential benefits of our system for non-invasive assessment of microcirculations within tissues. Here we used the chorioallantoic membrane (CAM) of a 15-day-aged chick embryo as a model. The CAM is a well-established model for studying microvascu-

lature and has been used extensively to investigate the effects of vasoactive drugs, optical and thermal processes in blood vessels, as well as retina simulation. Shown in Figure 3.16 are video frame sequences showing real-time chicken embryo blood flow with an imaging rate of 70 fps. From the structure image we can clearly see the blood vessel wall, chorion membrane. In the velocity image we can clearly identify two blood vessels; one is flowing with larger speed than the other. It was also evident that blood moved at different speeds within the vessel. The magnitude of the blood flow was maximal at the center and gradually went down to the peripheral wall. From this video we can clearly observe the blood flow speed variation over time. Both vessel blood-flowing speed fields were modulated by the pulsation effect of the blood flow. C-mode imaging was achieved by scanning the focused beam across the sample surface using X-Y scanning mirrors. The physical scanning range was 2.4×1.5×1.2 (X×Y×Z) mm^3, while all the other parameters were the same as the previous phantom C-mode imaging. It took 3.7 seconds to image a volume; the volume rendering of structural and flow information were displayed right after the volume data set was ready, with a delay of only 64.9 ms, which could be further reduced. To the best of our knowledge, this is the first-time demonstration of online simultaneous volume structure and flow-rendering OCT imaging. Combining volume flow speed with structural volume images could be highly beneficial for intraoperative applications such as microvascular anastomosis and microvascular isolation. The rendering of flow volume would allow the surgeon to evaluate the surgical outcomes. Figure 3.17 shows the 3D

rendering and B-mode images of CAM imaging.

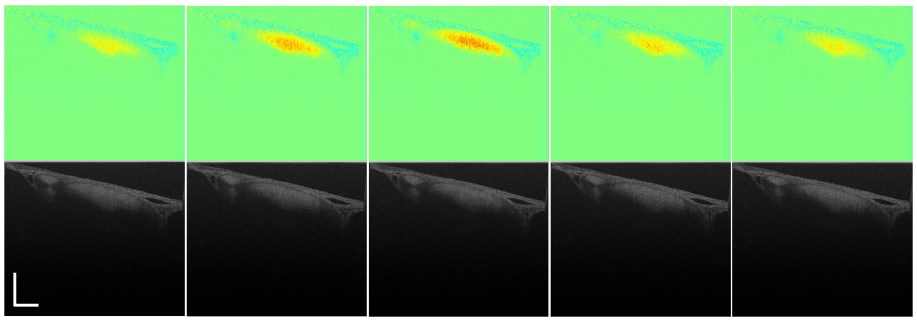

Figure 3.16: Real-time video image sequences showing the pulsation of blood flow of one vessel of chicken embryo membrane, imaged at 70 fps (scale bar: 300 μm).

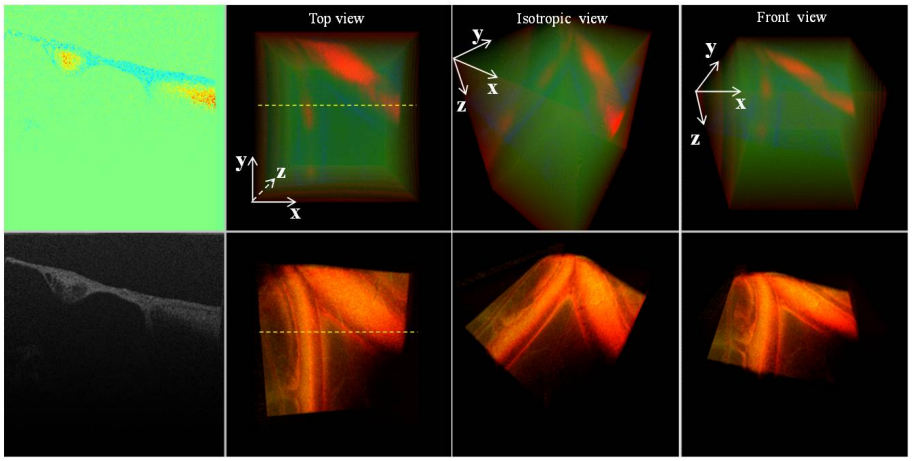

Figure 3.17: Screen-captures of simultaneous flow and structure imaging of CAM under different views; B-mode images correspond to position marked by yellow dashed line on the volume image.

To resolve the Doppler phase information, the B-mode image lateral direction needs to be oversampled. For example, in our system the lateral transverse resolution was 12 μmtypical for a scanning length of 2.4 mm; the oversampling factor of 5 needs to be applied. This requires 1000 A-scans for each B-scan. In our imaging one volume consists of 256 B-frames and the camera speed was 70,000 A-scans per second;

therefore, our volume imaging rate was 0.27 volumes per second, although our system could sustain a volume rendering rate of 15 volumes per second. If a higher-speed camera having 249,000 A-scans per second were used, the volume imaging rate would be 1 volume per second for the same volume size. As camera speed goes up, however, the minimum detectable flow speed will also go up. There is a trade-off between imaging speed and system flow sensitivity. The Doppler en-face preview method proposed in [51] is one possible approach to a solution to temporarily increase the volume rate before increasing the sampling area and sampling density, which will be incorporated into our system in future studies.

Chapter 4

Common Path OCT Applications

4.1 Motion Compensation for Fiber Bundle based Confocal Microscope

4.1.1 Introduction

Confocal microscopy is a well-established 3-D imaging technique with high lateral and axial resolution [78]. The concept of using fiber-optic component-based confocal microscopy has been demonstrated to show high stability, ease of use, and flexibility [79–81]. Flexible coherent fiber bundlesconsisting of tens of thousands of fiber channelshave been widely implemented for use in endoscopic confocal reflectance microscopy [82, 83], two-photon laser scanning [84], and optical coherence tomogra-

phy [85–87]. This design allows a scan-less probe and probe miniaturization. It also has the advantage of separation of the scanning end and sample end and miniature size. To improve imaging quality in vivo, a lens system must be customized and fitted to the fiber bundle. Confocal microscopy, based on a pair of GRIN lenses or objective lenses attached to a fiber bundle probe, has been studied [82, 88]. However, in vivo imaging of live samples can significantly degrade from the live sample motions due to breathing, heart-beating, blood-flowing, and other physiological activities. These result in intra- and inter-frame distortions, or even loss of the whole image frame [89]. For example, during the imaging of an embryo of a fruit fly during stem cell study, the accumulated muscle motion effect of the embryo can cause the imaging area to be completely out of the view. Motion compensation is critical to obtaining reasonable confocal imaging in vivo. Thus when video imaging is required, the probe can track the area of interest all the time keeping all the video images at focus. This work focuses on the axial motion compensation, which is crucial to obtain high resolution confocal images. Although lateral movement is negligible on restrained animal models and not considered in this work, image distortion caused by lateral motion can be corrected using a software method [90]. However without a clear at-focus image, it is impossible to perform the later software correction. Common-path optical coherence tomography (CP-OCT) has recently been demonstrated with its ability to precisely sense distance and has compact features for instrument integration [91]. In this paper, we implemented Fourier domain CP-OCT in a fiber bundle confocal microscope

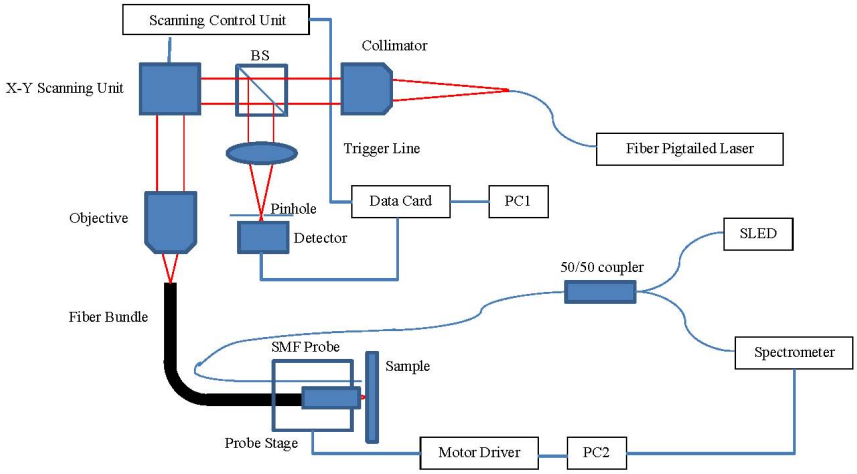

Figure 4.1: Schematic of the Motion Compensated Confocal Scanning System.

to compensate axial motion distortion in confocal imaging.

4.1.2 Experiment Setup

A fiber bundle probe terminated with GRIN lenses was assembled by gluing two GRIN lenses together at the distal end of a fiber bundle (Fujikura FIGH-10-500N, with an imaging diameter of 460 μm and 10k fiber cores) using UV curing adhesive. The average core size is 2.9 μm and the average pitch is 4.5 μm. We used the GRIN lenses (NT64-525, 0.25 pitch, N.A. = 0.55 and NT64-526, 0.23 pitch, N.A. = 0.55) from Edmund Optics. The length of the 0.25 pitch lens was 4.34 mm; the length of the 0.23 pitch lens was 3.96 mm. When assembled, Zemax simulation showed a working distance of 200 microns with a 1X image magnification. However, our experiment showed a working distance of 140×5 microns with a 1X image magnification for the

probe. This was due to the forming of a small gap between the two GRIN lenses during the assembling process.

We built an axial motion-compensated confocal microscope system by combining a fiber bundle-based confocal microscope with a CP-OCT distance sensor. The schematic of the whole system is shown in Figure 4.1. We used a fiber pigtailed diode laser (Meshtel, MFM-635-2S) with a wavelength of 635 nm as the confocal imaging light source. We used an objective lens (Olympus Plan N, 10X/0.25) as the collimator. A polarization-insensitive beam-splitter (CM1-BS013, Thorlabs) was used to direct the reflected signal beam onto the photon detector. The beam was coupled into the fiber bundle by an objective lens (Olympus Plan N, 20X/0.40). We used a focusing lens with a focal length f=60.0 mm and a pinhole of size 50 m in front of the photon detector. The 2D scanning Galvo Mirror System was controlled by a function generator (Tektronix, AFG30228), which also sent trigger to the data card (NI USB-6211, 16 Inputs, 16-bit, 250kS/s) to synchronize data acquisition. We used Personal Laptop (Lenovo ThinkPad T400, Intel Core2 Duo CPU @ 2.8 GHz) to acquire the image data.

A CP-OCT distance-sensing system was operated separately with the confocal scanning system. The light from a SUPERLUM Broadband Light Source (center wavelength: 878.6 nm, bandwidth: 180 nm) was coupled into a single-mode fiber by a 50/50 broadband coupler. The single-mode fiber probe was cleaved in a right angle to provide reflection at the fiber end. The Fresnel reflection at the fiber tip served

as reference light. A needle tube was used to protect the single-mode fiber reference surface by leaving a distance offset between the fiber inside the tube and the tube tip. The back-reflected/scattered light from the reference and the sample was directly coupled into the fiber and routed by the coupler to a customized spectrometer.

The fiber bundle scanning probe and the single-mode fiber probe were glued together at the probe stage, which was connected to the shaft of a high-speed linear motor (LEGS-L01S-11, Piezo LEGS). We used Workstation (DELL, Precision T7500) to obtain the distance information from the CP-OCT signal and deliver commands to the linear motor through a motor driver.

4.1.3 Motion Compensation Principle

The LEGS-L01S-11 has a 35 mm travel range, 20mm/s maximum speed, less than 1 nm resolution depending on different control modes, and a 10N maximum driving force. The CP-OCT system has an axial resolution of 3.6 micron in air and 2.8 μm in water. Using the peak detection, we achieved a position accuracy of 1.6 μm. To calibrate the position and validate its accuracy, we measured the peak position of the CP-OCT signal corresponding to the change in displacement of an ideal mirror placed on a precision translation stage in air. The result is shown in Figure 4.2. We can see that the distance sensing result has a very good linearity with the actual displacements. The effective distance-sensing can be larger than 1 mm, which is sufficient for the motion compensation. By linear fitting the curb we obtained the

calibration result of one pixel displacement equals to 1.6 μm displacement. As long as the OCT peak can be detected, the distance accuracy remains relatively constant. During our test the OCT peak signal was over 46dB above the noise floor. Even when the target is a biological tissue, distance sensing by peak detection has been shown to work well.

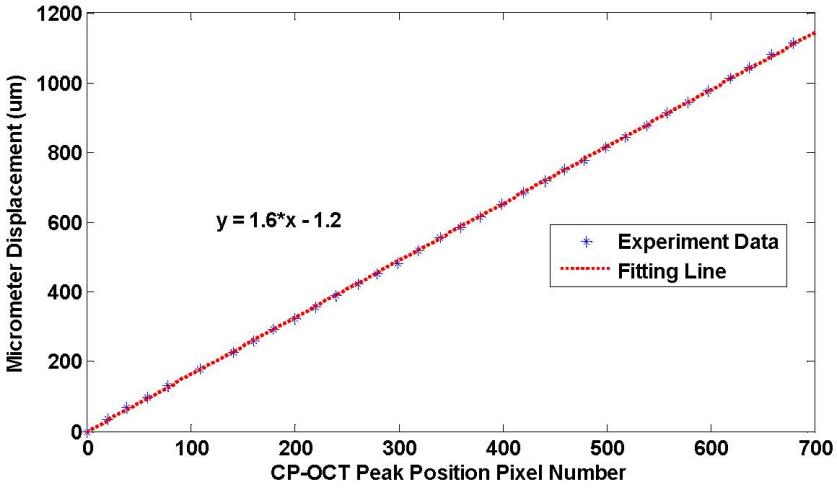

Figure 4.2: Fiber to mirror surface distance-sensing test.

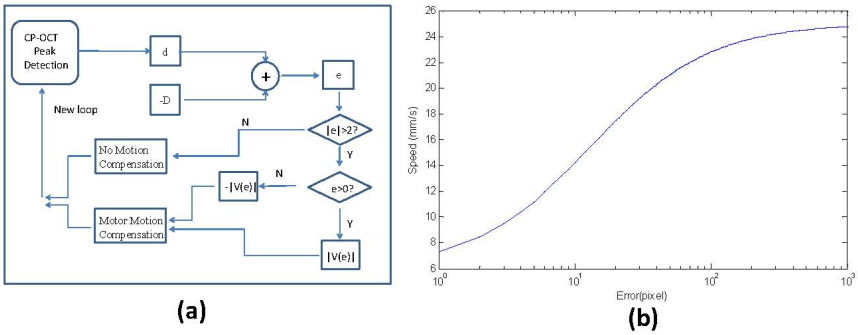

Figure 4.3: (a) System control flowchart; (b) Speed control curve.

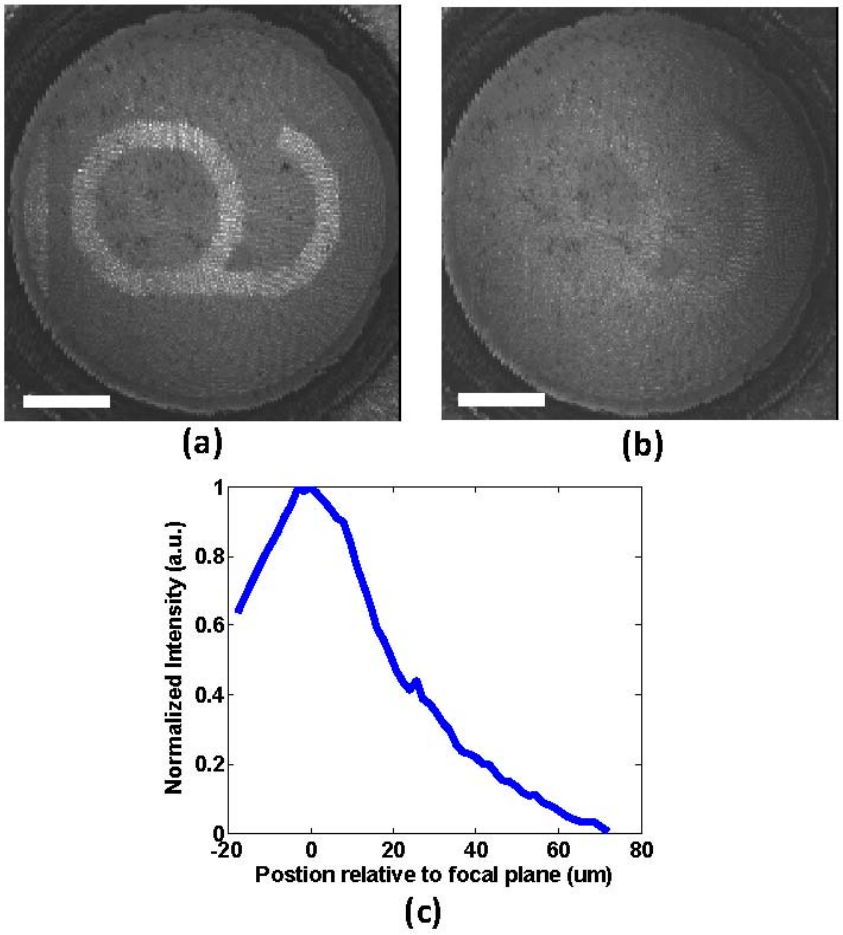

Figure 4.4: (a) Image in focus; (b) Image 50 microns out of focus; (c) Depth response of the confocal system, measured by moving ideal mirror along z axis.(scale bar: 100 μm).

The system control flowchart is shown in Figure 4.3(a). Ideal imaging distance D was predetermined while the CP-OCT sensor measured the actual distance, d. The error signal, e was defined as d minus D. If the absolute value of e is less than 2 pixel distance, the velocity of motor remains zero- there is no motion compensation. If the absolute value of e is larger than 2 pixels, the motor will be driven at a speed

proportional to that error. If the sign of e is positive, which means that the sample is moving away from the probe, the probe is driven forward. If the sign of e is negative, which implies the sample is moving towards the probe, the probe is driven backward. The relation between the velocity of motor and the magnitude of error signal is shown in Figure 4.3(b), which was experimentally optimized to make the motion compensation fast, accurate and stable. The sensor measures the distance again and the whole loop is repeated at the rate of 500 Hz. Therefore the CP-OCT distance-sensing system ran at 500 A-scan corrections per second and monitored the distance between the fiber bundle probe and the target at 500 Hz. When the distance varied over 3.2 μm, the computer sent a command to the motor to move the probe to minimize the distance error to zero.

4.1.4 Results and Discussion

The fiber bundle has 10k cores and the imaging plain was over-sampled 200 pixels by 200 pixels (460 μm by 460 μm) to follow the Nyquist Sampling theorem. To obtain good image quality, the data card was set at a sampling rate of 40k/s, which sets the imaging frame rate to 1 fps. NBS 1963A Resolution Target was used as test sample. The radius of Airy Disk $(R - a)$ of the optical system is calculated as

$$R_a = 1.22\lambda\frac{f}{D} = 11.6\mu m \tag{4.1}$$

Where D=4 mm is the radius of the collimated beam, f=60.0mm is the focal length of the lens right before the detector. Radius of our pinhole is 25 μm, which is 2.2 in normalized Airy units and is among the commonly used pinhole size [92]. The axial resolution of the confocal system was 40 μm, this was measured using a mirror as a target and moving the target along the axial direction of the confocal microscope. For an ideal confocal system, the through-focus axial response can be calculated by an equation: $[sin(w)/w]^2, \text{where} w = \pi z(N.A.)^2/\lambda$, z is the axial displacement to the focal point [82]. With a 0.2 N.A. focusing lens and 635 nm center wavelength, the ideal theoretical FWHM or axial resolution of the system is calculated to be 13 micron. The reason for discrepancy mainly comes from a relatively large size of the collection pinhole used in front of the detector, which has 2.2 Airy units. By choosing this pinhole size, we effectively suppressed the background and non-signal rays while maintaining a relatively high sensitivity. The peak signal to noise ratio measured using the mirror target was 22.57 dB. A typical SNR for the target imaging was 20.27 dB. When we moved the glass sample 50 μm away from the focal plane, the target 'number 6' completely disappeared, as shown in Figure 4.4

We placed the sample on a Newport XYZ 3D translation stage to simulate target movement. During image acquisition, the stage was driven back and forth along the axial direction of the probe. Without the motion compensation some part of the frame comes into focus while some part of the frame is out of focus (intra-frame distortion), shown in Figure 4.5(a). The consequence of the target movement is that

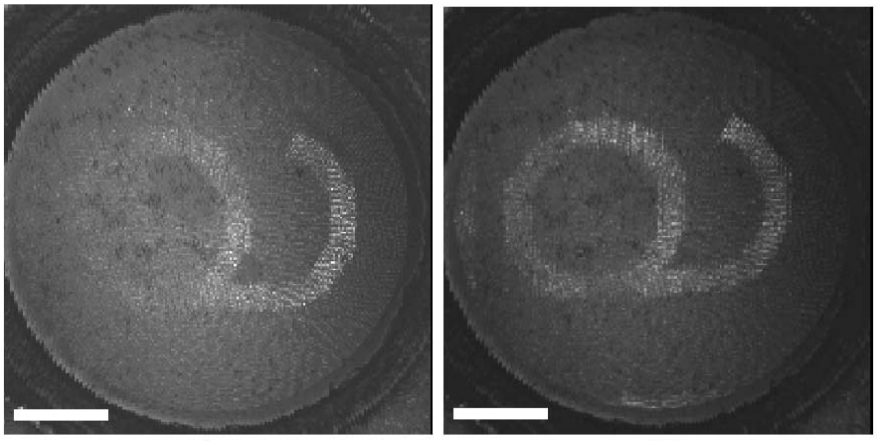

Figure 4.5: (a) Image without motion compensation; (b) Image with motion compensation. (scale bar: 100 μm)

some part of the image will be annulled by the depth discrimination of the confocal microscopy. With the motion compensation, the whole frame remains in focus, as shown in Figure 4.5(b).

To show the influence of the motion compensation on inter-frame distortion, two sets of images were recorded over 50 seconds as shown in Figure 4.6. Figure 4.6(a)-(d) presents four sequential images taken without motion compensation while the sample stage was periodically driven back and forth. Figure 4.6(e)-(h) shows four sequential images taken with the motion compensation. We can clearly see that the CP-OCT-based motion compensation system can track the focal plane effectively, providing clear, in-focus images. To further study the stability and precision of motion compensation, sample displacement relative to the focal plane without and with the motion compensation was recorded and plotted in Figure 4.7(a) and (b), respectively.

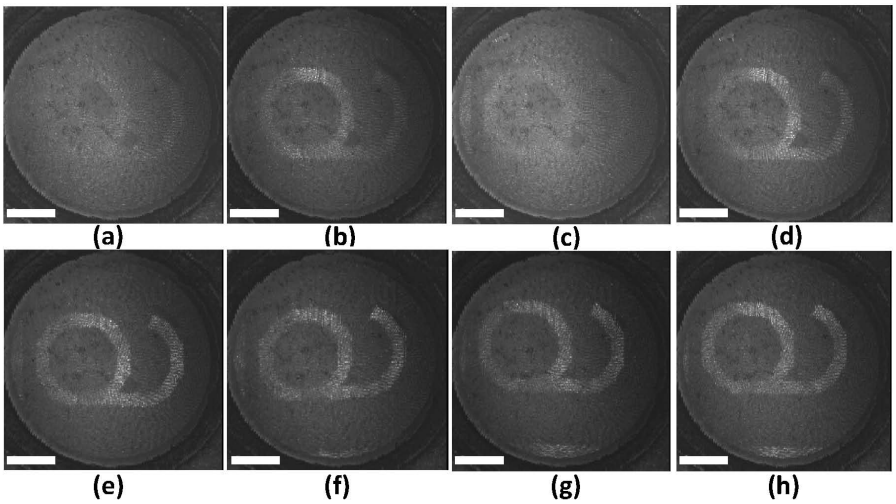

Figure 4.6: (a), (b), (c), (d) Sequential Images without motion compensation; (e), (f), (g), (h) Sequential Images with motion compensation (scale bar: 100 μm).

As shown in Figure 4.7(a), the average amplitude of the motion added to the sample stage was 60 micron and the frequency was 0.3 Hz. The average speed of the sample motion was 72 $\mu m/s$ during the test. This periodical motion added to the sample closely resembles physiological motions, such as breath of living animals. It took 2 ms for completion of each position correction cycle that was the single control loop time constant for the system. The theoretical maximum speed of the motion that the FD-CP-OCT system can compensate is analyzed below. Suppose at the time t=0, the sample is within the error scope, there is no motion compensation. After a loop time constant T_{loop} , speed of the sample υ_{sample} times υ_{loop} will be the distance error detected by the system, then the motor is commanded to move at a speed V_{motor}, the time it takes for the motor to catch up with the sample is $\upsilon_{compensation} = \upsilon_{sample} T_{loop}/(\upsilon_{motor} - \upsilon_{sample})$, Let $\upsilon_{compensation} = n \times T_{sampling}$ in order

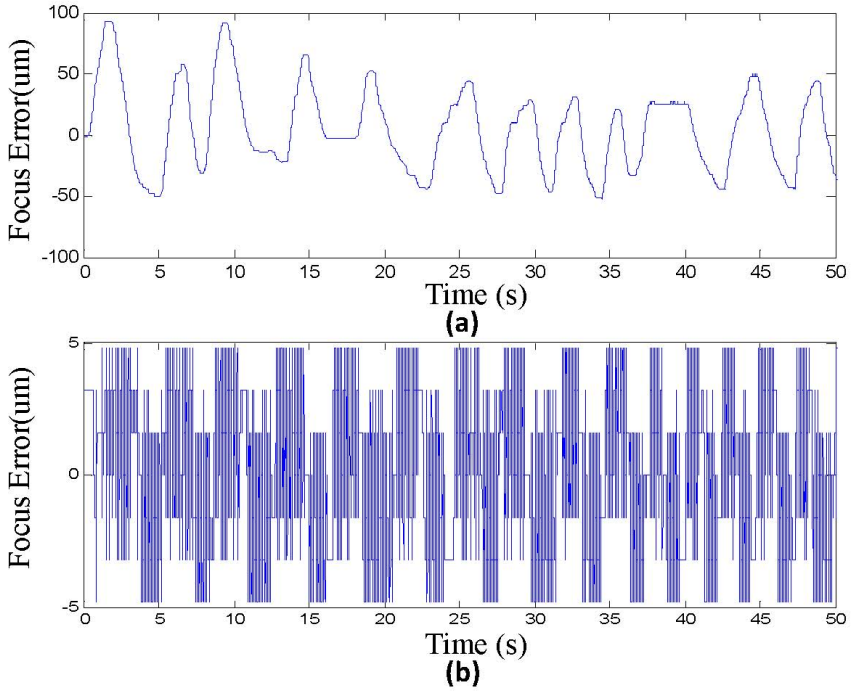

Figure 4.7: (a) Focus error (no compensation) variation with time; (b) Focus error (with compensation) variation with time: minus means toward probe, positive means away from probe.

to keep every n pixel at focus, we can get

$$\upsilon_{sample} = \upsilon_{motor} \frac{1}{1 + \frac{T_{loop}}{nT_{sampling}}} \tag{4.2}$$

$T_{sampling}$ is the acquisition time for each pixel. From this we can calculate the theoretical maximum sample speed that the system can compensate. If we want next pixel to be compensated that is n=1, in our system setup $T_{loop} = 1/500s$,$T_{sampling} = 1/40000s$, V_{motor} maximum=20 mm/s, we can get $\upsilon_{sample} = 247\mu m/s$. If n=2, $\upsilon_{sample} = 488\mu m/s$; n=5, $\upsilon_{sample} = 1.18mm/s$. Noticing that when n=1, the sample

displacement during that time is only 0.5 m, the image distortion for that pixel should be relatively small enough. Choosing motors that have higher speed and optimize the algorithm to decrease loop constant time would further improve the maximum speed that the method could compensate. When the compensation was on, as shown in Figure 4.7(b), the focus error was small and very stable, oscillating with maximum amplitude of 4.8 μm relative to the focal plane. Error jumps relatively high when the motion direction is changed, which is commonly known as over-shoot. Increasing the distance-sensing and correction rate above 500 per second would decrease the compensation over-shoot, which will be part of our future study.

Our work presented in this section focused on a proof-of-concept demonstration of the proposed method using a well-established resolution target as a sample. However, certain difficulties could be expected during in vivo imaging using this method. Since the distance sensor is sensing the edge of the microscopes field of view, the compensation error occurs when the target surface does not move uniformly. However, due to the small field of view (460×460 μm), such a motion non-uniformity is rare. In most cases the whole field of view moves together. For some samples, the external and internal layers do not move together, such as the heart of a fruit fly. The algorithm can be modified to track the motion of the layer of interest.

4.2 Novel *in-situ* Intraocular Lens Power Measurement

4.2.1 Introduction

Intraocular lens (IOL) implantation in refractive cataract surgery has become one of the most commonly performed surgical operations in medicine with more than 500 million IOLs implanted worldwide since the invention and first implantation of IOLs in 1949 [58] . Cataracts affect more than 20 million Americans over the age of 40 and every year more than 3 million cataract surgeries are performed [59]. These numbers will dramatically increase over the next 20 years as the US population ages [59]. Most of the cataract post-surgical device associated complications are directly related to some fundamental IOL optical properties such as dioptric power, reflected glare, light scattering, imaging quality, material refractive-index, thickness, and geometrical shape. The focal length (or IOL dioptric power) is a key parameter whose precise preclinical measurement is part of release specifications for all IOLs and is of critical importance to the safety and effectiveness of IOLs [60, 61].Currently, some conventional techniques for IOL dioptric power measurements are utilized, such as image magnification, autocollimation, nodal slide, Bessels method, Moir deflectometry, Talbot interferometry, and confocal fiber-optic laser microscopy [60–67] The effectiveness of most of these methods is often limited in terms of accuracy, spatial sample align-

ments, subjective image evaluation, and the dynamic range over which measurements can be performed (for both positive and negative dioptric powers). Moreover, three standard test methods for measurement of IOL dioptric power are specified by the International Standard, ISO 11979-2:1999 Ophthalmic Implants-Intraocular Lenses, Part 2: Optical properties and test methods [**?**] One of these standard methods is for determination of dioptric power by calculation from measured IOL dimensions including the sample surface radii and central thickness. For measurement of these basic IOL parameters, a specialized radius meter, micrometer or general purpose interferometer are recommended. These techniques, however, impose some limitations related to requirements for either a sensor-to-surface mechanical contact or complex and non-practical measurements for in-situ condition usage. In addition, the small size of IOLs also makes the measurement of surface radii highly demanding. Because of the complexity in correcting the IOL dimensions obtained under non *in-situ* conditions, alternative non-contact methods that could be performed in a wet environment (IOL in balanced saline solution) are of great interest. Optical coherence tomography is now established as a powerful and versatile tool for *in-vivo* optical biopsy [4]. It has been used to perform in-vivo quantitative corneal parameter extraction including anterior and posterior radii of curvature, central corneal optical power, and thickness maps of the cornea [68]. However, due to the scanner non-telecentricity or fan distortion14 of the scanning beam and the refraction at the corneal surface, algorithms for all those corrections were required to extract the correct parameters [68–71]. By

sharing reference and probe arm, the common-path Fourier domain optical coherence tomography (CP-FD-OCT) is a straightforward and effective technique that circumvents group velocity dispersion and polarization compensation to maintain a high axial resolution with a simple principal setup [72, 73]In this work, in order to avoid the fan distortion of the scanning beam, we have performed the scanning procedures using step motors. Furthermore, the fiber probe is immersed into the saline solution, thus the refraction of the light at the solution-air interface is avoided. Although there is limited adjustment on the reference arm light power to optimize the SNR [74], such a deviation from the optimized SNR is acceptable considering the advantages of CP-OCT. In this paper we demonstrate, for the first time to the best of our knowledge, a novel and simple CP-FD-OCT method for non-contact, accurate and objective measurement of IOL dioptric powers under in-situ conditions which could provide valuable information for standards, regulation and development.

4.2.2 Methods

The CP-FD-OCT method principal setup is illustrated in Figure 4.8. The IOL dioptric power measurement method is based on a digital IOL surface reconstruction by scanning a single-mode fiber probe along x and y directions utilizing two high-resolution linear motors. The IOL sample is fitted into a customized lens holder in a glass cuvette filled with balanced saline solution. The light from a Superlum Broadband Light Source (825.1-nm center wavelength, 67-nm bandwidth, 10 mW)

is coupled into a single-mode fiber by a 50/50 broadband coupler. The single-mode fiber probe is cleaved at right angle to provide Fresnel reflection at the fiber end which serves as the reference light. The power of the beam illuminating the sample was measured to be 630 μW. The single-mode fiber is placed into a fiber holder attached to a Newport XYZ 3D translation stage driven by high-resolution linear stepper motors (Newport 850G, 1 μm Resolution). The back reflected/scattered light from the reference and the sample is directly coupled into the fiber probe and routed by the coupler to a spectrometer (HR 4000, Ocean Optics) with 3648 pixel line-scan CCD detector, the exposure time is set at 6 ms to get a reasonable reference signal. Note that the relative smaller refractive index difference of the saline solution and the single-mode fiber requires longer exposure time than air-fiber interface. The CP-OCT system has a theoretical imaging depth of 2.2 mm in saline solution.

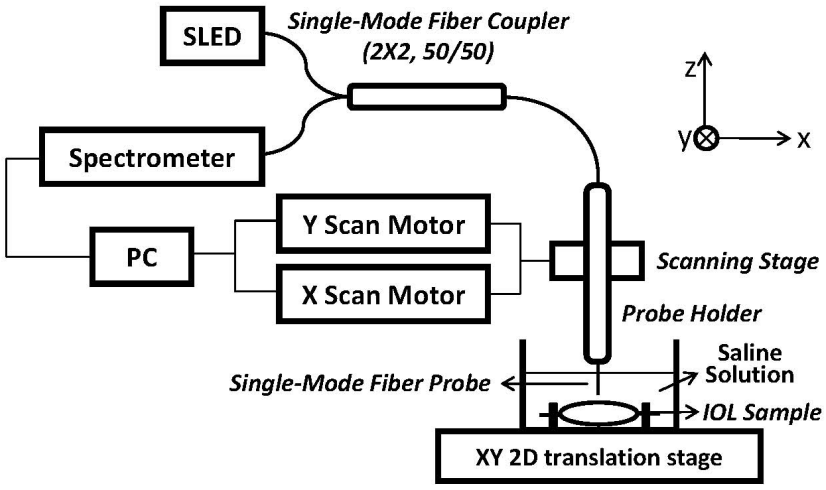

Figure 4.8: Schematic of the system setup.

The CP-OCT method provides the advanced feature of distortion-free in the sample arm beam geometry. The distortion effects are mainly caused by two sources: fan distortion of the scanning beam and light refraction in the air-saline solution interface. Figure 4.9a illustrates an one dimensional fan distortion, note that fan distortion occurs two dimensionally. The fan distortion will cause a flat surface to appear curved in the obtained image. When the light in the sample arm arrives at the air-saline interface with an incident angle other than zero, refraction will occur. As shown in Figure 4.9b, the actual optical path length (OPL) obtained, which the OCT system measures, is not the exact projection distance on the z-axis. Some specialized fan distortion and 3D refraction correction algorithms need to be applied to extract the correct curvature information of the sample. However, the CP-OCT approach is straightforward without fan distortion and refraction as shown in Figure 4.9c. The scanning surface of the fiber tip is a flat surface which is adjusted parallel to the plane of translation stage where IOL sample lies. Furthermore, the fiber probe is immersed into the saline solution, and thus, there is no refraction effect occurred at the air-saline interface. The fiber probe measures the exact distance along the z-axis from the probe tip to the IOL surface. The fiber tip is positioned as close as possible to the IOL surface in order to get a high SNR during the measurement.

After taking a Fast Fourier transform (FFT) of the interpolated spectrum data in linear k-space at each scanning point, distance between the reference (fiber probe tip) and IOL sample surface can be resolved with an accuracy of 1.22 μm by searching

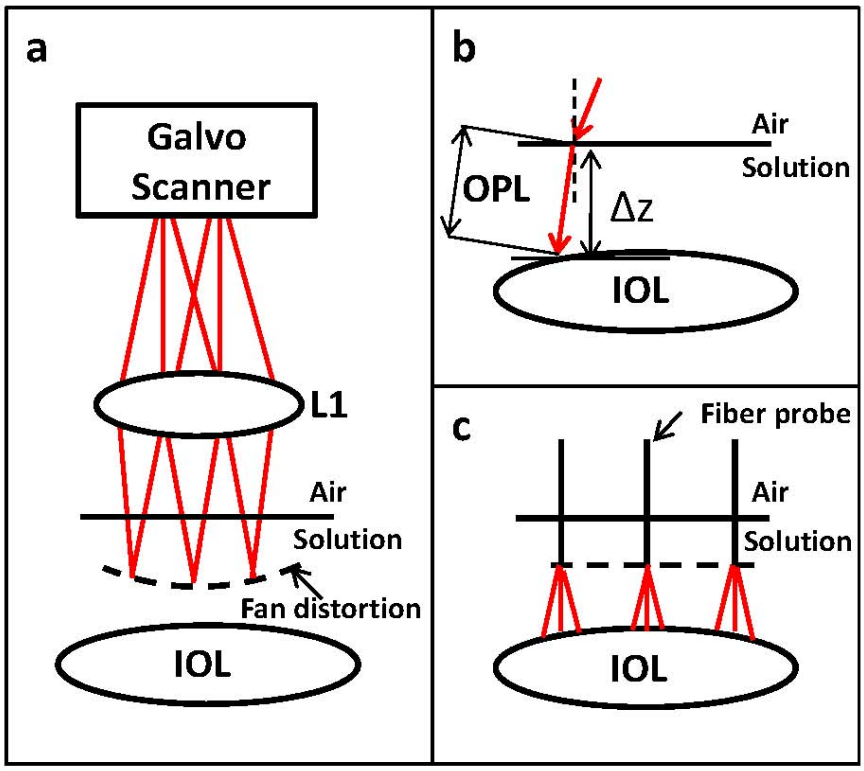

Figure 4.9: Comparison of 1D sample arm beam geometry of CP-OCT and standard Galvo scanner based OCT. (a) illustration of fan distortion in standard Galvo scanner based OCT; (b) illustration of distortion caused by the refraction at the air-solution interface; (c) illustration of CP-OCT scanning beam geometry. (Dashed line: trajectory of scanning beam; L1: focal lens; OPL: optical path length; z: projection of OPL on z-axis).

where the maximum peak signal of the A-scan data lies [75–77]. The accuracy is determined by the OCT system and refractive index of saline solution at wavelength around 825.1 nm. The peak position detection accuracy can be further improved by using zero padding technique to spectral data before FFT [74]. The peak position and system axial resolution is illustrated in Figure 4.10. In this case, accuracy higher than the axial resolution (5.1 μm in air/3.9 μm in saline solution) of the OCT system can

be achieved because there is only one boundary between the saline solution and the IOL sample. The maximum signal intensity comes from this boundary in the A-scan distance profile. By searching for the maximum signal intensity, we can determine where the surface lies. Thus, we can locate the peak signal position with a resolution of one pixel which corresponds to 1.6 μm in air and 1.22 μm in saline solution. These were calibrated by measuring the displacement of ideal mirror surface immersed in saline solution controlled by a high-precision micrometer using the OCT system, as geometrical distance needs to be corrected by the refractive index of the saline solution at OCT system wavelength band.

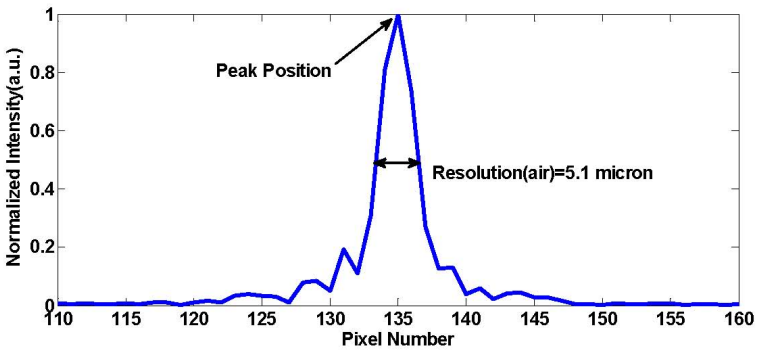

Figure 4.10: Illustration for peak-position and system resolution.

The lateral scan is carried out with a field of view centered on the highest point of the IOL sample surface. The size of field of view for 5D is 3×3 mm (150×150 points, step size is 20 μm), for 20D and 22D is 3×3 mm (100×100 points, step size is 30 μm) and for 36D is 1.5×1.5 mm (150×150, step size is 10 μm). The total acquisition time is proportional to the total sampling points. For a 150150 scanning protocol, the acquisition time is about 2.5 hours. The acquisition time can be significantly reduced

by modifying the scanning program, which is in progress now. Later, the radii of two IOL surfaces can be calculated after a digital construction. The OCT signal intensity decays when the distance between the surface and the fiber tip increases, as the beam coming out of the fiber probe is divergent. A 20 dB decay of the OCT signal intensity from depth 100 μm to 500 μm was observed by using a mirror as the sample. The CP-OCT system has a sensitivity range of around 70 dB over a distance of 2 mm. The glass cuvette is placed on an XY 2D translation stage. By adjusting the sample position and the height of the scanning stage, the probe can be positioned pointing to the center of IOL sample. Then sample stage is moved back a distance of half of the length of field of view along the x and y directions, and the scan is initiated. Following the completion of the first IOL surface scan, the IOL is flipped over and identical procedures for the second surface are repeated.

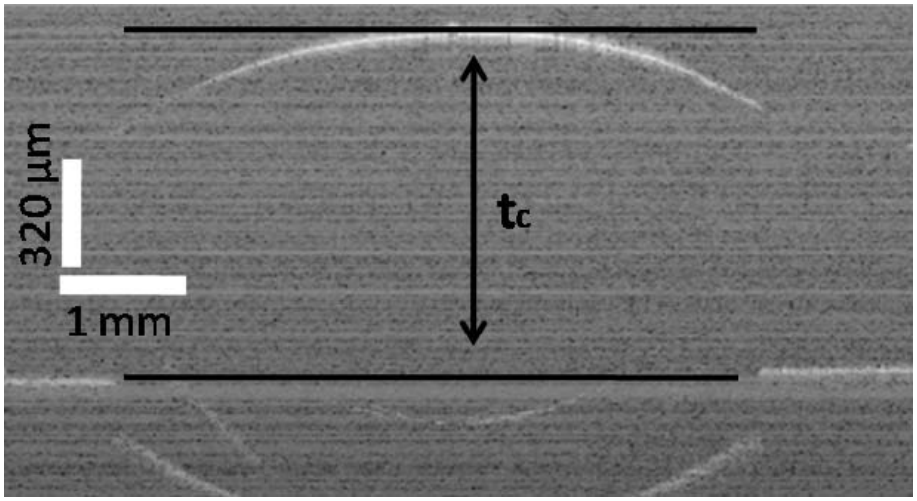

Figure 4.11: B-scan Image in air with the lens resting on a flat plate, that the upper arc is the anterior surface of the lens and that the rear surface is located by the plane of the back plate. (Two horizontal black lines indicate the thickness of IOL,t_c)

Due to the limit of identifying two surfaces of the IOL during a single scan in wet condition, the thickness of the IOL is measured in air. For the thickness measurement, one B-scan image is shown in Figure 4.11, which is cropped to show the area of interest. It is in log scale along the axial direction to accommodate details far away from the probe. The physical central thickness of the IOL sample tc can be resolved by two horizontal black lines marked in the image. The bottom black line indicates the surface on which the IOL sample rests [77]. Artifacts below the bottom line are ghost images due to the multiple reflections. A typical in-vitro B-mode image of the IOL sample in wet condition is shown in Figure 4.12 in linear scale, which is also cropped to show the area of interest.

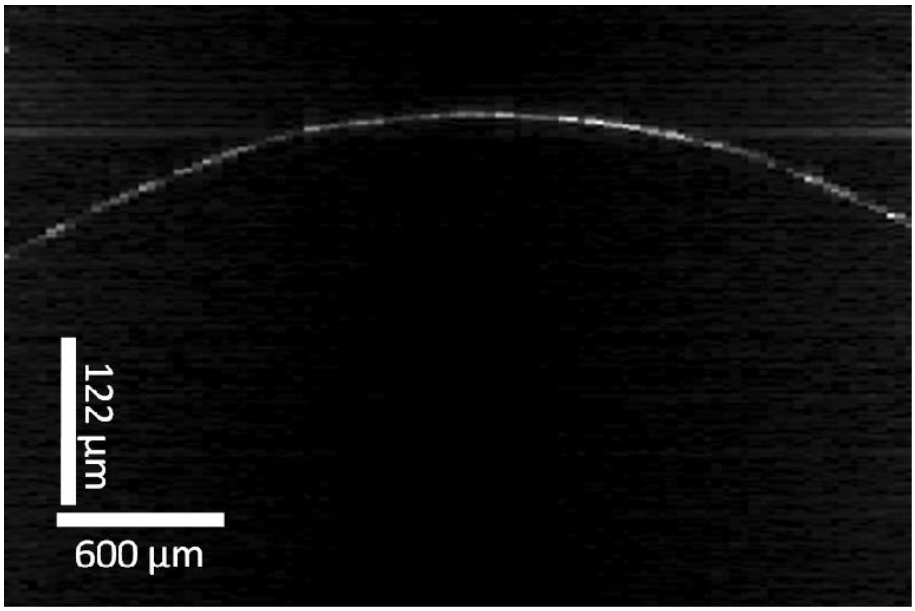

Figure 4.12: A typical in-vitro B-mode image of the IOL sample consists of 100 A-scans.

The key CP-FD-OCT method idea involves the specific use of motor driving scan-

ning common-path Fourier domain optical coherence tomography, which has the following advantages: (1) The scanning beam field forms a flat plane when the fiber tip is driven two dimensionally. This flat plane guarantees that the curvature calculated from the measurement is accurate. An alternative procedure uses the mirror scanning set-up, which is another commonly used method to perform beam scanning in FD-OCT. However, in this case, the scanning beam field has intrinsic curvature. Hence, we chose the motor driven scanning to remove curvature error. (2) By creating a reference from the single-mode fiber tip, the group velocity dispersion and polarization mismatch between the reference and sample arms are circumvented in real time. Dispersion and polarization mismatch is caused by the sample and saline solution only. However, the mismatch over a distance of 1-mm thick saline solution is negligible. (3) It is a completely non-contact method, and therefore has no effect on the IOL sample. (4) It is an in-situ measurement method. Due to the small size of the single-mode fiber probe, which has a diameter of 50 μm after removing the cladding and the mechanical hardness of the probe, it can be inserted into the saline solution for a long time while maintaining the shape and reference easily. (5) Measurement environmental conditions can be easily maintained at a stable stage due to the small size of the fiber probe inserted into the solution and the slow motor driving speed, 0.1 mm/s, used in the experiment. (6) Surface reconstruction can provide valuable information to improve standards and regulations, since the radii of front and back surfaces are calculated separately.

For further data analysis, we utilize the following procedures. First, we construct the measurement surface using a peak detection method for each A-scan shown in Figures 4.13(a) and Figures 4.13(b). Second, we perform a 3rd degree polynomial surface fitting using the toolbox in Matlab 2010b. Points that deviate over ten microns from the fitting surface are excluded from the fitting data to improve the accuracy of fitting, shown in Figures 4.13(c) top. Residuals of the fitting and experimental data are presented in Figure Figures 4.13(c) bottom. Third, the lowest point (x_0, y_0) of the surface is calculated based on the polynomial fitting equation. Using parameters up to the second order of the equation and the condition for a minimum value, the start point (x_start, y_start) can be calculated. Then, the lowest point (x_0, y_0) is searched around the start point. Fourth, according to geometric mathematics, the surface mean radius can be calculated at the point (x_0, y_0) using the geometric mean of radius along two directions shown in Figures 4.13(d), since the IOL is not perfectly spherically symmetric. Finally, with both of the radii and index known, the dioptric power can be determined using the following formula:

$$D = D_f + D_b - (t_c/n_{IOL})D_f D_b \tag{4.3}$$

where D is the dioptric power,

$$D_f = (n_{IOL} - n_{med})/r_f \tag{4.4}$$

$$D_b = (n_{med} - n_{IOL})/r_b \tag{4.5}$$

n_{IOL} is the refractive index of the IOL optical material (1.459) which is normally provided by the manufacturer,n_{med} is the refractive index of the surrounding medium (1.335), r_f and r_b are the radii of the front and back surface of the lens respectively, and t_c is the central thickness of the IOL.

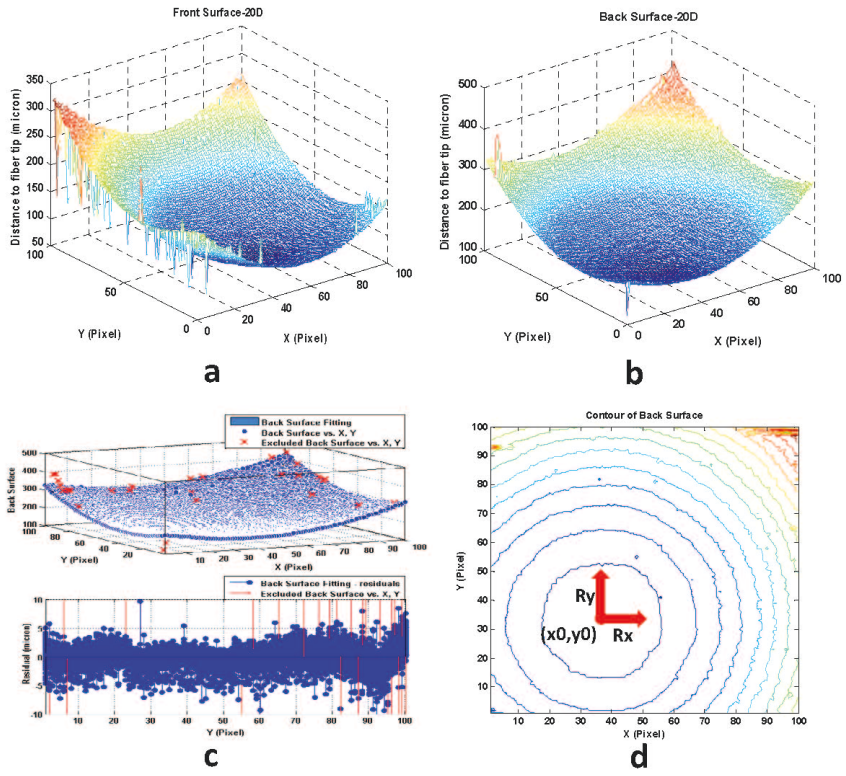

Figure 4.13: (a) front surface of 20D IOL sample constructed by peak position detection of each A-scan; (b) back surface of 20D IOL sample constructed by peak detection of each A-scan (blue to red indicating low to high); (c) top: 3rd degree polynomial surface fitting of the experimental data of back surface; bottom: residuals of the fitting; (d) mean radius of surface is the geometric mean of radius along two directions (Rx and Ry) shown in a contour image of the back surface.

4.2.3 Results and Discussion

The IOL dioptric power is now determined in compliance with the International Standard, ISO 11979-2:1999 Ophthalmic Implants-Intraocular Lenses, Part 2: Optical properties and test methods. Basic requirements for the measurement methods are listed in the standard including the allowed tolerances on IOL dioptric power: 0.3D for the dioptric power range of 0 to $\leq$15D; $\pm$ 0.4D for >15 to $\leq$ 25D; $\pm$ 0.5D for >25 to $\leq$ 30D; and $\pm$ 1.0 D for > 30D.

Using the proposed measurement system and procedures described above, we tested four IOL samples with positive dioptric power of 5D, 20D, 22D and 36D, which are among in practice low-, middle- and high-range IOLs that are commonly used. The measured average values of these four lenses are 4.95/20.11/22.09/36.25 D, respectively, based on five measurements. The repeatability is estimated by the standard deviation (SD) of these five measurements, which is 0.1/0.18/0.2/0.58 D for 5/20/22/36 D IOLs, corresponding to a relative error of 2/0.9/0.9/1.6 percentage for four lenses, respectively. Although the SD is relatively larger compared to 0.03D [**?**]/0.15D [66] obtained by using other conventional test methods, the SD of the new method is well within the allowed tolerances of the ISO Standard. Moreover, as a non-contact and in-situ compatible approach, the new method can provide additional unique information about the IOL sample, such as the front and back surface radii separately and the central thickness, which turns out to be of great interest to improving the product efficacy and safety. Furthermore, a significant advantage of this

method is the absence of evident limitations in using it to test various IOL samples in terms of dioptric power range, negative/positive powers, hydrophilic/hydrophobic and recently developed new IOL designs. In addition, some other IOL optical properties may also be calculated from the digital surface reconstruction, such as aberrations, though not a main task of this article.

The CP-FD-OCT method accuracy of IOL dioptric power measurement depends on the following basic factors. (1) OCT system sensitivity: The accuracy of determining the peak position of each A-scan is critical to the digital surface reconstruction. However, sensitivity of OCT system degrades as the probe moves away from the sample surface. The error increases when the probe goes to the margin of the IOL scan, as the distance between the IOL surface and probe is increasing and the beam coming out of the fiber probe is divergent. It is important to position the IOL surface as close to fiber tip as possible. (2) Lateral scanning step size: The optical lateral resolution of the CP-OCT system varies over the depth as the beam coming out of the bare fiber probe is divergent. The lateral resolution is measured to be 7.5 μm when the sample is 100 μm away from the fiber tip. It goes up to 22 μm when the distance is 0.5 mm. During the measurement, the distance from the fiber tip to the IOL surface is usually within a 500 μm range. When the step size of the motor is larger than the optical lateral resolution, the system resolution is determined by the step size. When the step size of the motor is smaller than the optical lateral resolution, the IOL surface

is oversampled. At each lateral position we can obtain an averaged distance over the field of the optical lateral resolution, which should be the distance from the fiber tip to the center part of the field. During the measurement of IOL, the highly curved surface may prevent some signal within the resolution area being collected back through the fiber. Degradation of the resolution over the depth further decreases the signal intensity. This is the reason for the error to go up when the probe scans the edge area of IOL and for the error increase with the IOL dioptric power increase. In order to cover a large field of view including reasonable total sampling points, different step sizes were used depending on the dioptric power of the IOL samples. By reducing the step size, increasing the number of scanning points and performing zero-padding to the spectra data before FFT, a digital surface reconstruction with a higher accuracy can be achieved, and thus, providing more accurate radius calculation.

4.3 Motion Compensated handheld CP-OCT imaging

4.3.1 Introduction

In many circumstances, it is more convenient to use a simple hand-held, manually-scanned probe to obtain OCT images of tissues and organs which might otherwise be inaccessible using standard mechanical scanning heads [93]. A hand-held imaging

probe has the following advantages. First, it is small and lightweight, making it easy to access tight spaces. Second, surgeons are intimately familiar with hand-held instruments that can leverage their experience and skills with little training. Third, a small hand-held instrument offers greater safety because the surgeon can more easily override or remove the instrument in cases of malfunction [94]. Finally it offers the surgeon great freedom to obtain any image size, for example a larger field-of-view compared to those constrained by apertures of scanning lens or other endoscopic probes [95–99].

A hand-held probe, however, poses additional challenges over mechanically-rigid scanners. First, non-uniform motion of the probe during lateral manual scanning will cause image distortion and inaccuracy. Earlier work by Ahmed et al. and more recent work by our lab provide solutions to correct non-uniform scanning speed artifact using de-correlation of adjacent A-lines [93, 100]. Second, physiological tremor composed of low and high frequency amplitudes over 100 μm would cause large motion artifacts in acquired images [101]. Involuntary motions of a subject may also cause OCT imaging artifacts. Finally, the manual scan across and close to the target surface is highly riskyespecially involving fragile tissues. For example, in the context of retinal surgery, the retina is only 350 μm for humans, and tearing it can permanently damage eyesight. Scanning while maintaining a larger distance between the probe tip and target surface is not an ideal solution since that degrades image quality and the imaging depth is typically limited to 3-5 millimeters. While motion is in the form of both ax-

ial and lateral directions, axial motion is the primary concern due to its direct effects on the image quality. There have been methods used to compensate for the sample surface topology and axial motion in OCT to keep a good system sensitivity and image range, for example adaptive ranging technique for time-domain OCT (TDOCT) [102] and the reference mirror tracking method for spectral domain OCT (SDOCT) [103]. Common path optical coherence tomography (CP-OCT) is a simple, all-fiber-based technique that shares reference and probe arm which circumvents group velocity dispersion and polarization compensation [72]. With all-fiber setup it has been widely studied for various medical applications because it can be arbitrary long, which is of great importance in the clinical environment [73, 104, 105]. Recently, CP-OCT has been demonstrated for surface topology and motion compensation [91] and a conceptual micro-incision tool [106], and novel microsurgical tool platform which is called SMART (smart micromanipulation aided robotic-surgical tool), active tremor cancellation based handheld vitreoretinal microsurgical tool [107].

In this work, we developed and studied a CPOCT-based hand-held imaging system capable of motion compensation in the axial direction. A prototype hand-held imaging probe that housed a piezoelectric motor and an imaging fiber tip has been fabricated and tested. Distance from the fiber tip to the imaging target was monitored and adjusted by the corresponding feedback control of the motor. In principle the mechanism utilized to compensate axial motion is straightforward and similar to adaptive ranging or the reference mirror tracking method. However, combining this

mechanism with a spectral domain CPOCT system by moving the imaging tip solved the problem of degraded lateral resolution with increasing imaging depth. Ten times zero-padding of the A-scan spectrum was used to increase the distance sensitivity to 0.16 μm in our system, thus yielding better motion compensation performance. Graphical user interface, real-time data processing, and visualization based on a CPU-GPU hybrid programming architecture [16, 28] were also developed. Hand-held manual scan images of two artificial phantoms, human hand palm, finger nail and ex-vivo bovine retina were obtained. We used a cross-correlation maximization based shift correction algorithm for topology correction to provide anatomically correct images to surgeons, since the system flattens the acquired image. The system was able to track the sample surface with a rate of 460 Hz and the root-mean-square (RMS) error of a hold-still task was measured to be 2.93 μm. To the best of our knowledge, this is the first time that a probe capable of compensating axial motion for image formation in hand-held manual-scanning OCT being reported.

4.3.2 Methods

4.3.2.1 System configuration

The system configuration and schematic diagram of the prototype probe are shown in Figure 4.14(a). A right angle cleaved single-mode fiber was inserted into an inner needle with a slight recession to protect the fiber end facet. The inner needle (25-

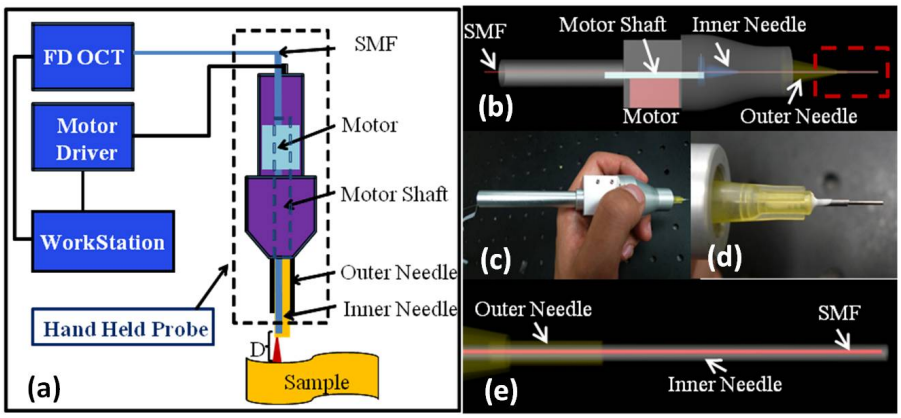

Figure 4.14: (a) schematic of system setup; (b) illustration of design of the probe; (c) probe prototype held by hand; (d) zoomed view of the probe needle tip; (e) zoomed view of the dashed red box in (b).

gauge, BD Syringe) was attached to a piezoelectric linear motor while the outer needle (20-gauge, BD Syringe) was used to guide the movement of the inner needle [26]. The motor and CP-OCT system formed a closed-loop control system. A design illustration of the prototype probe used in this study is shown in Figure 4.14(b) and a photograph of the prototype probe is shown in Figure 4.14(c). The length of aluminum probe is 140 mm excluding attached needle; its weight is about 65 g. Such a light weight gives the surgeon negligible burden to move it around. A zoomed view of the probe needle set tip is shown in Figure 4.14(d) and Figure 4.14(e).

We used a fiber pigtailed 635 nm red diode laser (Meshtel, MFM-635-2S) as a guide. Light from a SUPERLUM Broadband Light Source (center wavelength: 845 nm, bandwidth: 105 nm) was coupled into a single-mode fiber probe by a 50/50 broadband coupler. The distal end of the single-mode fiber (5.6/125 μm Core/Clad diameter) probe was cleaved at a right angle to provide a Fresnel reflection that served

as the reference. The single-mode fiber reference surface was protected by leaving the fiber tip inside the tube. The back-reflected/scattered light from the sample was collected by the bare fiber probe and routed to an in-house-built spectrometer. We used a 12-bit, 2048 pixel CCD line-scan camera (e2v, EM4, USA) with a camera link interface as the detector of the home-built spectrometer. The minimum line period limited by the camera is 14.2 μs, corresponding to a maximum line rate of 70,000 A-scans/s. The spectrum data acquired by the camera is transferred to a computer through a frame grabber (National Instruments, PCI-E 1429). In the following experiment, each frame is an average of three A-scans; this was used for tracking the probe tip movement relative to the target surface. The eventual compensation rate of the system was determined by the frame rate of the system, which was less than the maximum line rate. The CP-OCT system has an axial resolution of 3.6 μm in air and 2.8 μm in water. Using the peak detection, we achieved a calibrated position accuracy of 1.6 μm [29]. To further increase the distance-sensing accuracy of the system, we applied the ten times zero-padding technique [30] to achieve a theoretical accuracy of 0.16 μm, sufficient for us to do the motion compensation. Please note that accuracy and resolution of an imaging system are different. Resolution describes the smallest separation of two targets that can be detected, while accuracy describes the smallest displacement of only one target that can be resolved. The lateral resolution depends on the distance from the sample to the fiber tip. The lateral resolution is 10 μm at 100 μm away from the fiber tip and increases almost linearly to 33 μm at 1.6 mm

away from the fiber tip while our system designed axial imaging range is 1.6 mm.

The single-mode fiber probe was then connected to the shaft of a high-speed linear motor (LEGS-L01S-11, Piezo LEGS). We used a quad-core Workstation (DELL, Precision T7500) to obtain the distance information from the CP-OCT signal and deliver commands to the linear motor through a motor driver. The LEGS-L01S-11 has a 35-mm travel range, 20-mm/s maximum speed, better than 1-nm resolution depending on different control modes, and a 10N maximum driving force. For our experiment, we used a motor with a step resolution of 0.2 μm. While A-scans were used to extract distances from the fiber tip to the sample surface, they were also stored to form M-scan images.

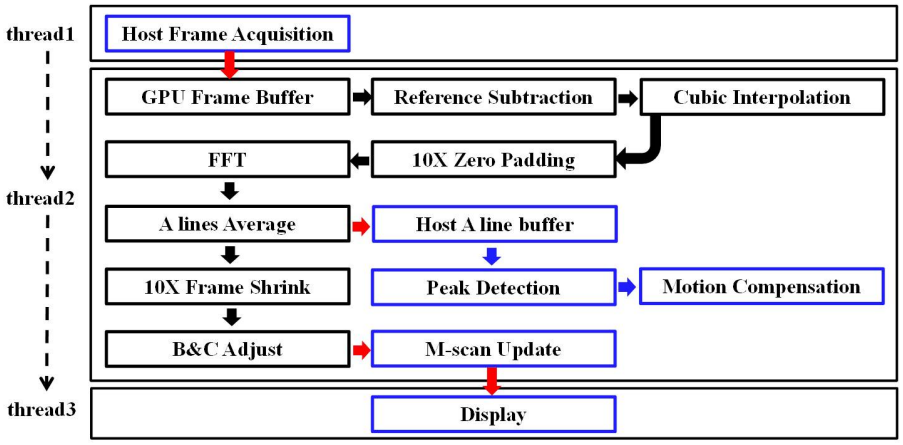

Figure 4.15: Data processing flowchart: red arrows indicate data transfer between GPU and host; blue arrows indicate processing flow in host; black arrows indicate processing flow in GPU; GPU kernel functions are outlined with black lines, and CPU functions are outlined with blue lines; dashed arrows indicate triggering between the three threads.

4.3.2.2 Motion compensation and M-scan imaging

During the hand-held operation, voluntary and involuntary movements of the hand and tissue sample causes the distance, D, between the fiber tip and the sample surface to deviate from the desired set-point, d_0, which causes a measured error $e = D - d_0$. Based on the measured error, e, a well-known feedback control approach using PID (Proportional, Integral and Derivative) gain was implemented to control the speed of the piezoelectric motor u_m to reduce the error:

$$u_m = K_P e + K_I \int e + K_D \frac{d}{dt} e \tag{4.6}$$

where K_P, K_I and K_D are respectively the proportional, integral and derivative gain coefficients and were empirically optimized.

We performed M-scan imaging while surface tracking and motion compensation were on. We implemented a real-time, graphical user interface that controls data acquisition, data processing, motion compensation, and image visualization based on a multi-threaded CPU-GPU hybrid programming architecture. The data processing flowchart of the proposed system is shown in Figure 4.15. Thread 1 handled the data acquisition from the spectrometer. Thread 2 performed the data processing and motion compensation. Thread 3 performed the image visualization task. Communication and synchronization between the threads are performed through an event-driven method. Computing tasks were distributed among GPU and CPU to take advantage

of both processors. Process steps that can achieve better performance through parallel computing were assigned to GPU (outlined by black rectangular), while process steps that require more logical computing were assigned to CPU (outlined by blue rectangular). After the raw spectrum was transferred to the GPU buffer, it was first subtracted by a pre-acquired physical reference spectrum, and then was cubic interpolated from the λ domain to the k domain. After that a ten times zero-padding was applied to the interpolated data to increase the distance sensitivity. Three A-scans of post-FFT data of the zero-padded spectrum were averaged to increase the SNR of the A-line data. Due to the ten times zero padding, the post-FFT A-line was shrinked back to normal size and then brightness and contrast adjustment was applied to the shrinked A-line for display purposes. Meanwhile the non-shrinked averaged A-line with higher distance sensitivity was transferred back to the CPU host for the purpose of peak detection and motion compensation. In the following test the CCD camera was running at 460 fps, which corresponds to a motion compensation rate of 460 Hz with 2.2 ms interval. This gives an effective sampling rate of 460 A-scans per second while the hand is moving the probe.

4.3.2.3 Topology correction

The motion compensation function of the probe tries to keep the distance between the imaging fiber tip and sample surface constant during the OCT imaging, which eliminates the motion artifacts due to hand and sample motions, and the sample

surface topology. While suppression of the hand and sample motions is desirable, removal of the surface topology is a side effect that needs to be addressed. The motion compensation algorithm includes Doppler velocity-based correction [108] and image structure intensity based position correction [109–111]. In this work, we performed the topology correction by shifting certain number of pixels (Δz) in the axial direction to maximize the cross-correlation between adjacent A-scans for its simplicity and effectiveness. This method was evaluated [109] for bulk image shifts (BISs) correction.

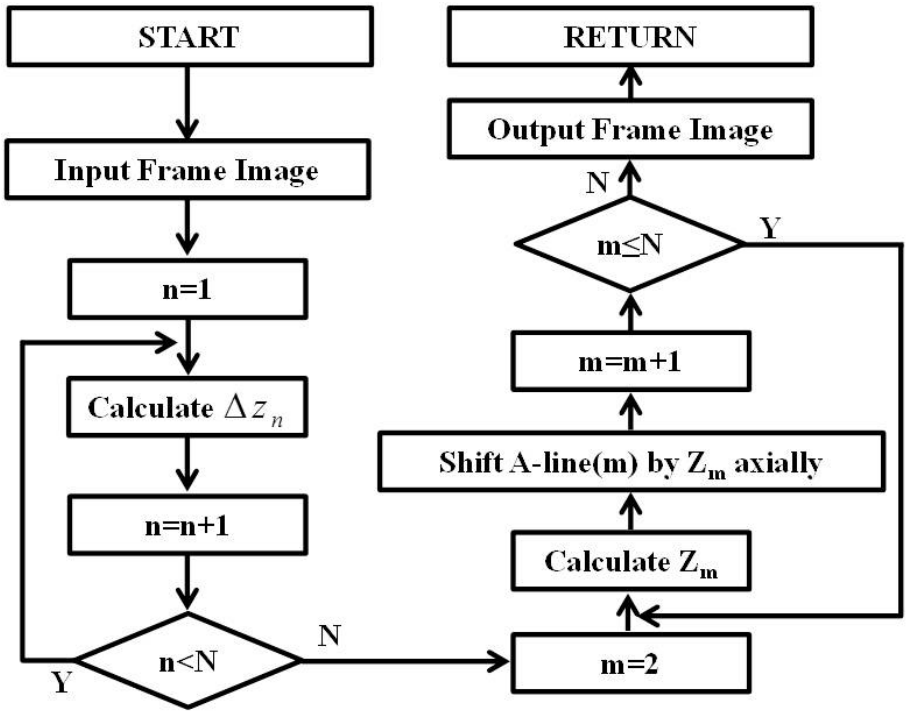

Figure 4.16: Pseudo-code of the cross-correlation maximization-based shift correction algorithm.

The pseudo-code of the topology correction process is illustrated in Figure 4.16. For an image consisting of N number of A-scans, an array of size N-1 containing Δz_n will be created. As shown in Eq.(4.7), $F(\Delta z)$ is a cross-correlation (XOR) function with variable Δz indicating the pixel-shift amount between A-line(n) and A-line(n+1), while $n \in [1, N-1]$. A-line(n) indicates the number n A-line out of the total N A-lines in the frame image. By iterating Δz from $-\Delta z_{range}$ to $+\Delta z_{range}$ with incremental step size of one, Δz_n will be recorded as the value that maximize $F(\Delta z)$. Δz_{range} determines the time cost to Δz_n. The larger it is , the longer it takes to find Δz_n. Here we chose Δz_{range} to be 20, which corresponds to a relative displacement of 32 μm, then considering the sampling rate of 460 A-scans per second, this corresponds to an axial motion speed of $\pm$14.72 mm/s between adjacent A-scans. This speed range is sufficient for us to correct the relative axial motion speed induced by hand tremor or target motion. Then, using the first A-line as the origin ($Z_1 = 0$), the total amount of pixel shift Z for A-line(m) is the summation from Δz_1 to Δz_{m-1},$m \in [2, N]$, shown in Eq.(4.8). By shifting A-line(m) with the corresponding Z_m in the axial direction for all the A-lines in the frame, the final topology correction image is achieved. The assumption for this method working properly is that adjacent A-scans of biological tissue exhibit maximum cross-correlation under a natural topology state, which is intuitive [112] and that they are correlated, which is satisfied by

experimentally oversampling the imaging area.

$$F(\Delta z) = XOR[A_n(z), A_{n+1}(z + \Delta z)], \Delta z \in [-\Delta z_{range}, +\Delta z_{range}], n \in [1, N-1] \tag{4.7}$$

$$Z_m = \sum_{i=1}^{m-1} \Delta z_i, m \in [2, N] \tag{4.8}$$

4.3.3 Results and Discussion

4.3.3.1 Motion compensation test

First, we tested the motion compensation function of our system using a hold-still task. The probe was held by one volunteer and pointed perpendicular to a target surface. The operator tried to maintain a constant distance of D = 640μm and the probe position was recorded as the function of time. As shown in Figure 4.17(a), our feedback control of the motor greatly reduced hand tremor, which is composed of both low frequency drift and high frequency vibration. The system was able to limit the hold-position drift/error to less than the maximum peak-to-peak error of $\pm 14\mu m$ as shown in Figure 4.17(b). The RMS error after motion compensation was much lower and was $\pm 3\mu m$. Figure 4.17(c) shows the frequency spectrum analysis results of the fiber tip-to-probe distance with (red) and without (blue) motion compensation over a 10-second period. As we can see from the spectrum, the hand tremor has been well suppressed.

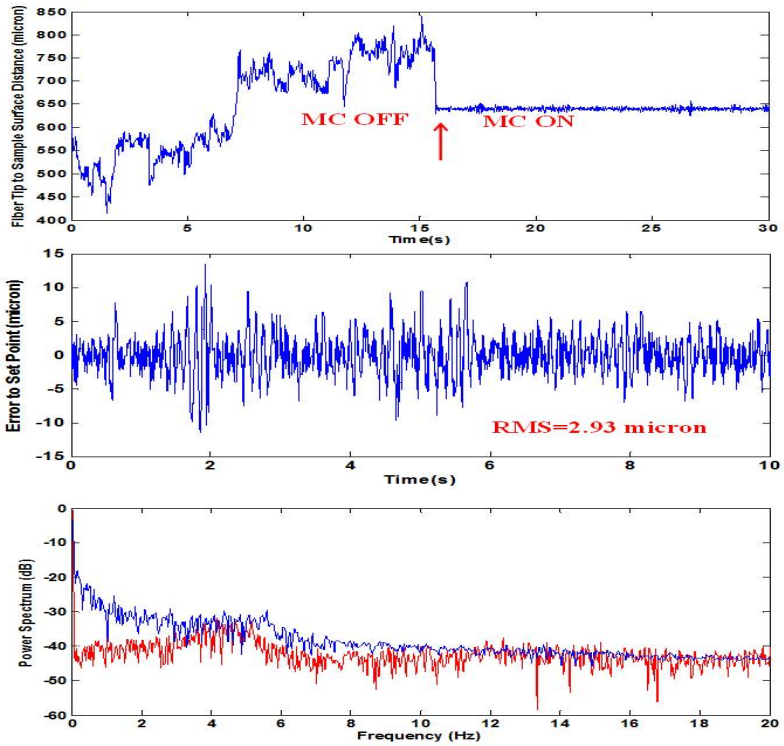

Figure 4.17: (a) Free hand-held probe position tracking; (b) zoomed view of motion compensation, time zero corresponding to the red arrow position in (a); (c) frequency analysis 0 to 20 Hz: red (motion compensation is on), blue (motion compensation is off).

4.3.3.2 Hand-held imaging

To demonstrate that the motion-compensated hand-held probe can significantly enhance the imaging quality of the free-hand scanning OCT system, we performed a series of imaging studies using two phantom samples, in-vivo tissues, and ex-vivo bovine retina. The images were cropped for better viewing. Figure 4.18(a) is a digital camera image of the first artificial sample , which is a resolution card with 1 line per

millimeter lines of the card surface. Figure 4.18(b) is the standard galvanometer-mirror scanned SD-OCT image along the red line mark in Figure 4.18(a), the lateral image field of view is 22 mm. From Figure 4.18(b) we can clearly see the structure of our sample. On top of the target card we placed two polymer tape layers and then we added five polymer strips separated from each other to form a step-like surface topology. Parallel to the red line mark in Figure 4.18(a), is a stainless steel rod used to guide the probe scanning, though it is very difficult to scan the exact same position during this study. Figure 4.18(c) is the handheld imaging without motion compensation. We can clearly see the hand tremor and thus two important consequences: sample collision and signal loss. Places where the probe collided with the sample were marked in red circles in the image. Figure 4.18(d) is the topology corrected image of the Figure 4.18(c). Figure 4.18(e) is the handheld imaging with motion compensation. As expected, there was no accidental collision with the sample and the probe tracked the area of interest precisely. Figure 4.18(f) is the topology corrected image of Figure 4.18(e). From Figure 4.18(d) and Figure 4.18(f), we can see that cross-correlation based shift correction algorithm can reconstruct the sample surface topology reasonably well. Therefore reconstructed images are much easier to interpret than those images with motion corruption artifacts. That is, the layer structure, detailed structure lied between layers, and the step shape surface structure are all clearly visible. Also, non-uniform lateral scanning speed can be visualized through the non-periodic structure of the underlying lines.

We further evaluated our system performance by imaging another phantom sample having a ridge shaped surface topology, created by placing layered tape on top of a clay. An image using a bulk scanning head is shown in Figure 4.19(a). Figure 4.19(b) shows a handheld imaging without the motion compensation. Since the height of the ridge is large, whenever the probe tip moved close to the ridge, it collided with the sample. The collision area is marked with a red rectangular box. When the probe collided with the surface the signal faded and the reconstructed image became incorrect over that range. Figure 4.19(d) is the handheld scanning image with the motion compensation. We were able to scan across the ridge without touching the ridges. Figure 4.19(e) is the topology corrected image of Figure 4.19(d). It is clear that the general ridge shape has been recovered with some error. Notably the flat bottom has been reconstructed into a curved shape. Nevertheless the shape of surface and the underying structure of the sample can be easily seen. Undoubtedly the software correction method we implemented here doesn't result in a perfect surface topology reconstruction. However, this technology provides an ability to scan OCT free-hand OCT with a needle probe, provides a large field of view and significantly reduces the chance of accidental tool tip collision with tissue.

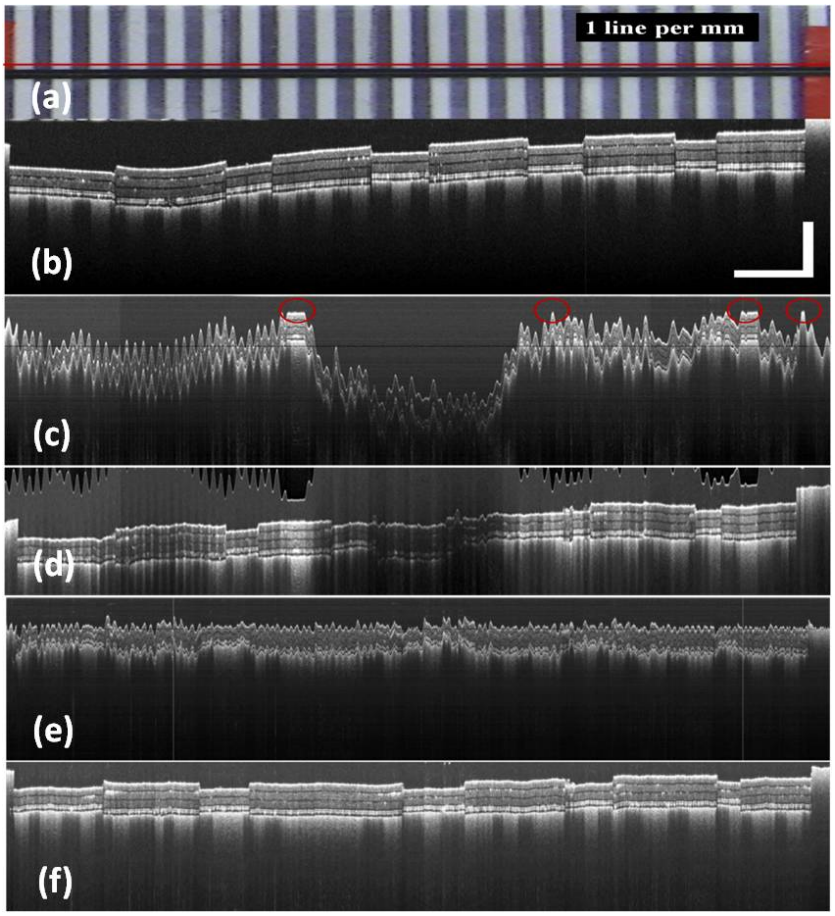

Figure 4.18: (a) camera picture of a phantom sample; (b) standard galvanometer-mirror scanned SD-OCT image of the phantom sample along the red line shown in (a); (c) freehand scanned image along the red line without motion compensation, red circles mark where the tool tip collided with the sample surface; (d) topology corrected image of (b); (e) freehand scanned image along the red line with motion compensation; (f) topology corrected image of (e). (scale bar: vertical 500 μm, lateral 2 mm).

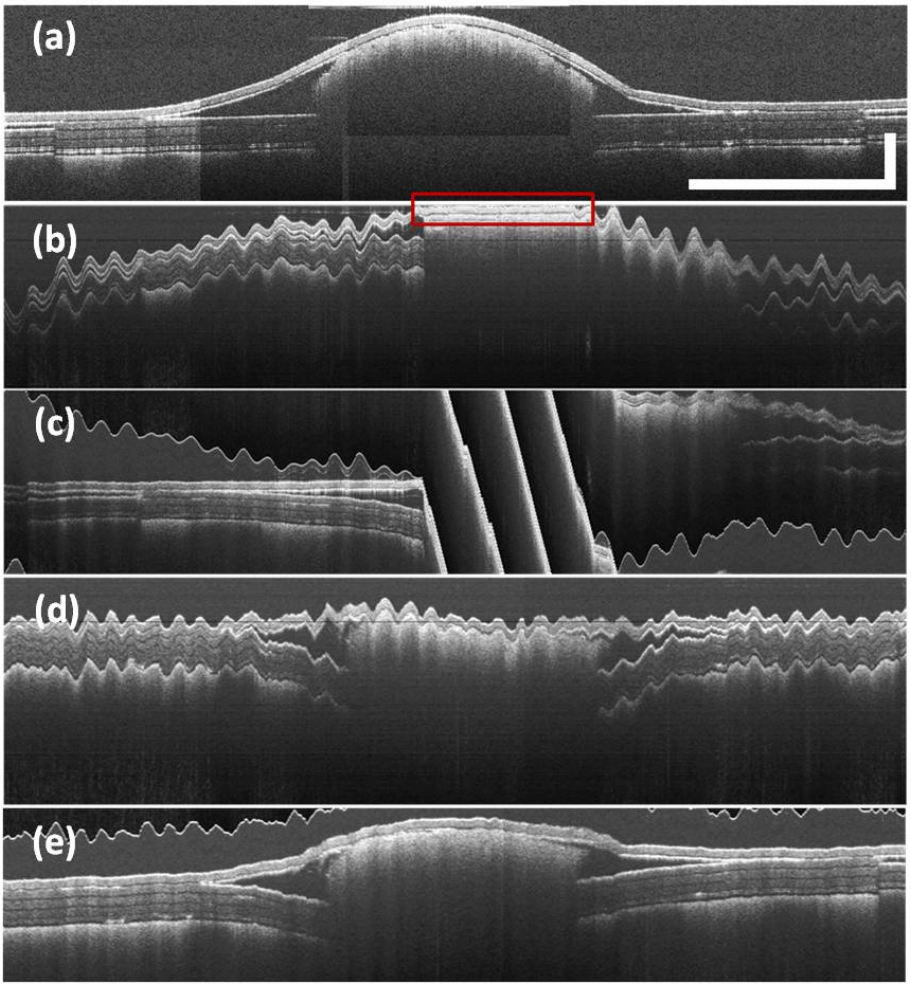

Figure 4.19: (a) galvanometer-mirror scanned SD-OCT image of a phantom with ridged surface topology (b) freehand imaging of the sample without motion compensation, red rectangular indicates where the probe collided with the sample surface; (c) topology corrected image of (b); (d) freehand imaging of the sample with motion compensation; (e) topology corrected image of (d). (scale bar: vertical 500 μm, lateral 2 mm).

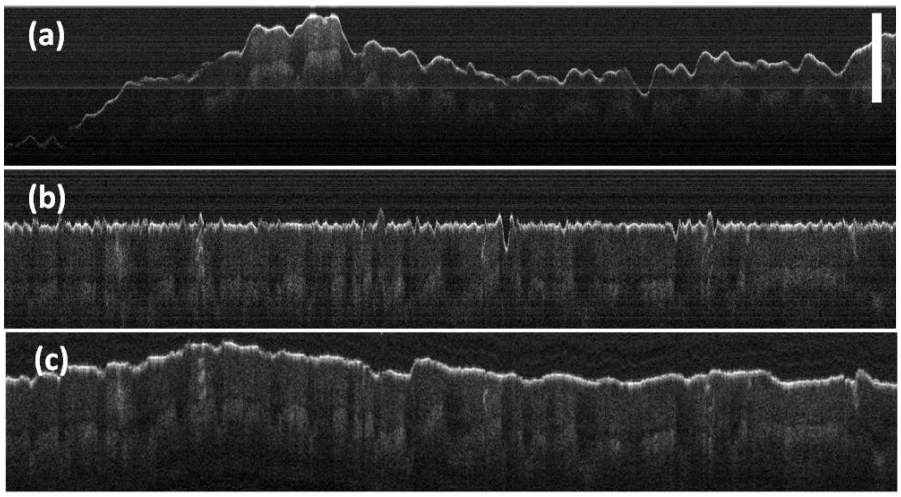

Figure 4.20: Hand-held imaging of human hand palm without (a) and with (b) motion compensation; (c) topology-corrected image for (b) (scale bar: 500 μm).

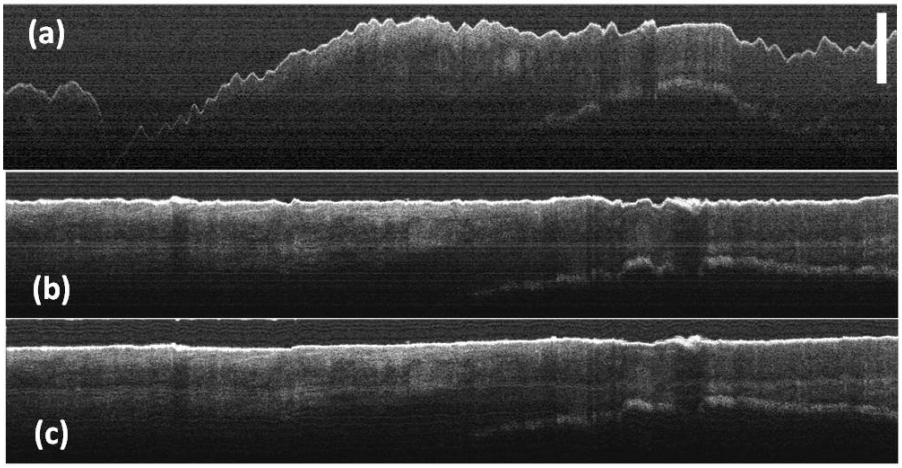

Figure 4.21: Hand-held scanning of human finger nail without (a) and with (b) motion compensation; (c) topology-corrected image for (b) (scale bar: 500 μm).

We further tested our system by imaging a non-stationary, naturally placed palm of the hand and finger nail; the results are shown in Figure 4.20 and Figure 4.21. Estimated lateral scanning range is 15 mm for Figure 4.20 and 8 mm for Figure 4.21. The hand tremor is apparent on images without motion compensation, Figure 4.20(a) and Figure 4.21(a). Accompanied with hand tremor was the non-uniform intensity variation over the scanned images. When the probe distance increases, A-lines become dimmer and sometimes get completely lost. One extreme case is shown in the left part of Figure 4.20(a) and Figure 4.21(a): the probe is so far away from the tip that detailed structure or anatomy information beneath the target surface was not imaged. The effect of motion compensation can clearly be seen from images in Figure 4.20(b) and Figure 4.21(b). The low frequency axial drift was almost completely negated while the amplitude of high frequency vibration was well compressed. Detailed structures of the hand palm and finger nail are clearly visible. We can clearly see the boundary between epidermises and dermises layers and sweat duct lying within the epidermises layer. Due to the wavy surface topology of hand palm, the probe compensates more when the hand palm was imaged compared to the finger nail. After surface topology correction,Figure 4.20(c) revealed the smooth wavy surface topology of hand palm clearly, and the sweat duct in Figure 4.20(c) becomes naturally spiral. Figure 4.21(c) also revealed smooth and natural topology of the finger nails junction area. These performances of our system were consistent with our phantom imaging. Safety is one of the main concerns for the image-guided intervention. By keeping our probe

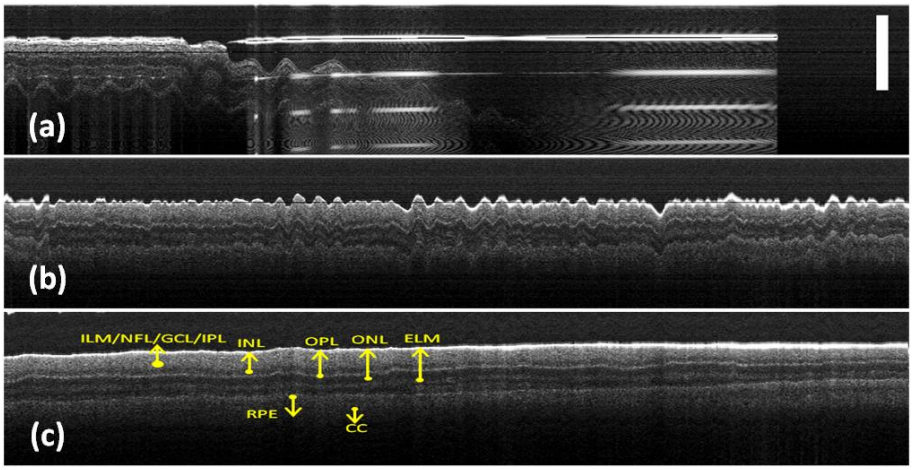

Figure 4.22: Hand-held scanning of bovine retina without (a) and with (b) motion compensation; (c) topology-corrected image for (b) (scale bar: 500 μm).

at a constant distance of 200 μm, risk of damaging the sample surface by accidental hand movement was avoidedan important factor which needs to be addressed during image-guided microsurgery intervention.

To further study the probe imaging capability, we performed ex-vivo bovine retina imaging with vitreous removed as shown in Figure 4.22. Estimated lateral imaging range was 6 mm. Cow eyes were obtained from a local butcher shop. Figure 4.22(a) is the image without motion compensation. The probe collision with the retina can be seen from the distorted image areas. Figure 4.22(b) is the image with motion compensation while Figure 4.22(c) is the topology corrected image of Figure 4.22(b). This again demonstrates the active distance controls ability to prevent collision between the sample and the probe. Since the eye was imaged several hours after harvesting, the retina degenerated and some retinal layers are less prominent. First four layers of the retina have lost boundaries. All retina layers have been labeled in Figure 4.22(c).

Performance of motion compensation is a crucial factor that affects the quality of free-hand scanning OCT systems. In our experiment, we used a piezoelectric motor controlled OCT probe to provide the motion compensation through a USB com port interface with baud rate of 9600 bits/s. Command delivery through USB cable consists of 19 bits: 8 of them are used to control the time cost of one motor step; 10 of them are used to control how many steps to move during one command, while 1 bit of them is the stop bit, which gave us the maximum compensation rate of around 505 Hz. During our experiment, the compensation rate varied from 450 Hz to 470 Hz. We confirmed the compensation rate by continuously sending commands to the motor and recording the time cost in C++ without any other computation task involved. The result was 500 Hz, which corresponds well with the 505-Hz limit. The command delivery latency through the USB port was one of the bottlenecks. Another important factor that affected the motion compensation result was our system distance sensitivity. It is easy to compensate for small errors, but this would require better distance sensitivity that would enable the system to detect these smaller errors. We applied a 10x zero-padding to the spectrum, which effectively improved the system distance sensitivity by a factor of 10: from 1.6 μm to 0.16 μm. However, such digital processing method cannot improve the system sensitivity indefinitely [107]. As the time-varying M-scan images were recorded, there was a non-uniform spatial sampling rate in lateral direction due to the non-constant scanning velocity of hand-held scanning. Though this is not the focus problem of this manuscriptand the resulting

images we got did not suffer a lot from this non-constant scanning speedthis needs to be addressed in the future. The motion-compensation process results in flat images, which eliminates the topographical information of the target surface; therefore we implemented a simple and intuitive cross-correlation maximization-based shift correction algorithm to restore the target topology. Further study on the topology correction algorithm such as Doppler velocity-based algorithms and registration algorithms based on different global objective functions [111] will be performed later. As both the lateral non-uniform scanning speed correction and topology correction utilize the cross-correlation information between adjacent A-scans, studies combining both axial and lateral scanning correction will be carried out in the future. Proper probe tip engineering [113, 114]is also need in the future.

Chapter 5

Atherosclerotic Plaque Detection Using Full-range SD-OCT

5.1 Introduction

Stroke is the fourth leading cause of death in the United States [115]. Randomized clinical trials have shown carotid endarterectomy (CEA) surgery to be superior to medical therapy alone for prevention of stroke [116, 117]. Approximately 100,000 CEA procedures are now performed in the United States each year1, and perioperative stroke occurs in 3 to 6 % of cases [116–119]. While many perioperative strokes are unavoidable, the majority are due to technical errors, including residual plaque, suture lines or intimal flap, which may be prevented if diagnosed during the operation [119, 120]. Current intraoperative carotid imaging is limited to duplex

ultrasonography, continuous wave Doppler, or intraoperative angiography. Duplex ultrasonography is limited by low-definition imaging that often requires a trained ultrasonography technologist to interpret the intraoperative imaging. Continuous wave Doppler is easy to use and provides an overview of the patency of the reconstructed vessel through audible evaluation, but it is not able to provide imaging or quantify the degree of vessel stenosis [121] Intraoperative angiography is the gold standard for imaging but has the disadvantage of requiring the use of arterial puncture and bringing in a separate angiography team into the operating room [122]. A real-time, detailed imaging methodology for intraoperative assessment of CEA and cerebrovascular surgery is needed.

Optical coherence tomography (OCT) may offer a solution. OCT utilizes reflected infrared light, similar to the reflected sound waves found in ultrasound, in order to acquire real-time, cross-sectional imaging [4]. The benefit of OCT is that it provides resolutions of 5-10 μm compared with the resolution of several hundred micrometers found with ultrasound. Endovascular OCT imaging of vascular plaques has been shown to resolve the thin fibrous caps thought to be responsible for plaque vulnerability in addition to the ability to differentiate between lipid, calcium, and fibrous tissue [123] Endovascular OCT, however, involves imaging with a percutaneous arterial catheter. In order to obtain adequate vascular wall visualization in vivo, blood must be displaced with saline. Optimal imaging, therefore, is limited to 2 seconds without balloon occlusion of the vessel being imaged. This requirement limits the

practical application of endovascular OCT during open CEA surgery.

The apolipoprotein E deficient ($ApoE^{-/-}$) murine model has been established as one of the closest representations of clinical atherosclerosis in humans, modeling such aspects as plaque rupture in a similar pattern as the human pathology [124] $ApoE^{-/-}$ mice fed a high-fat diet (HFD) have been shown to consistently develop arterial plaques throughout the arterial system [125] Pravastatin therapy in combination with the model has been shown to reduce brachiocephalic artery plaque cross-sectional area by 61 % and the incidence of acute plaque rupture by 36 % [124].

We set out to develop an extravascular OCT imaging device for non-invasive, real-time, detailed atherosclerotic plaque visualization during CEA and intracranial vascular surgery. After development of the OCT imaging device, its accuracy in analyzing the presence of arterial plaques was assessed in the $ApoE^{-/-}$ model. Mice were randomized to wild-type mice on a regular diet, $ApoE^{-/-}$ mice on a HFD to promote plaque development, and $ApoE^{-/-}$ mice on a HFD with pravastatin therapy to inhibit plaque development and acute plaque rupture. To our knowledge, this is both the first publication of in vivo extravascular OCT imaging of carotid plaque morphology and the first application of OCT imaging to assess statin efficacy in a live, in vivo model of atherosclerosis.

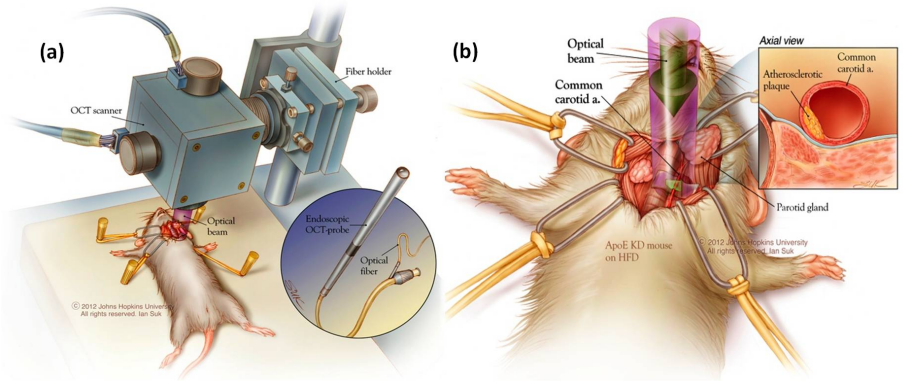

Figure 5.1: (a) Schematic of experimental setup. (b) Details of OCT cross-sectional imaging of the mouse left common carotid artery bifurcation.

5.2 Material and Methods

5.2.1 Experimental Design

We set out to assess the ability of intraoperative OCT imaging to accurately determine the presence, size, and morphology of carotid arterial plaques in a murine model of atherosclerosis. A total of thirty-nine wild-type and ApoE$^{-/-}$ mice in two separate experiments were placed into one of three groups to compare plaque development and morphology. Wild-type mice (n=13) were provided a standard rodent diet. ApoE$^{-/-}$ (n=26) were provided a high-fat diet (HFD) and then randomized to one of two treatment groups: 1) ApoE$^{-/-}$ on HFD and 2) ApoE$^{-/-}$ on HFD with daily pravastatin.

Study 1 consisted of a proof of concept analysis to establish the OCT imaging methodology, analyze plaque development over time in order to establish the optimal timing of carotid plaque development, and determine the survivability of the surgical

procedure. In the first experiment OCT imaging was obtained at 8 weeks (n=1 per group), 10 weeks (n=1 per group), and 14 weeks (n=3 per group). After left lateral neck dissection and OCT imaging were completed, the mice were either kept alive for a second imaging or were euthanized and perfused. After perfusion, the carotid arteries were again imaged in situ for comparison of plaque morphology with the live, *in vivo* images. A final feasibility experiment was then performed by converting the table-top, stationary OCT unit (Figure 5.1) into a handheld imaging probe adapted for clinical application (Figure 5.1inset). Mice at 10 weeks were imaged using the handheld probe prior to perfusion.

Study 2 was performed to establish the efficacy of OCT imaging to determine plaque presence and size compared with histology and to determine the treatment efficacy of pravastatin therapy. Mice (n=8 per group) were administered their designated treatments for 14 weeks followed by live, *in vivo* OCT imaging and post-perfusion in situ OCT imaging. The carotid arteries were then resected, and the histology obtained was compared with the OCT images. Acquired cross-sectional OCT images and histology slices were evaluated for percent lumen patency by highlighting the region of patent inner vessel lumen excluding plaque and calculating the highlighted area using ImageJ software (Rasband, W.S., ImageJ, U. S. National Institutes of Health, Bethesda, Maryland, USA, http://imagej.nih.gov/ij/, 1997-2012). The percent lumen patency was reported as mean ± standard error of the mean (SEM).

5.2.2 Animals

C57Bl/6J wild-type mice (Jackson Laboratories, Bar Harbor, Maine) and C57Bl/6J ApoE$^{-/-}$ (Jackson Laboratories, Bar Harbor, Maine) of age 10 weeks for the initial experiment and 18 weeks for the final experiment. All mice were housed in standard animal facilities with free access to Baltimore City water. Wild-type mice were given free access to standard rodent chow. ApoE$^{-/-}$ mice were given free access to high-fat, atherogenic rodent diet (Harlan Laboratories, Indianapolis, Indiana). The Johns Hopkins Animal Care and Use Committee approved all experimental protocols.

5.2.3 Design of the OCTimaging Device

Details of the OCT system configuration were reported in our previous work [21, 28,126]. The OCT system is built on a dual graphics processing unit (GPU) computer architecture, which allows for cross-sectional imaging with simultaneous ultra-fast 4D (3 spatial dimensions with time) reconstruction. The OCT spectrometer was set to operate at 1024-pixel mode by selecting the area-of-interest (AOI). The minimum line period was spectrometer-limited to 7.8 μs with the exposure time of 6.5 μs, corresponding to a maximum line rate of 128k A-scan/s. The imaging volume is 2.3 mm (X) by 2.3 mm (Y) lateral and 3 mm (Z) axial. Each B-mode image consisted of 512 A-lines. The system has a measured axial resolution of 6 μm in air and lateral resolution was approximately 20 μm assuming Gaussian beam profile.

5.2.4 Anesthesia

Mice were anesthetized with a single intraperitoneal injection (0.05mL/10g) of an anesthetic mixture containing xylazine (10mg/kg) (100mg/mL Xyla-ject; Phoenix Pharmaceutical, Inc., St. Joseph, MO) and ketamine (50mg/kg) (100mg/mL KetaThesia; Butler Animal Health Supply, Dublin, OH). Absence of pedal and tail pinch reflexes was confirmed prior to procedure performance.

5.2.5 Surgical Technique

After initiation of anesthesia, the midline and left neck were shaved (Chromini Cordless Trimmer, Wahl Manufacturing Co., Toronto, Canada). The region was then scrubbed with povidone-iodine topical antiseptic followed by 70 % ethyl alcohol. Mice were placed supine and a vertical skin incision was made in the skin overlying the left neck approximating the location of the left carotid sheath. The underlying soft tissue and salivary glands were dissected with the use of a surgical microscope (Carl Zeiss Co., Oberkochen, Germany). Four miniaturized retractors were placed to retract the submaxillary gland, sternocleidomastoid muscle, and midline strap muscles to reveal the region of the carotid sheath. The left common carotid artery was bluntly separated from the surrounding tissue and was visualized to above the level of the carotid bifurcation. A small piece of latex measuring 3mm x 5mm was then placed under the distal common carotid and proximal bifurcation to maintain visualization

during the imaging process and to mimic similar surgical technique used in CEA.

After *in vivo* OCT imaging of the live mice was completed, the mice were separated into those who were to remain alive for a follow-up imaging procedure (n=3 per group) and the remaining underwent perfusion in order to undergo post-perfusion imaging. Mice designated to remain alive for additional imaging had the latex piece removed, tissues re-approximated, and the incision closed using a 4-0 silk suture (Ethicon, Sommerville, New Jersey).

5.2.6 OCT Imaging Acquisition and Analysis

After left carotid exposure, the extravascular OCT scanner was placed over the distal common carotid in order to capture plaque development at the carotid bifurcation. There were two imaging modes of the OCT system: B-mode and C-mode imaging. The OCT system ran at 128,000 A-scans per second. Under B-mode imaging mode, cross-sectional image of a specific area of interest under investigation by the surgeon was obtained. Each raw B-mode image consisted of 512 A-scans covering a reasonable whole vessel diameter. Every 10 frames were averaged to improve the image quality, which gives an effective imaging video rate of 25 frames per second (fps), from an initial rate of 250 fps. Another advantage of averaging the frames is that speckle patterns, which are inherent with OCT images, are averaged out for blood flow whereas plaque and vessel wall images contained a pronounced grain pattern. This information was used to determine which part was plaque and which part

was blood within the vessel wall. For C-mode imaging, each volume consisted of 500 B-frames. While real-time images were rendered, raw spectra data for the B-mode and C-mode images were also saved for later analysis, if needed. Image processing software, ImageJ, was used to perform the post-image processing and volume rendering.

5.2.7 Tissue Preparation

After completion of OCT imaging, mice were perfused via bilateral thoracotomy, cannulation of the left ventricle, and opening of the right atrium. Perfusion was performed with 50mL of normal saline (0.9% NaCl) at 10mL/min using a pump (Watson-Marlow, Inc., Wilmington, MA). The saline was followed by perfusion with 50mL of 10% formalin at 10mL/min. Injection of porcine gelatin (Sigma Aldrich, St. Louis, Missouri) was then performed via syringe injection through the previously placed cannula within the left ventricle. The mice then underwent in situ, extravascular OCT imaging for comparison with the previous live, in vivo imaging.

After completion of the *in situ* imaging, the carotid artery was excised from the level 10mm proximal to the common carotid bifurcation to the level 1mm distal to the bifurcation. A 4-0 silk suture tie was placed at the proximal end for identification during histologic slicing. The excised carotid arteries were labeled and placed in 10% formalin for $>$ 48hours for fixation and embedded in paraffin. Five axial sections of 10 μm thickness were taken at the carotid bifurcation at 5 levels separated by 100 μm.

Samples were then processed and placed on glass slides. One slide from each level was then stained with hematoxylin and eosin (H&E). The level found to be nearest the midpoint of the carotid bifurcation was then independently identified and used for comparison analysis with OCT imaging.

5.2.8 Inter-rater Reliability

In order to better determine the potential clinical application of intraoperative OCT imaging of carotid plaques, a brief quiz was designed to assess the ease of identifying plaque on single-frame, cross-sectional images obtained from live mice. A one-page instruction sheet consisting of four cross-sectional images, two containing no plaque and two containing carotid plaque with the plaque identified by outline and arrows, was initially provided to the volunteers. After this brief instruction page, four blinded volunteers were asked to identify whether plaque was present in a series of 24 printed OCT images obtained in vivo from live study mice. The volunteers had varying levels of experience with interpreting OCT images from no exposure to experienced.

5.2.9 Statistical Analysis

Analysis of percent lumen patency between treatment groups using a single imaging modality (live, *in vivo* OCT imaging; post-perfusion OCT imaging, histologic

imaging) was performed using a Kruskal-Wallis test (one-way, nonparametric ANOVA). Statistical significance of the difference in percent lumen patency between imaging modalities was calculated using the Friedman test (non-parametric, repeated measures ANOVA). Inter-rater reliability was calculated as mean SEM sensitivity and specificity. All calculations were performed using GraphPad Prism version 6.00 for Macintosh (GraphPad Software, La Jolla California USA).

5.3 Results

5.3.1 OCT Image Acquirement

OCT imaging was acquired in a total of 38 wild-type and ApoE$^{-/-}$ mice. Study 1 consisted of a total of 15 mice within the 3 treatment groups imaged over time for proof of concept and determination of study methodology: Group 1) wild-type mice provided a standard rodent diet (n=5); Group 2) ApoE$^{-/-}$ mice provided a HFD (n=5), and Group 3) ApoE$^{-/-}$ mice on HFD with daily pravastatin (n=5). Mice from each group were imaged at 8, 10, and 14 weeks to establish the time-course of plaque development in the ApoE$^{-/-}$ mouse carotid. Plaque was initially evident at 8 weeks within the ApoE$^{-/-}$ on HFD mice. Optimal plaque development across all imaged ApoE$^{-/-}$ on HFD mice was seen at 14 weeks. ApoE$^{-/-}$ mice on HFD given daily pravastatin at the time of initiation of the HFD had a lesser degree of plaque development. The OCT scanning fiber was then integrated into a handheld probe as

a proof of concept of the convertibility of the imaging system into a clinically feasible handheld device for intraoperative imaging.

Study 2 was then performed to establish the statistical efficacy of extravascular OCT detection of carotid atherosclerosis compared with histology and to establish the therapeutic efficacy of pravastatin treatment. After administration of the designated treatment for 14 weeks, mice were anesthetized and surgical exposure performed for in vivo OCT imaging, post-perfusion in situ OCT imaging. The carotid arteries were then resected and the previously obtained OCT images were compared with the histology.

5.3.2 Atherosclerotic plaque evaluation

At 14 weeks after treatment initiation, the 23 (one ApoE$^{-/-}$ mouse on HFD did not survive to 14 weeks) mice of study 2 underwent live, in vivo OCT imaging, post-perfusion *in situ* OCT imaging, and *ex vivo* histologic analysis (Figure 5.3and Figure 5.2). When placed in direct comparison with the perfused arteries, the scattering component of RBCs results in suboptimal imaging of the far wall of the carotid artery. Despite this limitation, the presence of carotid plaque was identified during OCT imaging in 100% of ApoE$^{-/-}$ on HFD mice prior to perfusion. When compared with histology, OCT imaging prior to perfusion revealed 100% sensitivity and 100% specificity for plaque identification in both the ApoE$^{-/-}$ on HFD group and the ApoE$^{-/-}$ on HFD with pravastatin group.

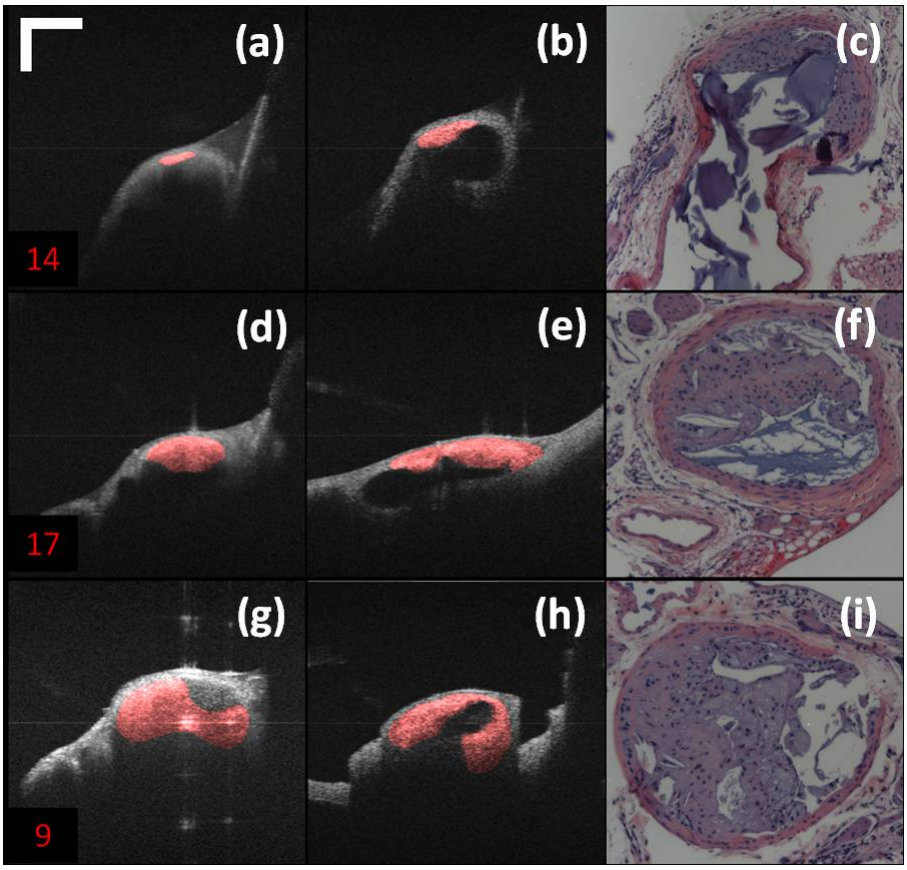

Figure 5.2: Carotid artery vessel lumen patency at various levels within the Apolipoprotein E deficient mouse on high-fat diet, mouse label number was marked on the bottom left. Level 1(bottom row):100-80% lumen patency; Level 2(middle row):80-50% lumen patency.Level 3(top row):50-0% patency. (scale bar 500μm, plaques are marked in red.) The violet artifact within the lumen of the H&E slides is a result of porcine gelatin injection after artery perfusion in order to maintain the 3D architecture for comparison of vessel lumen patency with the obtained OCT images.

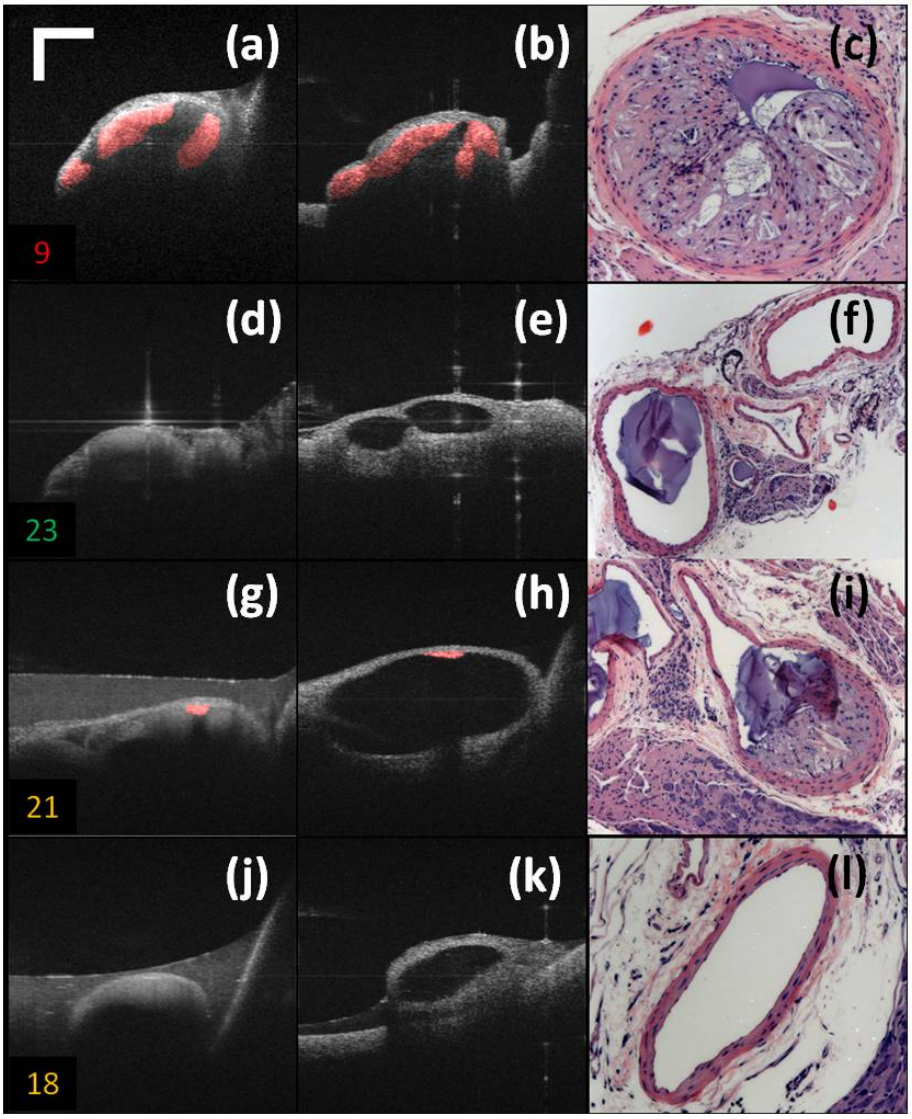

Figure 5.3: Mouse number is labeled in color at the bottom left of each row: green indicates wild-type mice on regular diet, red indicates Apolipoprotein E deficient ($ApoE^{-/-}$) mice on high fat diet (HFD), and yellow indicates $ApoE^{-/-}$ mice on HFD with pravastatin treatment. The left column is images obtained during live, *in vivo* imaging. Atherosclerotic plaque is highlighted in red. The second column is in situ images after perfusion. The right column consists of hematoxylin and eosin (H&E) histologic slides, stained after perfusion (scale bar 500 μm). The violet artifact within the lumen of the H&E slides is a result of porcine gelatin injection after artery perfusion in order to maintain the 3D architecture for comparison of vessel lumen patency with the obtained OCT images.

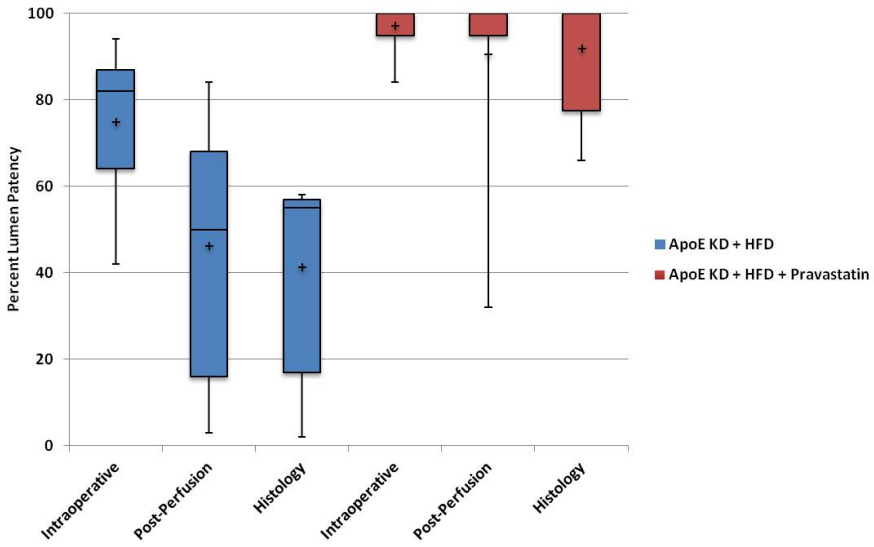

Figure 5.4: Percent lumen patency of the murine carotid artery, as calculated by live, intraoperative OCT imaging; post-perfusion OCT imaging; and histology. The area of patent vessel lumen is presented for each mouse within the apolipoprotein E knock-down (ApoE KD) on high fat diet (HFD) group and the ApoE KD on HFD with pravastatin treatment group. Box plot symbols are as follows: plus, mean; minus, median.

The mean percent lumen patency (Figure 5.4) in ApoE$^{-/-}$ on HFD mice was found to be 74.9% (±6.8), significantly less than normal mice ($p<0.001$) in which all were found to have 100% lumen patency and ApoE$^{-/-}$ on HFD with pravastatin ($p<0.01$), which were identified to have 97.1% (±5.8) lumen patency. In comparison with post resection histology, mean percent luminal patency in ApoE$^{-/-}$ on HFD mice was found to be significantly less during in vivo imaging than on post resection histology ($p<0.01$). ApoE$^{-/-}$ mice on HFD revealed a 74.9% (±6.8) lumen patency in comparison with a 41.4% (±8.6) lumen patency noted on histology. With normal mice and ApoE$^{-/-}$ on HFD with pravastatin, no significant difference was noted between live, in vivo OCT imaging and post-perfusion histology.

5.3.3 Inter-rater Reliability of Plaque Presence

After completion of the standardized volunteer assessment of single cross-sectional images, the mean sensitivity of live, *in vivo* OCT imaging in identifying plaque presence was 86.25% (±8.25) and specificity was 71.50% (±9.17).

5.3.4 En face and 4D reconstruction

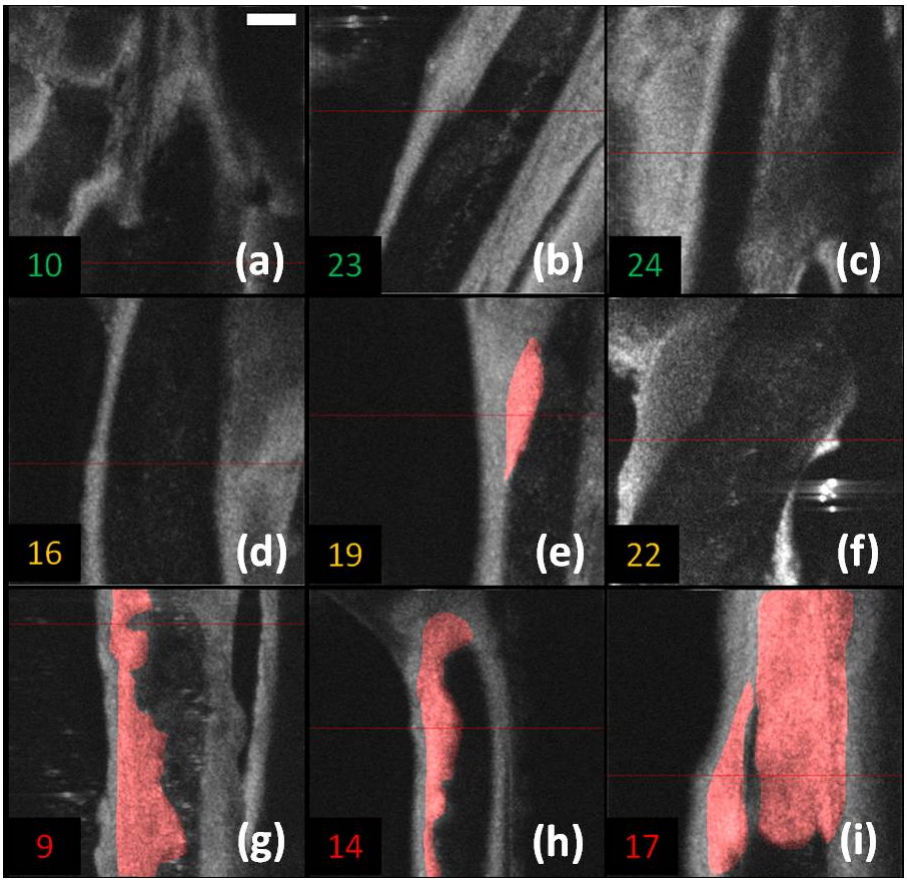

Figure 5.5: *En-face* slices (screen captured with red line indicating OCT scanning beam) at different depths to visualize the carotid plaque from different mice after perfusion, mouse label number was marked in color at the bottom left, green indicates wild-type mice on regular diet, yellow indicates Apolipoprotein deficient ($ApoE^{-/-}$) mice on high-fat diet (HFD with pravastatin treatment, and red indicates $ApoE^{-/-}$ mice on HFD without treatment (scale bar for both horizontal and vertical directions: 500 μm, plaques are highlighted in red).

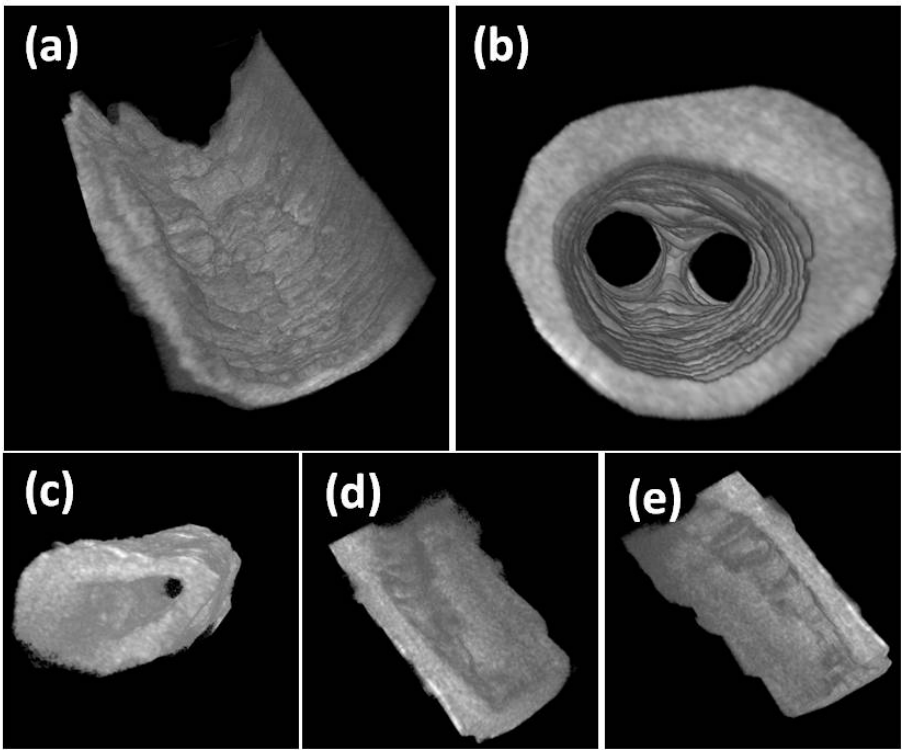

Figure 5.6: 4D volume rendering of the vessels: (a) an in-vivo partially occluded vessel ; (b) a normal hollow vessel after perfusion; (c) a heavily occluded vessel after perfusion; (d) top half of vessel (c) through virtual cut;(e) bottom half of vessel (c) through virtual cut.

In order to further assess the clinical potential of intraoperative OCT imaging, our OCT system was engineered to provide simultaneous volume rendering of the scanned images in order to present the plaque morphology and optimize the ability to determine the extent of atherosclerotic plaque within a vessel. From a 4D volume C-scan image, en face slices at varying depths were obtained to visualize plaque during the live, in vivo imaging and the post-perfusion in situ imaging (Figure 5.5). Figure 5.6(a) reveals live, in vivo vessel imaging with partial atherosclerotic plaque occlusion. Figure 5.6(b), depicts a normal vessel wall after perfusion, and reveals

a virtually simultaneous reconstruction of the common carotid bifurcation into the internal and external carotid arteries. Figure 5.6(c) shows a heavily occluded vessel after perfusion. To better study the inner plaque volumetric morphology, two virtual cut views can be made by cutting the vessel into top, Figure 5.6(d) and bottom, Figure 5.6(e), halves.

5.4 Discussion

We present the first statistical analysis of the ability of extravascular OCT imaging to evaluate the presence and morphology of carotid plaque in ApoE$^{-/-}$ mice and the first use of extravascular OCT to analyze pravastatin efficacy in preventing plaque development in live mice. Presence of atherosclerotic carotid plaque was positively identified by OCT imaging in 100% of ApoE$^{-/-}$ mice on HFD. Upon analysis of plaque morphology, live, in vivo OCT imaging in ApoE$^{-/-}$ mice on HFD had a statistically significant decrease in vessel lumen patency compared with wild-type mice. Pravastatin therapy was found to significantly increase the carotid artery lumen patency in ApoE$^{-/-}$ mice on HFD. This statistically significant increase in vessel lumen patency was evident on live, *in vivo* OCT imaging and confirmed by post-perfusion *in vitro* OCT imaging and histology.

A standardized assessment containing 24 randomized OCT images of live, in vivo carotids from all three treatment groups was then presented to a group of volunteers

with a diversity of experience with OCT images from zero to experienced. Although presented with a single cross-sectional carotid image rather than a dynamic, live video with 4D reconstruction, which would be available during live imaging, the assessment revealed a mean sensitivity of 86.3% and specificity of 71.5%. Given the presence of the added limitation of erythrocyte scattering seen with in vivo OCT imaging, this sensitivity compares favorably with that of the ex vivo, perfused analysis of human coronary plaque by intravascular OCT by Rieber et al. which revealed a sensitivity ranging from 64-77% and specificity of 88-97%16. Likewise, Manfrini et al. reported a sensitivity of 45-83% and specificity of 76-83%17 for clinical intravascular OCT imaging. In comparison, our OCT imaging during study 2 revealed 100% sensitivity and specificity for carotid plaque detection when live, *in vivo* imaging was compared with post-perfusion histology.

Our purpose in this study was to establish whether OCT imaging would provide an effective technique for high-definition, live imaging that would assist intraoperative decision-making during CEA and other open cerebrovascular surgeries. Recent research interest has focused on the ability of endovascular OCT imaging of atherosclerotic plaques to provide information on plaque morphology and possibly assist in predicting plaque rupture vulnerability [127, 128]. While endovascular OCT imaging may have diagnostic potential, its intraoperative application is limited. Its requirement for invasive, intravascular catheter placement requires the equipment and expertise of a physician experienced in endovascular techniques, adding to the

time and cost of a potential surgical procedure. In addition, standard CEA surgical technique requires the use of intraoperative temporary arterial clipping, precluding the simultaneous use of endovascular catheter [129]. Likewise, endovascular OCT imaging would be a suboptimal imaging modality within the field of cerebrovascular neurosurgery where temporary clipping is often used during aneurysm and cerebral revascularization [130] surgeries, both potential applications for extravascular OCT imaging technology in assessing vessel lumen patency and flow dynamics.

The greatest benefit to date of OCT image acquisition over intraoperative ultrasound is the high-definition possible that enables detailed 4D (3 spatial dimensions plus time) reconstruction of the vessel lumen. With the dual-GPU system engineered for our present device, we were able to produce virtual-live 4D images that could be used to make instantaneous intraoperative decisions without need for an invasive procedure, such as intravascular catheter insertion. In addition, many OCT imaging devices have been limited by a frame capture rate of 4 to 8 frames per second (fps) found in initial studies [123, 131] with up to 100fps on current commercial units [132]. Our dual-GPU system captures 250fps and averages every 10 frames. Speckle patterns, which are inherent with OCT images, are averaged out as blood flow whereas plaque and vessel wall images remain stable. The averaging, therefore, removes much of the motion artifact found in a live pulsating object, such as the mouse carotid artery, enabling clearer visualization of the plaque morphology. In addition, the ability of this system to be integrated into a handheld imaging probe allows for free-range

imaging of the vessel lumen from multiple angles.

The most apparent limitation of OCT imaging is the depth of light penetration, between 0.5 and 3mm with most systems used clinically today. Depth of light penetration is directly related to the wavelength selected and becomes a trade-off between light absorption and scattering. Absorption is minimized within tissue between the wavelengths of 700 to 1300nm. While absorption is lower at 800nm, scattering is less at 1300nm, which leads to greater tissue penetration at longer wavelengths. For our system, we utilized a light source of wavelength 825nm, as we found this to provide the optimal balance of light absorption and tissue penetration for imaging murine carotid atherosclerosis. This choice of wavelength, however did limit our depth of penetration to approximately 1-2mm. One potential method of overcoming this limitation is through the use of the prototype handheld OCT imaging probe. Holding the probe from three different angles at 0°, 90°, and 180°, for example, could provide for a virtual 360° image reconstruction of the vessel lumen. Also, depth of tissue penetration is less of an issue within the field of microvascular neurosurgery, such as aneurysm securing procedures, where the integration of our current system into a handheld imaging probe may have immediate clinical application. For example, arguably some of the most complex of cerebral aneurysms to secure with an open surgical approach involve the anterior communicating artery (ACoA). The average diameter of human ACoAs is 1.5mm, which is within the 1-2mm depth of penetration using our current OCT imaging system [133]. An OCT imaging probe would allow for evaluation of the

vessel lumen after aneurysm securing, immediately ensuring that no nearby perforating arteries are unknowingly occluded by the aneurysm clip. Intraoperative occlusion of small perforating vessels has been estimated to account for 8% of all strokes after clipping of ruptured cerebral aneurysms [134]

5.5 Summary

OCT evaluation of the carotid artery in ApoE$^{-/-}$ mice on HFD revealed a statistically significant decrease in lumen patency compared to wild-type mice on a regular diet. Pravastatin was found to significantly increase vessel lumen patency in the ApoE$^{-/-}$ mouse on HFD. OCT offers the potential for real-time, detailed vessel lumen evaluation with simultaneous 4D reconstruction, potentially improving surgical accuracy and outcomes during CEA and cerebrovascular neurosurgical procedures.

Chapter 6

Microvascular Anastomosis Guidance and Evaluation Using Real-time 3D Doppler SD-OCT

6.1 Introduction

Vascular and microvascular anastomosis is considered to be the foundation of plastic and reconstructive surgery. In 1912 Alexis Carrel was awarded the Nobel Prize for describing a suture technique utilizing precise placement of sutures to connect the two ends of vessels together [135]. This procedure has since remained a challenge for surgeons to master for nearly 100 years [136]. Even in the era of high quality, binocular surgical microscopes equipped with optics providing highly magnified images, this

technique still requires the highest level of skill and surgical expertiseespecially for small vessels (diameter less than 1.0 mm). Advancements in microvascular surgery have revolutionized the approach to reconstructive microsurgery [137]. In the last two decades, innovative techniques such as vascular coupling devices [138], thermo-reversible poloxamers [136], and suture-less cuff techniques that can provide rapid vascular anastomosis [139] have been introduced.

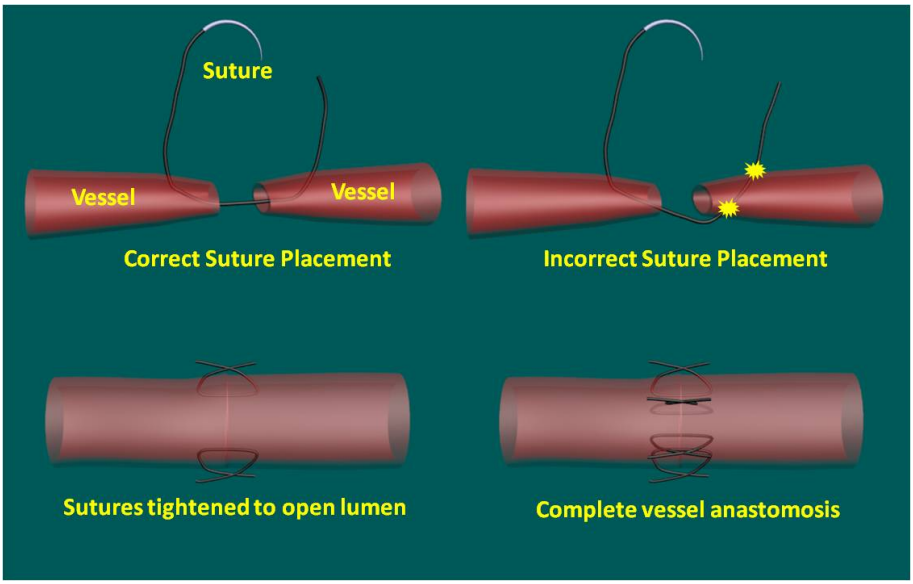

Figure 6.1: Suture based vascular anastomosis

Figure 6.1 illustrates the procedure of suture based vascular anastomosis. First(top-left), sutures are placed in collapsed vessel from adventitia through intima on one end, followed by suture placement from intima to adventitia on the other vessel end. Then(bottom-left), sutures are laid down flat and tightened, which approximates the intima, while the lumen is opened to allow placement of sutures. Finally(bottom-right), sutures are applied circumferentially for the anastomosis, making a complete

seal to prevent leakage. Top-right of Figure 6.1 illustrates an incorrect suture placement that needs to be avoided during surgical operation.

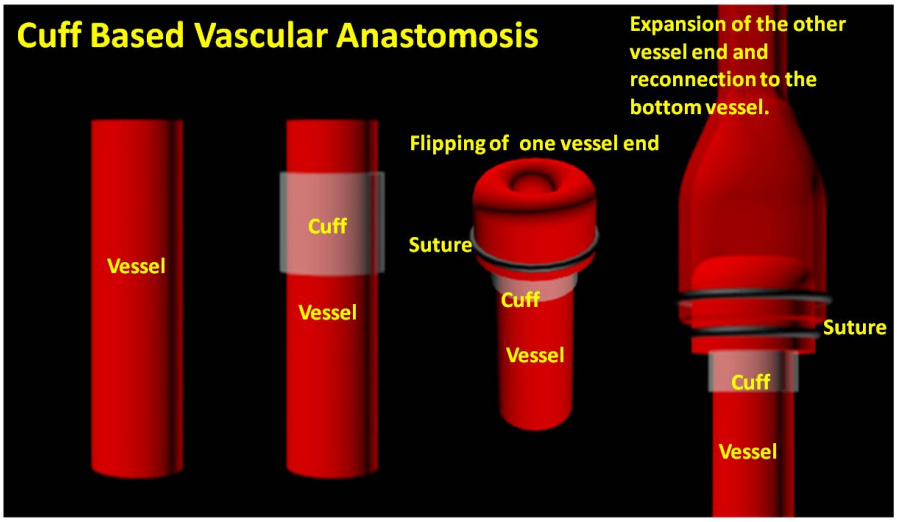

Figure 6.2: Cuff based vascular anastomosis

Figure 6.2 illustrates the procedure of suture-less cuff based vascular anastomosis. First,a biocompatible cuff with proper diameter is chose to be placed outside of one vessel. One vessel end was flipped over and tied to the cuff using sutures. After the other vessel end is expanded to be grafted to the flipped vessel end. A second suture tie is made to attach the top vessel onto the cuff.

However, no notable innovations in the field of surgical imaging have been developed that can provide real-time in-depth view, 3D guidance, and postoperative evaluation for microvascular surgery. Computed tomography (CT) angiograms, magnetic resonance (MR) angiograms, and ultrasound Doppler are three main postoperative diagnostic imaging modalities that surgeons resort to for vascular anastomosis [136]. When it comes to microvascular surgery for vessel diameter less than 1 mm and su-

per microsurgery for vessel diameter less than 0.5 mm, however, drawbacks of these imaging modalitieslow spatial resolution, slow imaging speed, poor temporal resolutioninhibit their application [140]. Attaching an implantable Doppler probe to the anastomosis site is a non-imaging method to detect thrombosis by listening to the flowing sound in the vessel. Although it can tell whether the flow continues, it cannot provide the surgeon with further thrombosis morphology detail [141]. None of the above-mentioned methods is capable of performing real-time surgical guidance or assistance.

Optical coherence tomography (OCT) is a well-established, non-invasive optical imaging technology that can provide high-speed, high-resolution, 3D images of biological samples [1]. Pioneer work by Boppart and colleagues in 1998 used OCT to perform intraoperative assessment of microsurgery [6]. In this work, the 3D OCT reconstructions depicted the structure within an arterial anastomosis and helped identify sites of lumen obstruction [6]. Since then OCT has evolved from a time-domain system to the much faster Fourier domain system. Functional OCT such as phase-resolved Doppler OCT (PRDOCT) developed two decades ago has enabled high-resolution tissue structure and blood flow imaging [42]. Furthermore, ultra-high speed OCT data processing and image rendering based on graphics processing units enabled real-time 4D OCT imaging [17,28,29]. Previously, our pilot study with real-time 3D OCT video intra-operative guidance [126] was aimed at enabling depth perception, facilitating micro-surgical education and improving surgical outcome through prompt diagnosis of

potential intra-operative complications. Only one suture tie was made in that study. In this study real-time PRDOCT with simultaneous 3D structure and flow imaging was introduced to microvascular anastomosis for mainly two purposes: intraoperative assistance to surgeons in avoiding detrimental technical errors and post-operative evaluation of surgical outcome in terms of detecting the flow status, lumen patency, and thrombus formation in the anastomosed vessels. Compared to previous video volume rate imaging speed (10 volumes per second), we reduced the speed to 0.27 volumes per second with increased image lateral resolution to better serve the need for accurate guidance of the suture. This imaging speed was also fast enough not to hinder the surgeon's operation. We demonstrated the PRDOCT-assisted whole microvascular anastomosis procedure and postoperative evaluation case by case in a rodent model.

6.2 Methods

The OCT imaging system configuration (Figure 6.3) details were the same as we described in our previous study [28]. We used a line-scan camera (EM4, e2v, USA) with 12-bit depth and 2048 pixels as the spectrometer detector. We used a SLED light source with an output power of 10mW and an effective bandwidth of 105nm centered at 845 nm. The system ran at a 70 kHz line rate with an axial resolution of 3.0 μm in air and transversal resolution of approximately 12 μm. The detectable range of the

velocity of flowing target projected to the parallel direction of the scanning beam was [14.2, 0.294]∪[0.294, 14.2] mm/s. Each B-scan image consisted of 1000 A-scans, and each C-scan consisted of 250 B-scans. The physical lateral image scanning range can be varied depending on the surgical site, which was usually limited within an area of 1.5 by 1.5 mm^2. Simultaneous structure and flow volume rendering images were presented immediately after the acquisition. A separate Carl Zeiss surgical microscope with maximum optical power of 20x was put aside and close to the OCT system, so that the rat could be easily transferred back and forth under two different systems. OCT systems can potentially be combined with the surgical microscope, which has already been demonstrated [142]. Six to eight weeks old inbred Lewis rats (Harlan) were anesthetized using Isoflurane based anesthesia system. Femoral (ID: 0.8-1 mm) and popliteal arteries (ID: 0.4-0.6 mm) were exposed through an anteromedial skin incision. After dissection using standard optical microscope, framed approximator clamps (S&T, Neuhausen, Switzerland) were applied. Vessel was divided with a micro scissor and then shifted to the OCT platform. The anastomosis was performed using conventional interrupted 10-0 Nylon 6-8 sutures. In our preliminary experiments, the platform was rotated from optical microscope to OCT system after each suture placement. After re-vascularization, vessels were evaluated with PRDOCT for qualitative flow analysis and thrombus formation. Animal body temperature was maintained using heating pad. Room temperature was kept between 70-75 F° in the operating room. Heating pad, however, was not used on the OCT platform but can

be included in the future studies. The animal study was conducted in accordance with the Johns Hopkins University Animal Care and Use Committee Guidelines.

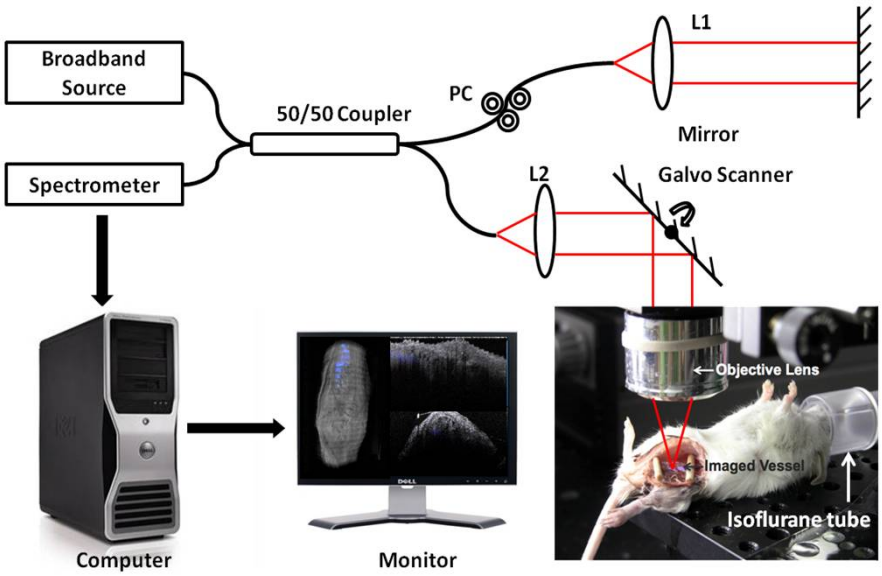

Figure 6.3: System Configuration (PC: polarization controller, L1, L2: focusing lens, 2D Galvo scanner was depicted only in 1D for simple demonstration, the animal could be either mouse or rat).

Either the left or right femoral artery of the limb was exposed through a surgical procedure, as shown in Figure 6.4(b). A tiny plastic rubber sheet was placed underneath the vessel to isolate the vessel from surrounding soft tissue for better surgical operation and imaging. The microvascular anastomosis was performed on the same vessel after both the distal and proximal end of the anastomosed site were clamped and cut into two half ends. Sutures were placed in the collapsed vessel from adventitia through intima on one end, followed by suture placement from intima to adventitia on the other vessel end. Sutures were laid down flat and tightened, which approximated the intima, while the lumen was opened to allow placement of sutures. Sutures were

then applied circumferentially for the anastomosis, making a complete seal to prevent leakage, as shown in Figure 6.4(c). Finally, the clamp was removed and blood went through the vessel without leakage or thrombus within the vessel if the procedure succeeded, as shown in Figure 6.4(d). Among all the circumferential sutures usually from 6 to 8 sutures should avoid accidentally going through both walls of one vessel, as shown in Figure 6.4(a). Otherwise, following the suture-tying procedure will close the vessel lumen, which will cause direct failure of the surgery.

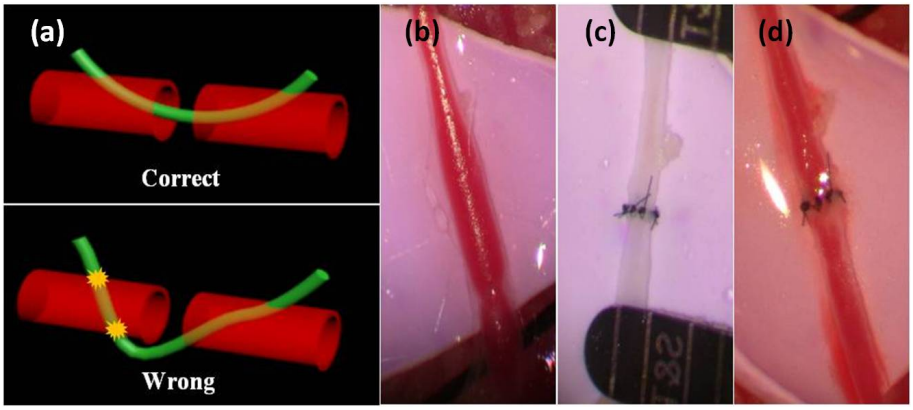

Figure 6.4: (a) illustration of the correct and wrong suturing procedures, (b) naive artery before microvascular anastomosis, (c) connected artery after 6 suturing, (d) connected artery with vessel clamp removed and blood flow restored.

6.3 Results and Discussion

The transparent nature of extremely thin vessels, as shown in Figure 6.5(a), poses a challenge to the surgeon viewing the anterior and posterior vessel walls through an optical microscope, and the surgeon relies mainly on tactile stimuli. Hence, from

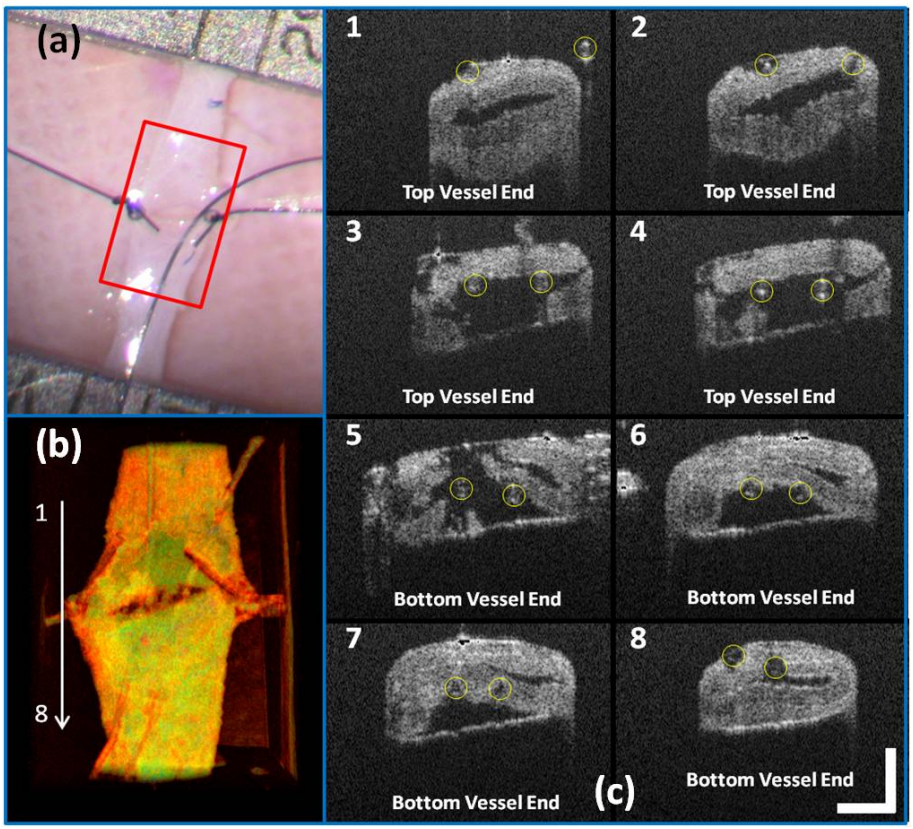

Figure 6.5: (a) Surgical microscope view of the surgical site, (b) top-view volume rendering of the 3D OCT image data corresponding to the red box in (a), (c) selected numbered B-mode frames in the direction of the arrow in (b) out of the video (scale bar: 200 μm).

a technical viewpoint, the risk of error increases towards the end of the procedure, when the maneuverability is limited due to the already-tied sutures. The risk can be proportionately higher in beginners with less experience. Figure 6.5 depicts the wrong suture placement during the procedure. For the first two sutures, the surgeon was confident about the correct placement; however, when it came to the 3rd, 4th, and additional sutures, OCT imaging was introduced to check and confirm the precise suture position relative to the vessel walls before tying knots. The total OCT imaging

time for all the sutures cost around 8 mins due to the real-time image acquisition and processing, which added a marginal burden to the overall average time of 47 mins without OCT imaging [136]. As most of the 8 mins was spent on transferring the animal back and forth and focusing on the area of interest, we would expect a much-reduced time cost when a future OCT system is integrated with a surgical microscope.

Figure 6.5(a) shows the surgical microscope view of a transparent vessel with two sutures tied and one suture going through both ends. After placing 4 sutures through both the proximal and distal cut ends, we imaged the red rectangular area marked in Figure 6.5(a) using OCT. Figure 6.5(b) is the corresponding top view volume rendering of the surgical site. We can clearly see the whole surgical site. First and second threads were intraluminal at the cut-end. However, 3rd and 4th suture went through both anterior and posterior walls of the distal cut end of the vessel. It offered the surgeon a general scene of the surgical site. Figure 6.5(c) consists of eight cross-sectional B-mode frames marked in the direction of the white arrow in Figure 6.5(b) selected from the volume image data. Sutures were marked with yellow circles in Figure 6.5(c). It demonstrates an example of technical error where an accidental back wall suture occludes the vessel lumen. We presented eight slices over the imaging volume to trace the sutures through both vessel walls. Slice 1-4 assures that suture 3 and 4 went through the proximal vessel end accurately. However error was found when the sutures went through the distal cut-end of the vessel. Slice 5 demonstrates that the sutures went through the posterior vessel wall. Slice 6 depicts

both sutures entering the posterior vessel wall while slice 7 indicates the moment that both sutures were inside the posterior wall. Finally slice 8 shows both sutures were inside the anterior wall. These four slices assured the surgeon that the lumen would be occluded. The suture was lying within the adventitia of the posterior wall and could not be visualized through the optical microscope. This error was successfully detected by the OCT image and allowed the surgeon to re-do the third and fourth suture to successfully perform the anastomosis.

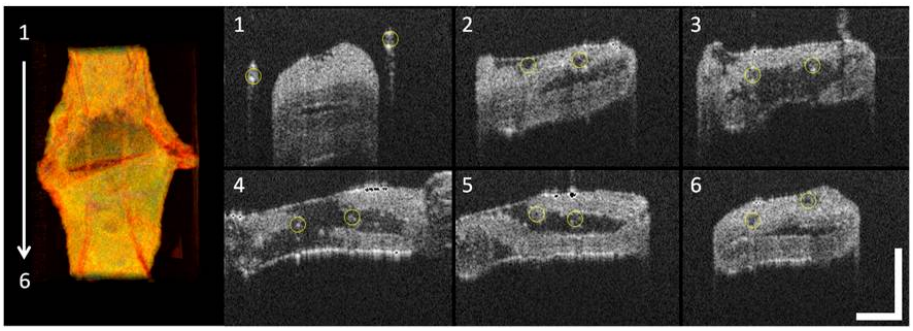

Figure 6.6: Selected OCT sequential images showing the correct suture position relative to vessel walls (sutures were marked by yellow circles on the image, scale bar: 200 μm).

Figure 6.6 represents accurate suture placement relative to the vessel walls. After confirming by the OCT imaging that there was no error, the surgeon continued to perform the rest of the sutures.

The key parameter to determine the surgical outcome is whether the blood flow could be restored. Because the vessels are so delicate, endothelial injury, mal-positioned or partial thickness sutures can induce turbulence or thrombosis. If the thrombosis occludes the vessel lumen with no flow distally, all the previous steps have to be re-

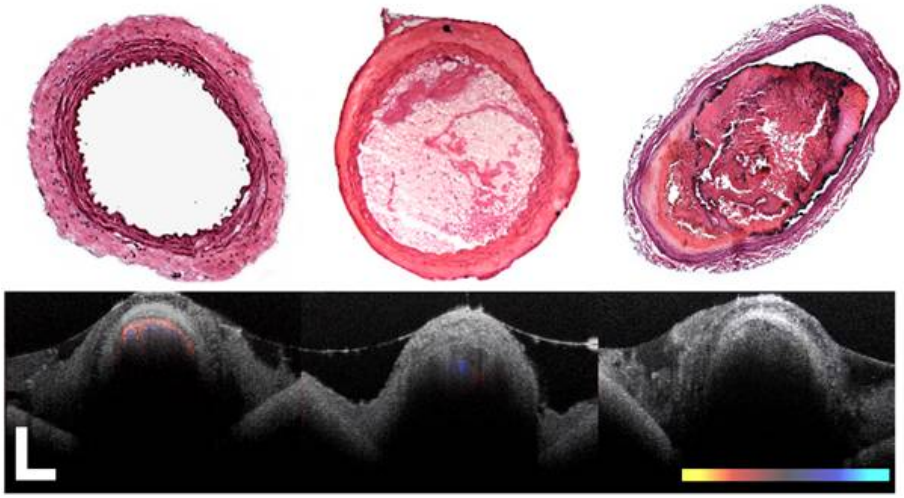

Figure 6.7: Naive, partial and full thrombosis imaging (left to right) correlation between histology (top row) and OCT (bottom row), scale bar: 200 μm

done. But sometimes the thrombus formation is not immediate or the thrombus is not large enough to completely occlude the vessel. In such a situation, visual input from an optical microscope can deceivingly show flow restoration. Structure and Doppler flow information from the PRDOCT can help the surgeon evaluate the quality of flow restoration and early thrombus formation. We validated the thrombosis detection capability of our system through comparison with gold standard histology analysis. The thrombosis was induced using the $FeCl_3$ solution model [143]. Figure 6.7 shows the result. In naive group we can see clean and smooth inner lumen from the structure image and well distributed Doppler signal inside the lumen. However, in partial thrombosis group, OCT image found structural irregularities along the inner vessel wall. Doppler signal also demonstrated flow alterations not coinciding with the luminal flow pattern of nave intact vessel. Finally in the full thrombosis group

Doppler signal completely disappeared. Besides Doppler signal, liquid blood can also be differentiated from solid thrombosis based on their speckle size [144].

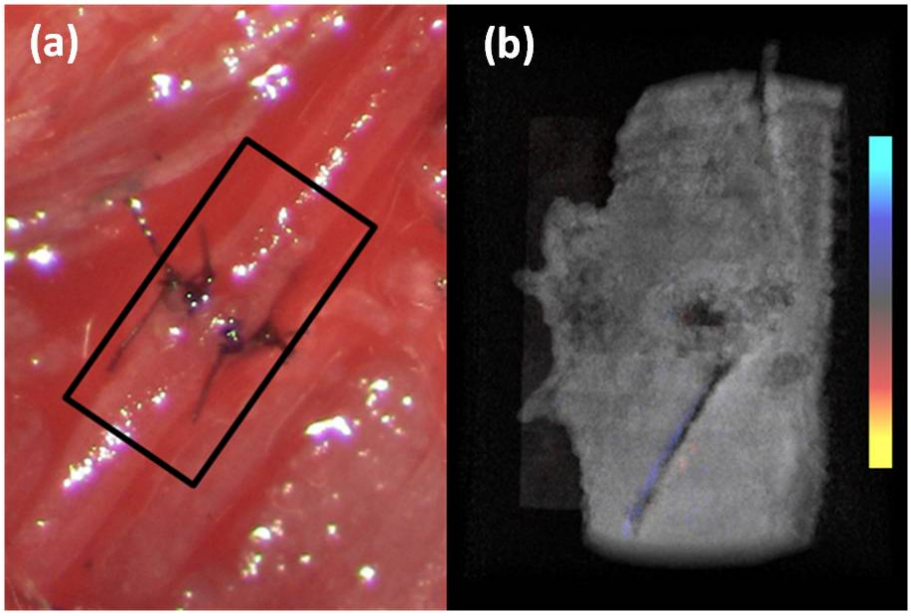

Figure 6.8: (a) Surgical microscope view of the connected vessel with clamp removed, (b) structural and flow overlaid top-view volume rendering of the area marked with black box in (a).

6.3.1 Rat Femoral Artery Anastomosis

We report two cases here. In the first case, the blood flow was not restored. The result is shown in Figure 6.8. Figure 6.8(a) was a camera image of the vessel under microscope. Figure 6.8(b) was the structural and flow overlaid top view volume rendering of the black box marked area in Figure 6.8(a). There was no Doppler signal indicating blood flow. This tells the surgeon that the whole procedure needs to be re-done; however, with Figure 6.8(a) only, it is really hard for the surgeon to know

whether there is flow.

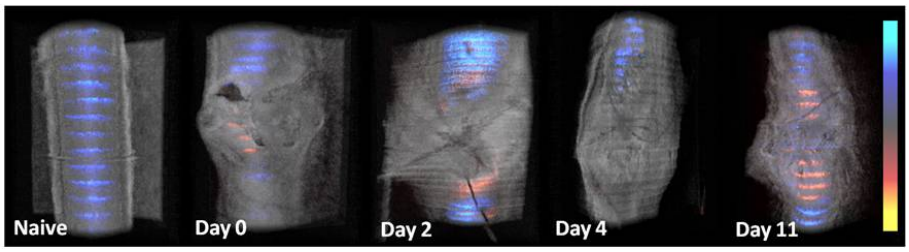

Figure 6.9: PRDOCT 3D volume imaging of the surgical site over 11 days.

The second case was a successful microvascular anastomosis followed by a long-term study. For each subsequent analysis, skin incisions were re-opened and closed using 4-0 Nylon interrupted sutures. Figure 6.9 shows the time-elapsed OCT imaging of the surgical site. From the naive state we can clearly visualize the normal healthy pulsation effect of the blood flow in the artery. The inner vessel lumen diameter measured by from OCT images stays at the same level around 0.4 mm, except for Day 2 when the vessel inner lumen diameter went up to 0.5 mm, which we suspect might be due to vasodilation. The junction area of two connected vessel ends immediately after the surgery was marked by Day 0. Compared to Figure 6.8, there was an obvious blood flow signal in all the Doppler images. At the junction area, densely distributed suture ties and connective tissue may limit the OCT image penetration depth into the vessel; thus, blood flow information was weak in the junction area. However, general flow distribution from the proximal to distal end of the anastomosed vessel could be viewed. From the Day 0 flow image, we can see that the flow tunnel in the junction area was curved instead of being straight. This might not be a well-sutured

vessel tunnel intuitively. However, no previous work has ever been able to resolve the anastomosed vessel flow distribution at such a high-resolution 3D level. Detailed study will be performed in the future to study the effect of vessel tunnel shape and connectivity on the survival rate of microvascular anastomosis. The complicated and irregular inner lumen at the junction area will produce flow turbulence and make the flow change directions instead of being unidirectional, which explains the unusual red blood flow signal in the junction area; however, we do observe blood flow signal in the distal end though weak compared to the proximal end. The blood flow was qualitatively better on Day 2 flow image as the rat recovered gradually. Day 4 flow image shows that there was a partial thrombosis in the junction area and nearby, as there was still some evidence of flow. A week later the thrombus disappeared as seen in Day 11 flow image. The blood flow was comparable to a naive state, though there was still some narrowing and turbulence in the middle of the junction area.

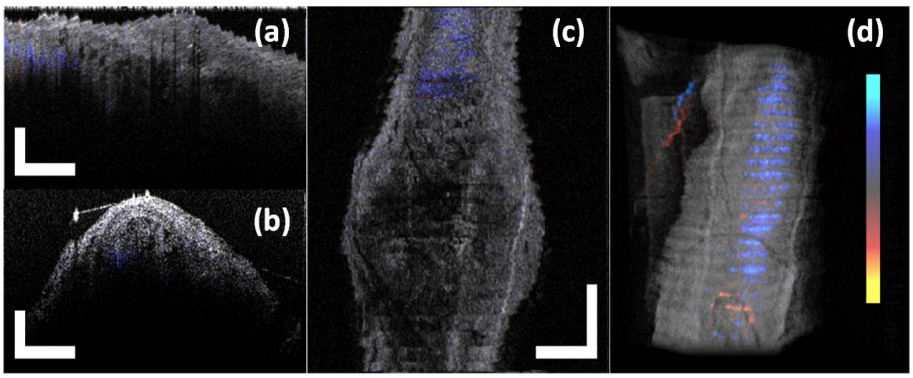

Figure 6.10: Structure and Doppler flow overlaid images at Day 4 of the surgical junction site(a) Sagittal-plane slice, (b) cross-sectional plane slice, (c) depth z-slice; (d) PRDOCT imaging of the distal end of the anastomosed vessel (scale bar: 200 μm).

Figure 6.10 imaged at Day 4 confirmed that the thrombosis was partial. Figure 6.10(ac) were three orthogonal plane image slices showing the area of interest of the anastomosed vessel. We overlaid the Doppler signal with the structure information together. There was little blood flow at the left side of Figure 6.10(a), at the bottom of Figure 6.10(b), or at the top of Figure 6.10(c). The porous structure that attached to the inner vessel lumen was the thrombosis based on our experimental thrombosis imaging studies. Due to limited image penetration depth of 900nm band light in the blood usually around 230 μm [145], we cannot see through the vessel wall all the way to the bottom; however, there was obvious blood flow beneath the thrombosis. Figure 6.10(d) was the distal artery imaging away from the connected junction. It confirmed that there was still blood flow in the artery and that the thrombosis at the junction area was partial. The vessel lumen was not fully occluded. Being able to detect the thrombosis offers the surgeon an opportunity to salvage the free flap or composite tissue through re-anastomosis or pharmacologic thrombosis. No therapeutic procedure was performed in this case. The Day 11 image clearly shows that the thrombus had resolved over time.

On Day 11 the rat was sacrificed for histology analysis. OCT slices imaging was compared to the standard histology image in Figure 6.11. Figure 6.11(a) was a histology slice image along the long axis of the vessel. Features were marked out in the image. From Figure 6.11(a), we can see the anastomotic narrowing due to indentation of vessel wall. There was still a small thrombus near the junction area, which was

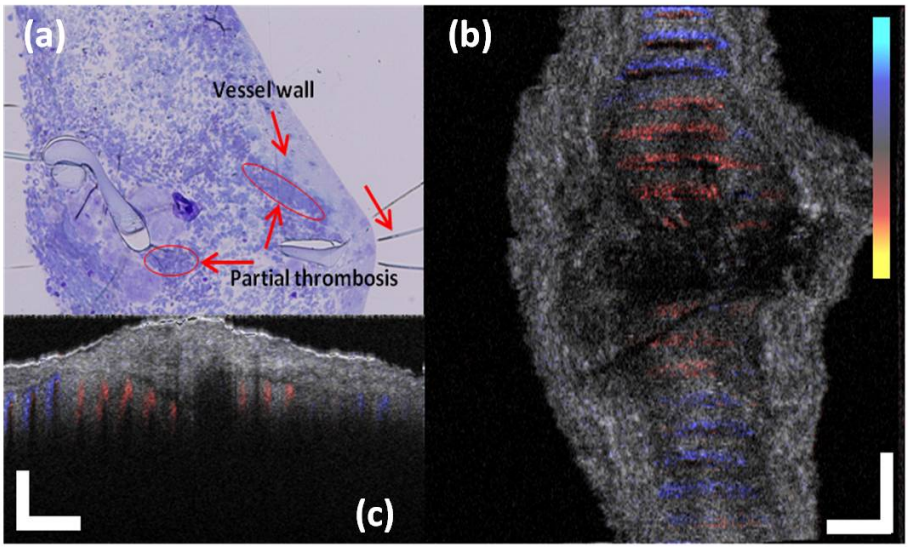

Figure 6.11: (a) Histology image of a thin slice along the vessel long axis, (b) structure and Doppler flow overlaid Z-slice OCT image of junction area, (c) structure and Doppler flow overlaid sagittal-plane slice of junction area (scale bar: 200 μm).

not significant enough to occlude the vessel wall. It is particularly important to have some degree of thrombosis at the anastomotic site to prevent blood from leaking out of vessel immediately after re-vascularization. The morphology of the thrombosis became dense instead of being porous in the Day 4 OCT image. Figure 6.11(b) was one OCT z-slice image with structure and flow information overlaid. We can clearly visualize the turbulence phenomenon and the narrowing and bending of the blood tunnel at the junction area, as shown by the histology result. A small amount of dense thrombus attached to the inner lumen wall at the junction area thickened the inner wall. Figure 6.11(c) explains the cause of turbulence, indented vessel wall forcing the blood flow to change the direction from moving upward to downward.

6.3.2 Mouse Femoral Artery and Vein Anastomosis

We performed a detailed systematic investigation of mouse femoral artery and vein anastomosis to study common possible surgical complications and evaluate the long term prediction capability of OCT. There are four principles for anastomosis. Avoid luminal narrowing at the anastomosis site. Avoid the creation of folds and a rough inner surface of the vessel. Oppose the two intimal edges closely. Eliminate contact of suture material with blood. We will explore how these four principles work in mouse femory vessel experiment.

First, we introduced a series of error operation during the surgery to both artery and vein of the mouse. Then OCT images and camera captured surgical images were acquired to test whether OCT can detect all these problems. Figure 6.12 demonstrates two basic detrimental errors. One is adventitia folding and the other is suture placed across both anterior and posterior walls of the vessel. For the adventitia folding it is very hard to diagnose this from the Day 0 camera image. However, the OCT images clearly show that there was no blood flow restored and 5 hours later even the camera image started to show the effect of thrombosis. For the sutures crossing both anterior and posterior walls, it is very easy to identify this from both the camera and OCT images.

Figure 6.13 demonstrates the effect of suture blood contact and severe lumen

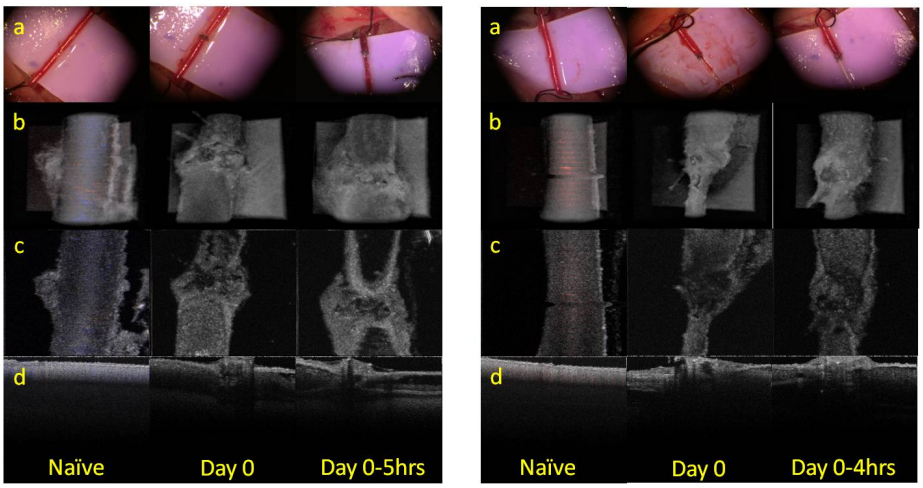

(A) (B)

Figure 6.12: (A)adventitia Folding; (B) suture crosses both posterior and anterior walls. a) camera images. b) top view volumetric c) z-slice d) sagittal slice structure and Doppler flow overlaid images

narrowing at the anastomotic site. Again in the Day 0 image, it is very hard for the surgeon to tell whether the blood has been restore or not. And OCT images accurately diagnosed the surgical failure. Figure 6.13 (A) illustrates the importance of principle of eliminating contact of suture material with blood, as the alien debris will induce acute thrombus after the surgery. Figure 6.13 (B) shows another example of the effect of anastomotic site lumen narrowing. No successful blood restoration was observed from the OCT images. Figure 6.14 shows one more example of severe lumen narrowing with barely noticeable blood flow in the OCT image. From the camera images we can see some abnormalities in the vessel diameter around the anastomotic site and blood refill status. From the OCT images, the inner structure and blood flow were depicted clearly. Huge thrombosis was formed at the surgical site, the blood flow was very weak. One day later the artery was totally occluded.

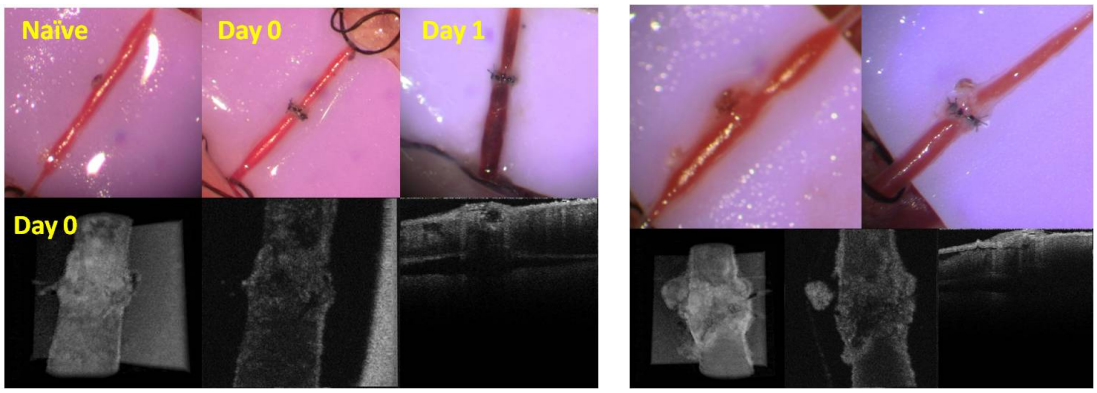

(A) (B)

Figure 6.13: (A)suture blood contact; (B) severe lumen narrowing

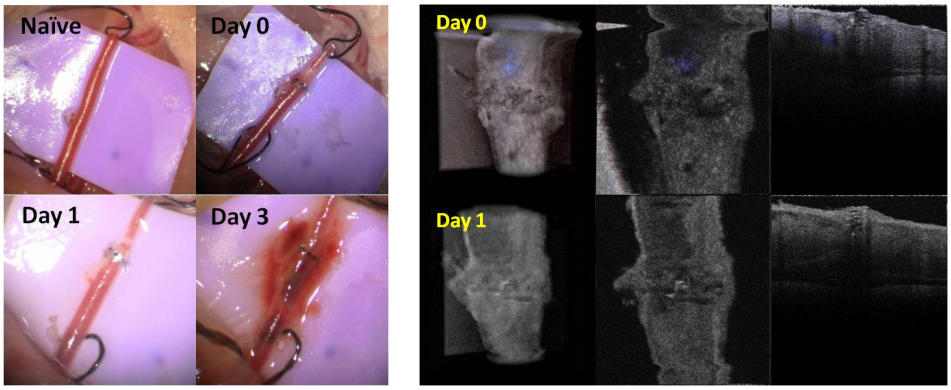

(A) (B)

Figure 6.14: Severe lumen narrowing with barely noticeable blood flow (A)camera images taken at different days; (B) corresponding OCT images taken at different days

While OCT can diagnose surgical failures immediately without problem, the capability of OCT to predict long term successful surgical outcome is also appreciated. We presented two successful vascular anastomosis cases here, one is on the femoral artery and the other is on the femoral vein, shown in Figure 6.15 and Figure 6.16 respectively. By comparison with the failure examples, we analyzed the long term imaging track results. Several key features are extracted to ensure long term success.

First of all, the initial blood flow after removing the clamp should be relative strong. Second, the there should be a clean junction site with the intima from two vessel ends approximating each other as close as possible. This makes the intimas easier to grow connected in the long run. Tiny amount of thrombus is acceptable at the surgical site, as shown in Figure 6.16 Day 0 OCT Z-slice imaging. One day later the tiny thrombus was resolved and clean smooth intima was revealed.

After practicing on the separate artery and vein imaging, we started to analyze the leg transplantation surgery. During which, both the artery and vein need to be connected. Figure 6.17 and Figure 6.18 show the suture based mouse leg transplantation on Day 0 and Day 21 respectively. Based on Day 0 image, we can clearly visualize strong initial blood flow and there is no severe lumen narrowing and adventia folding is also negligible. Though tiny partial thrombus was observed in the artery. The intima was clean and close to each other. We are sure that it will be a successful one. Day 21 imaging confirmed our predication. The intima grew connected and the thrombus was also resolved.

Figure 6.19 and Figure 6.20 show the cuff based mouse leg transplantation on Day 0 and Day 14 respectively. Cuff based anastomosis has the advantage of minimal vessel injury and it avoids the suture placement error. Day 0 image clearly show the well restored blood flow. Day 14 imaging confirmed its long term results.

Figure 6.21 shows the photo of the mouse after suture based transplantation (a) and cuff based transplantation (b).The skin and claw of the mouse both show reddish

surface which is an indication of healthy blood flow inside the tissue.

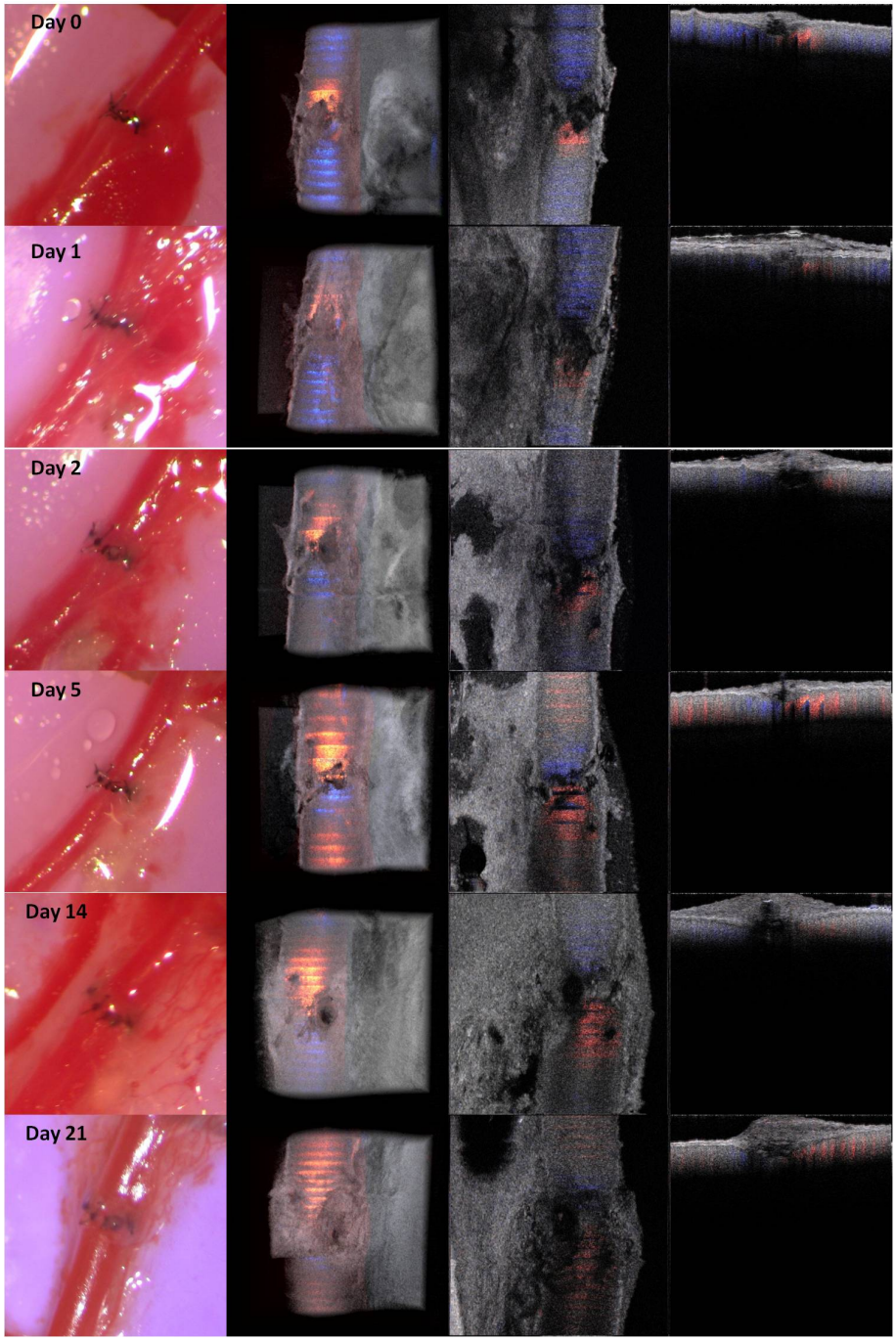

Figure 6.15: One successful long term study of femoral artery anastomosis over 21 days.

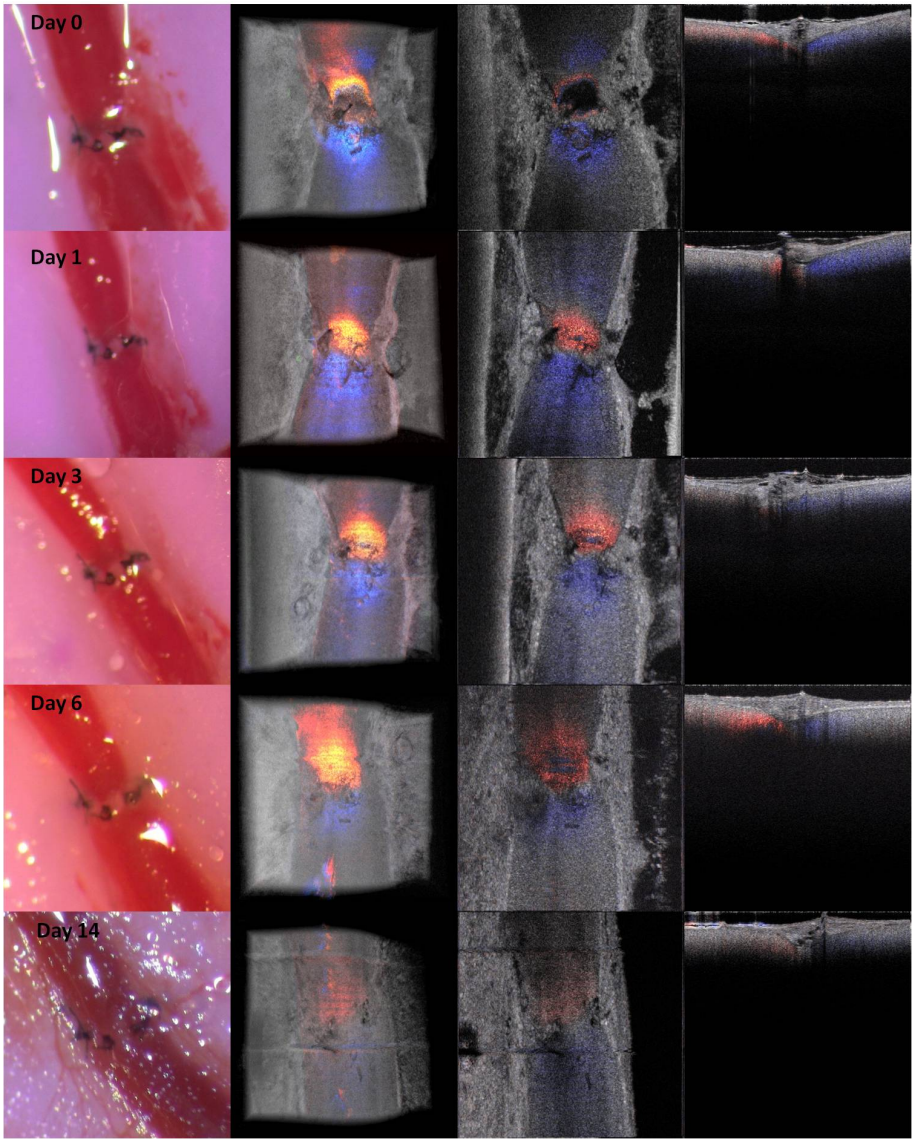

Figure 6.16: One successful long term study of femoral vein anastomosis over 14 days.

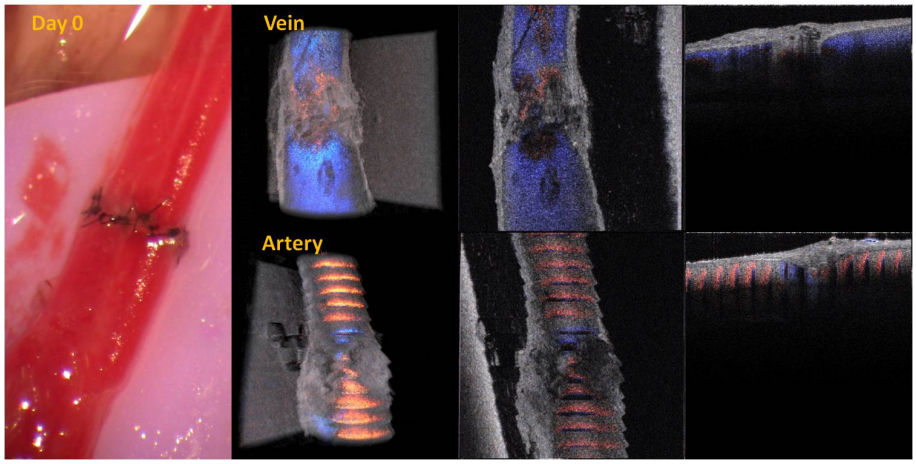

Figure 6.17: Sutured mouse leg transplantation on Day 0.

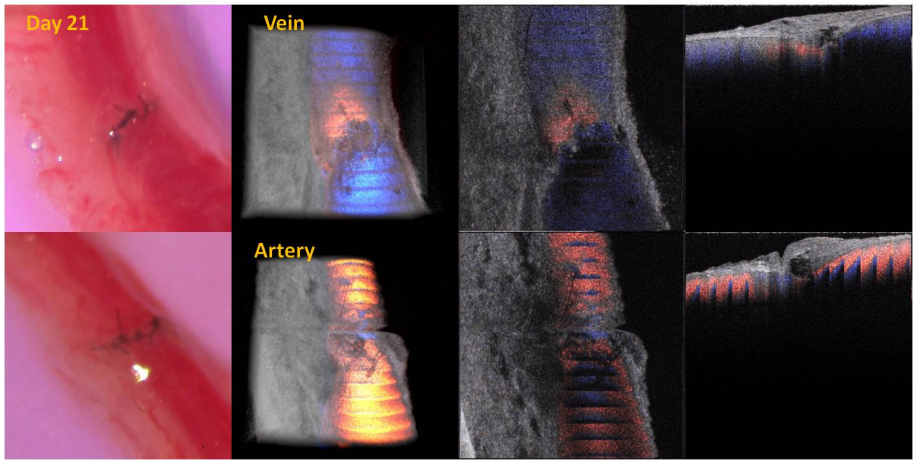

Figure 6.18: Sutured mouse leg transplantation on Day 21.

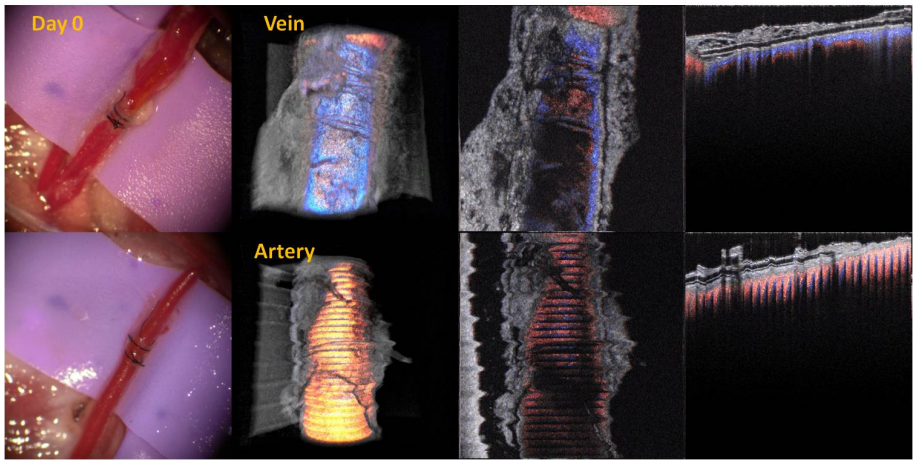

Figure 6.19: Cuff based mouse leg transplantation on Day 0.

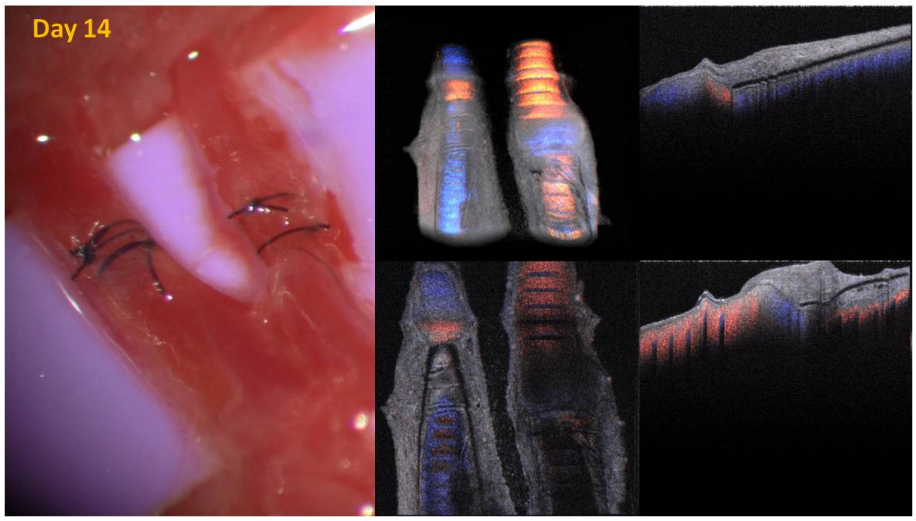

Figure 6.20: Cuff based mouse leg transplantation on Day 14.

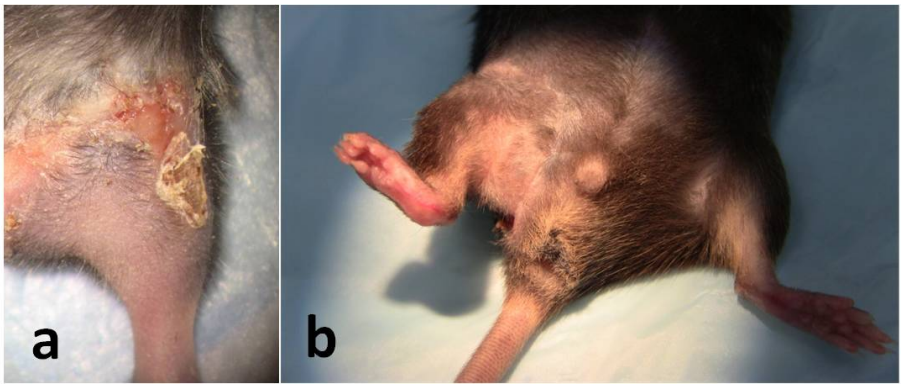

Figure 6.21: (a)camera image of the transplanted leg using suturing technique on Day 21; (b)camera image of the transplanted leg using cuff based technique on Day 14.

6.4 Conclusion

We demonstrated that real-time PRDOCT imaging can guide microvascular anastomosis, reduce the risk of technical failure, and provide immediate evaluation of the surgical outcome. Furthermore, this imaging modality can promptly diagnose early thrombus formation and potentially predict its progression. It can be used to provide rapid feedback for self-training as well as instructor led training. In addition, OCT can be of great importance as interventional and diagnostic tool. In our future research directions, we will combine this technique with a conventional surgical microscope to further optimize and improve surgical outcomes. A clinical environment using friendly miniature handheld probe will also be another direction to proceed with. This innovative imaging modality has great potential to broaden the scope of reconstructive microsurgery through improved surgical precision and better surgical outcomes for extremely small vessels (diameter less than 1.0 mm).

Chapter 7

Conclusion

This Chapter summarizes what have been achieved in this dissertation. This is followed by a discussion of possible future work.

7.1 Summary of Contributions

In this dissertation, advanced high-speed Fourier domain optical coherence tomography (FD-OCT)systems were investigated and developed. Several real-time, high-resolution functional Spectral-domain OCT (SD-OCT) systems capable of imaging and sensing blood flow and motion were designed and developed.

First of all, GPU accelerated real-time reference A-line subtraction and saturation correction algorithms and phase resolving algorithm were developed and integrated into previously developed hybrid CPU-GPU OCT signal processing architecture seam-

lessly. The reference A-line subtraction avoids a separate reference spectrum measurement and adapts according to the time varying reference power real-time. Meanwhile by perform real-time updated reference subtraction, OCT image quality is improved in terms of SNR. GPU accelerated phase resolving algorithm enriches the functionality of our current SD-OCT system by allowing simultaneous flow and structure imaging. I also evaluated customized ray casting based Doppler volume rendering to better present the flow information. GPU accelerated zero-padding based FFT and simple cross correlation based registration for CP-OCT system were integrated and used to perform real-time distance sensing, motion compensation and OCT topology correction. The zero-padding increases the system distance sensing sensitivity by an order of ten.

Second, different applications that can utilize the capability of distance sensing of CP-OCT systems were evaluated. By integrating a CP-OCT distance sensor to a fiber bundle based confocal microscope, the involuntary motion compensation of the sample was achieved. This allows a long term study of bio-samples free from axial motion distortion in circumstances where even short distance axial motion will cause signal loss. Then a novel CP-OCT based intraocular lens (IOL) power measurement method was developed. This method reconstructs the surface contour of IOLs which is free of geometrical distortion encountered in standard OCT system. It also enables the *in vitro* measurement, which was impossible before.*In vitro* measurement provides the surgeon more accurate lens power data for implantation. Finally a handheld CP-

OCT imaging probe capable of motion compensation for the purpose of microsurgery guidance was developed.By keeping the distance between the fiber tip and sample at a constant value, the probe was able to compensate the involuntary tissue motion and hand vibration while acquiring OCT images.

Finally, By utilizing the capability of OCT several different clinical applications were assessed. First, the full-range complex OCT system for mouse atherosclerosis detection with a potential in future intraoperative carotid endarterectomy (CEA) surgery. At the same time, by using OCT plaque detection, pravastatin therapy efficiency was evaluated. Second, phase resolved Doppler OCT was used for microvascular anastomosis in rodent model. OCT is able to guide the suture placement and evaluate poster surgical outcome. It has now been extensively used for suturing and non-suture based technique evaluation and surgical training.

7.2 Future Perspective

In the future, this research will be expanded into a broader and more comprehensive imaging program. Functional imaging capabilities such as spectroscopic, phase sensitive imaging and combination of full-range OCT and Doppler OCT to provide physiological and pathological information can be added to the system. Advanced imaging processing methods can be adapted into current system to improve the image quality. Further development of the motion compensation algorithm and optical

mechanical design are needed to make the handheld probe more functional and intelligent. For the microsurgery evaluation and assessment, there will be a focus on developing a miniature handheld probe with the size similar to common surgical tools such as a scissor or tweezer to facilitate the intraoperative application in clinical environment.

Bibliography

[1] W. Drexler and J. Fujimoto, *Optical Coherence Tomography, Technology and Applications*. NY, USA: Springer, 2008.

[2] P. Hahn, J. Migacz, R. O'Connell, R. Maldonado, J. Izatt, and C. Toth, "The use of optical coherence tomography in intraoperative ophthalmic imaging," *Ophthalmic Surg Lasers Imaging*, vol. 42, no. 0, pp. 85–94, 2011.

[3] T. Peters and K. Cleary, *Image-Guided Interentions, Technology and Applications*. New York, USA: Springer, 2008.

[4] D. Huang, E. Swanson, C. Lin, J. Schuman, W. Stinson, W.Chang, M. Hee, T. Flotte, K. Gregory, C. Puliafito, and J. Fujimoto, "Optical coherence tomography," *Science*, vol. 254, no. 5035, pp. 1178–1181, 1991.

[5] A. Fercher, C. Hitzenberger, G. Kamp, and S. EI-Zaiat, "Measurement of intraocular distances by backscattering spectral interferometry," *Optics Communincations*, vol. 117, no. 1-2, pp. 43–48, 1995.

BIBLIOGRAPHY

[6] S. Boppart, B. Bouma, C. Pitris, G. Tearney, J. Southern, M. Brezinski, and J. Fujimoto, "Intraoperative assessment of microsurgery with three-dimensional optical coherence tomography," *Radiology*, vol. 208, no. 1, pp. 81–86, 1998.

[7] M. Gora, K. Karnowski, M. Szkulmowski, B. J. Kaluzny, R. Huber, A. Kowalczyk, and M. Wojtkowski, "Ultra high-speed swept source oct imaging of the anterior segment of human eye at 200 khz with adjustable imaging range," *Optics Express*, vol. 17, no. 17, pp. 14 880–14 894, 2009.

[8] B. Potsaid, I. Gorczynska, V. J. Srinivasan, Y. Chen, J. Jiang, A. Cable, and J. G. Fujimoto, "Ultrahigh speed spectral / fourier domain oct ophthalmic imaging at 70,000 to 312,500 axial scans per second," *Optics Express*, vol. 16, no. 9, pp. 15 149–15 169, 2008.

[9] R. Huber, D. C. Adler, and J. G. Fujimoto, "Buffered fourier domain mode locking: unidirectional swept laser sources for optical coherence tomography imaging at 370,000 lines/s," *Optics Letters*, vol. 31, no. 20, pp. 2975–2977, 2006.

[10] T. Klein, W. Wieser, C. Eigenwillig, B. Biedermann, and R. Huber, "Megahertz oct for ultrawide-field retinal imaging with a 1050 nm fourier domain mode-locked laser," *Optics Express*, vol. 19, no. 4, pp. 3044–3062, 2011.

[11] I. Grulkowski, J. J. Liu, B. Potsaid, V. Jayaraman, C. D. Lu, J. Jiang, A. E. Cable, J. S. Duker, and J. G. Fujimoto, "Retinal, anterior segment and full

eye imaging using ultrahigh speed swept source oct with vertical-cavity surface emitting lasers," *Biomedical Optics Express*, vol. 3, no. 11, pp. 2733–2751, 2012.

[12] T. E. Ustun, N. V. Iftimia, R. D. Ferguson, and D. X. Hammera, "Real-time processing for fourier domain optical coherence tomography using a field programmable gate array," *Review of scientific instruments*, vol. 79, no. 11, p. 114301, 2008.

[13] A. E. Desjardins, B. J. Vakoc, M. J. Suter, S.-H. Yun, G. J. Tearney, and B. E. Bouma, "Real-time fpga processing for high-speed optical frequency domain imaging," *IEEE Trans Med Imaging*, vol. 28, no. 9, pp. 1468–1472, 2009.

[14] G. Liu, J. Zhang, L. Yu, T. Xie, and Z. Chen, "Real-time polarization-sensitive optical coherence tomography data processing with parallel computing," *IEEE Trans Med Imaging*, vol. 48, no. 32, pp. 6365–6370, 2009.

[15] J. Probst, D. Hillmann, E. Lankenau, C. Winter, S. Oelckers, P. Koch, and G. Httmann, "Optical coherence tomography with online visualization of more than seven rendered volumes per second," *Journal of Biomedical Optics*, vol. 15, no. 2, p. 026014, 2010.

[16] Y. Watanabe and T. Itagaki, "Real-time display on fourier domain optical coherence tomography system using a graphics processing unit," *Journal of Biomedical Optics*, vol. 14, no. 6, p. 060506, 2009.

[17] K. Zhang and J. U. Kang, "Real-time 4d signal processing and visualization using graphics processing unit on a regular nonlinear-k fourier-domain oct system," *Optics Express*, vol. 18, no. 11, pp. 11 772–11 784, 2010.

[18] S. V. der Jeught, A. Bradu, and A. G. Podoleanu, "Real-time resampling in fourier domain optical coherence tomography using a graphics processing unit," *Journal of Biomedical Optics*, vol. 15, no. 3, p. 030511, 2010.

[19] Y. Watanabe, S. Maeno, K. Aoshima, H. Kasegawa, and H. Koseki, "Real-time processing for full-range fourier domain optical coherence tomography with zero-filling interpolation using multiple graphics processing units," *Applied Optics*, vol. 49, no. 25, pp. 4756–4762, 2010.

[20] K. Zhang and J. U. Kang, "Grphics processing unit accelerated non-uniform fast fourier transform for ultrahigh-speed, real-time fourier-domain oct," *Optics Express*, vol. 18, no. 22, pp. 23 472–23 487, 2010.

[21] ——, "Real-time intraoperative 4d full-range fd-oct based on the dual graphics processing units architecture for microsurgery guidace," *Biomedical Optics Express*, vol. 2, no. 4, pp. 764–770, 2011.

[22] J. Rasakanthan, K. Sudgen, and P. H. Tomlins, "Processing and rendering of fourier domain optical coherence tomography images at a line rate over 524khz using a grapics processing unit," *Journal of Biomedical Optics*, vol. 16, no. 2, p. 020505, 2011.

[23] K. Lee, A. Mariampillai, J. Yu, D. Cadotte, B. Wilson, B. Standish, and V. Yang, "Real-time speckle variance swept-source optical coherence tomography using a graphics processing unit," *Biomedical Optics Express*, vol. 3, no. 7, pp. 1557–1564, 2012.

[24] L. Wang, B. Hofer, J. A. Guggenheim, and B. Povazay, "Graphics processing unit-based dispersion encoded full-range frequency-domain optical coherence tomography," *Biomedical Optics Express*, vol. 17, no. 7, p. 077007, 2012.

[25] Y. Huang and J. U. Kang, "Real-time reference a-line subtraction and saturation artifact removal using graphics processing unit for high-frame-rate fourier domain optical coherence tomography video imaging," *Optical Engineering*, vol. 51, no. 7, p. 083201, 2012.

[26] Y. Watanabe, "Real-time processing of fourier domain optical coherence tomography with fixed-pattern noise removal by partial median subtraction using a graphics processing unit," *Journal of Biomedical Optics*, vol. 17, no. 5, p. 050503, 2012.

[27] H. Jeong, N. Cho, U. Jung, C. Lee, J. Kim, and J. Kim, "Ultra-fast displaying spectral domain optical doppler tomography system using a graphics processing unit," *Sensors*, vol. 12, no. 6, pp. 6920–6929, 2012.

[28] Y. Huang, X. Liu, and J. U. Kang, "Real-time 3d and 4d fourier domain

doppler optical coherence tomography based on dual graphics processing units," *Biomedical Optics Express*, vol. 3, no. 7, pp. 2162–2174, 2012.

[29] M. Sylwestrzak, D. Szlag, M. Szkulmowski, I. Gorczynska, D. Bukowska, M. Wojtkowski, and P. Targowski, "Four-dimensional structural and doppler optical coherence tomography imaging on graphics processing units," *Journal of Biomedical Optics*, vol. 17, no. 10, p. 100502, 2012.

[30] Y. Jian, K. Wong, and M. V. Sarunic, "Graphics processing unit accelerated optical coherence tomography processing at megahertz axial scan rate and high resolution video rate volumetric rendering," *Journal of Biomedical Optics*, vol. 18, no. 2, p. 026002, 2013.

[31] A. Yariv, *Optical Electronics in Modern Communications*. New York: Oxford University, 1997.

[32] R. Leitgeb, C. Hitzenberger, and A.Fercher, "Performance of fourier domain vs. time domain optical coherence tomography," *Optics Express*, vol. 11, no. 8, pp. 2183–2189, 2003.

[33] M. A. Choma, M. V. Sarunic, C. Yang, and J. A. Izatt, "Sensitivity advantage of swept source and fourier domain optical coherence tomography," *Optics Express*, vol. 11, no. 18, pp. 2183–2189, 2003.

[34] S. Moon, S. won Lee, and Z. Chen, "Reference spectrum extraction and fixed-

pattern noise removal in optical coherence tomography," *Optics Express*, vol. 18, no. 24, pp. 24 395–24 404, 2010.

[35] B. Hofer, B. Povaay, B. Hermann, S. M. Rey, V. Kaji, A. Tumlinson, K. Powell, G. Matz, and W. Drexler, "Artefact reduction for cell migration visualization using spectral domain optical coherence tomography," *Journal of Biophotonics*, vol. 4, no. 5, pp. 355–367, 2011.

[36] H. G. Bezerra, M. A. Costa, G. Guagliumi, A. M. Rollins, and D. I. Simon, "Intracoronary optical coherence tomography: a comprehensive review," *JACC: Cardiovascular interventions*, vol. 2, no. 11, pp. 1035–1046, 2009.

[37] S. Asrani, M. Sarunic, C. Santiago, and J. Izatt, "Detailed visualization of the anterior segment using fourier-domain optical coherence tomography," *Arch Ophthalmol*, vol. 126, no. 6, pp. 765–771, 2008.

[38] F. LaRocca, S. J. Chiu, A. Ryan P.MeNabb, N. Kuo, J. A. Izatt, and S. Farsiu, "Robust automatic segmentation of corneal layer boundaries in sdoct images using graph theory and dynamic programming," *Biomedical Optics Express*, vol. 2, no. 6, pp. 1524–1538, 2011.

[39] M. A. Choma, K. Hsu, and J. A. Izatt, "Swept source optical coherence tomography using an all-fiber 1300-nm ring laser source," *Journal of Biomedical Optics*, vol. 10, no. 4, p. 044009, 2005.

BIBLIOGRAPHY

[40] (2013, August) Nvidia cuda zone. [Online]. Available: https://developer.nvidia.com/category/zone/cuda-zone

[41] K. Zhang and J. U. Kang, "Real-time 4d numerical dispersion compensation using graphics processing unit for fourier-domain optical coherence tomography," *Electronics Letters*, vol. 47, no. 5, 2011.

[42] Z. Chen, T. Milner, S. Sriniyas, X. Wang, A. Malekafzali, M. van Gemert, and J. S. Nelson, "Noninvasive imaging of in vivo blood flow velocity using optical doppler tomography," *OpticsLetters*, vol. 22, no. 14, pp. 1119–1121, 1997.

[43] R. Wang, L. J. Steven, Z. Ma, S. Hurst, S. R. Hanson, and A. Gruber, "Three dimensional optical angiography," *OpticsExpress*, vol. 15, no. 7, pp. 4083–4097, 2007.

[44] A. Mariampillai, B. Standish, E. Moriyama, M. Khurana, N. Munce, M. K. Leung, J. Jiang, A. Cable, B. C. Wilson, A. Vitkin, and V. Yang, "Speckle variance detection of microvasculature using swept-source optical coherence tomography," *OpticsLetters*, vol. 33, no. 13, pp. 1530–1532, 2008.

[45] V. J. Srinivasan, J. Jiang, M. Yaseen, H. Radhakrishnan, W. Wu, S. Barry, A. Cable, and D. A. Boas, "Rapid volumetric angiography of cortical microvasculature with optical coherence tomography," *OpticsLetters*, vol. 35, no. 1, pp. 43–45, 2010.

[46] G. Liu, L. Chou, W. Jia, W. Qi, B. Choi, and Z. Chen, "Intensity-based modified doppler variance algorithm: application to phase instable and stable optical coherence tomography systems," *OpticsExpress*, vol. 19, no. 12, pp. 11 429–11 440, 2011.

[47] Y. Zhao, Z. Chen, C. Saxer, Q. Shen, S. Xiang, J. de Boer, and J. S. Nelson, "Doppler standard deviation imaging for clinical monitoring of in vivo human skin blood flow," *OpticsLetters*, vol. 25, no. 18, pp. 1358–1360, 2000.

[48] Y. Zhao, Z. Chen, Z. Ding, H. Ren, and J. Nelson, "Real-time phase-resolved functional optical coherence tomography by use of optical hilbert transformation," *OpticsLetters*, vol. 27, no. 2, pp. 98–100, 2002.

[49] Y. Tao, A. Davis, and J. Izatt, "Single-pass volumetric bidirectional blood flow imaging spectral domain optical coherence tomography using a modified hilbert transform," *OpticsExpress*, vol. 16, no. 16, pp. 12 350–12 361, 2008.

[50] Z. Yuan, Z. Luo, H. Ren, C. Du, and Y. Pan, "A digital frequency ramping method for enhancing doppler flow imaging in fourier-domain optical coherence tomography," *OpticsExpress*, vol. 17, no. 5, pp. 3951–3963, 2009.

[51] B. Baumann, B. Potsaid, M. Kraus, J. Liu, D. Huang, J. Hornegger, A. Cable, J. Duker, and J. Fujimoto, "Total retinal blood flow measurement with ultrahigh speed swept source/fourier domain oct," *Biomedical OpticsExpress*, vol. 2, no. 6, pp. 1539–1552, 2011.

[52] H. Ren, C. Du, and Y. Pan, "Cerebral blood flow imaged with ultrahigh-resolution optical coherence angiography and doppler tomography," *OpticsLetters*, vol. 37, no. 8, pp. 1388–1390, 2012.

[53] S. Yazdanfar, M. Kulkarni, and J. A. Izatt, "High resolution imaging of in vivo cardiac dynamics using color doppler optical coherence tomography," *OpticsExpress*, vol. 1, no. 13, pp. 424–431, 1997.

[54] R. M. Werkmeister, N. Dragostinoff, M. Pircher, E. Gtzinge, C. K. Hitzenberger, R. A. Leitgeb, and L. Schmetterer, "Bidirectional doppler fourier-domain optical coherence tomography for measurement of absolute flow velocities in human retinal vessels," *OpticsLetters*, vol. 33, no. 24, pp. 2967–2969, 2008.

[55] R. Wang and L. An, "Doppler optical micro-angiography for volumetric imaging of vascular perfusion in vivo," *OpticsExpress*, vol. 17, no. 11, pp. 8926–8940, 2009.

[56] B. White, M. Pierce, N. Nassif, B. Cense, B. Park, G. Tearney, B. Bouma, T. Chen, and J. de Boer, "In vivo dynamic human retinal blood flow imaging using ultra-high-speed spectral domain optical coherence tomography," *OpticsExpress*, vol. 11, no. 25, pp. 3490–3497, 2003.

[57] G. Liu, W. Qi, L. Yu, and Z. Chen, "Real-time bulk-motion-correction free doppler variance optical coherence tomography for choroidal capillary vasculature imaging," *OpticsExpress*, vol. 19, no. 4, pp. 3657–3666, 2011.

BIBLIOGRAPHY

[58] D. Apples and J. Sims, "Harold ridley and the invention of the intraocular lens," *Survey of Ophthalmology*, vol. 40, no. 4, pp. 279–292, 1996.

[59] N. E. Institute. (2011, January) Arch ophthalmol. [Online]. Available: http://www.nei.nih.gov/eyedata/pbd6.asp

[60] I. Ilev, "A simple confocal fibre-optic laser method for intraocular lens power measurement," *EYE*, vol. 21, no. 6, pp. 819–823, 2007.

[61] K. Hoffer, D. Calogero, R. Faaland, and I. Ilev, "Precise testing of the dioptric power accuracy of exact-power-labeled intraocular lenses," *J Cataract Refract Surg*, vol. 35, no. 11, pp. 1995–1999, 2009.

[62] Y. Nakano and K. Murata, "Talbot interferometry for measuring the focal length of a lens," *Applied Optics*, vol. 24, no. 19, pp. 3162–3166, 1995.

[63] D. SU and C. Chang, "A new technique for measuring the effective focal length of a thick lens or a compound lens," *Optical Communications*, vol. 78, no. 2, pp. 118–122, 1990.

[64] E. Keren, K. Kreske, and O. Kafri, "Universal method for determining the focal length of optical systems by moir deflectometry," *Applied Optics*, vol. 27, no. 8, pp. 1383–1385, 1988.

[65] D. Tognetto, G. Sanguinetti, P. Sirotti, P. Cecchini, I. Marucci, and E. Ballone,

"Analysis of the optical quality of intraocular lenses," *Investigative Ophthalmology and Visual Science*, vol. 45, no. 8, pp. 2682–2690, 2004.

[66] N. Norrby, L. Grossman, E. Geraghry, C. Kreiner, M. Mihori, and A. Parel, "Accuracy in determining intraocular lens dioptric power assessed by interlaboratory tests," *Journal of cataract and refractive surgery*, vol. 22, no. 7, pp. 983–987, 1996.

[67] W. Smith, *Modern Optical Engineering*. NY, USA: McGraw-Hill, 1990.

[68] M. Zhao, A. Kuo, and J. Izatt, "3d refraction correction and extraction of clinical parameters from spectral domain optical coherence tomography of the cornea," *Optics Express*, vol. 18, no. 9, pp. 8923–8936, 2010.

[69] S. Ortiz, D. Siedlecki, L. Remon, and S. Marcos, "Optical coherence tomography for quantitative surface topography," *Applied Optics*, vol. 48, no. 25, pp. 6708–6715, 2009.

[70] R. Zawadzki, C. Leisser, R. Leitgeb, M. Pircher, and A. Fercher, "Three-dimensional ophthalmic optical coherence tomography with a refraction correction algorithm," *Proceedings of SPIE*, vol. 5140, pp. 20–27, 2003.

[71] S. Ortiz, D. Sledleckl, I. Grulkowski, L. Remon, D. Pascual, M. Wojtkowski, and S. Marcos, "Optical distortion correction in optical coherence tomography

for quantitative ocular anterior segment by three-dimensional imaging," *Optics Express*, vol. 18, no. 3, pp. 2782–2796, 2010.

[72] A. V. adn D. Kane, W. WOod, and K. Peterson, "Common-path interferometer for frequency-domain optical coherence tomography," *Applied Optics*, vol. 42, no. 34, pp. 6953–6958, 2003.

[73] J. Kang, J. Han, X. Liu, K. Zhang, C. Song, and P. Gehlbach, "Endoscopic functional fourier domain common path optical coherence tomography for microsurgery," *IEEE Journal of Selected Topics Quantum Electron*, vol. 16, no. 4, pp. 781–792, 2010.

[74] Y. Mao, S. Chang, E. Murdock, and C. Flueraru, "Simultaneous dual-wavelength-band common-path swept-source optical coherence tomography with single polygon mirror scanner," *IEEE Journal of Selected Topics Quantum Electron*, vol. 36, no. 11, pp. 1990–1992, 2011.

[75] R. Leitgeb, W. Drexler, A. Unterhuber, B. Hermann, T. Bajraszewski, T. Le, A. Stingl, and A. Fercher, "Ultrahigh resolution fourier domain optical coherence tomography," *Optics Express*, vol. 12, no. 10, pp. 2156–2165, 2004.

[76] D. Stifter, D. A. Sanchis, E. Breuer, K. Wiesauer, P. Burgholzer, O. Hoglinger, E. Gotzinger, M. Pircher, and C. Hitzenberger, "Polarization-sensitive optical coherence tomography for material characterisation and testing," *Insight*, vol. 47, pp. 209–212, 2005.

[77] M. Shahidi, Z. Wang, and R. Zelkha, "Quantitative thickness measurement of retinal layers imaged by optical coherence tomography," *American Journal of Ophthalmology*, vol. 139, no. 6, pp. 1056–1061, 2005.

[78] J. G.Fujimoto and D. L. Farkas, *Biomedical Optical Imaging*. New York, USA: Oxford University, 2009.

[79] T. Dabbs and M. Glass, "Fiber-optic confocal microscope: Focon," *Applied Optics*, vol. 31, no. 16, p. 3030, 1992.

[80] D.-H. Kim, I. K. Ilev, and J. U. Kang, "Fiber-optic confocal microscopy using a 1.55 mm fiber laser for multimodal biophotonics applications," *IEEE Journal of Selective Topics in Quantum Electronics*, vol. 14, no. 1, pp. 82–87, 2008.

[81] D. H. Kim, I. K. Ilev, and J. U. Kang, "Advanced confocal microscope using single hollow-core photonic bandgap fibre design," *IEE Electronic Letters*, vol. 43, no. 11, pp. 608–609, 2007.

[82] A. Gmitro and D. Aziz, "Confocal microscopy through a fiber-optic imaging bundle," *Optics Letters*, vol. 18, no. 8, pp. 565–567, 1993.

[83] C. Liang, M. Descour, K. Sun, and R. Richards-Kortum, "Fiber confocal reflectance microscope (fcrm) for in-vivo imaging," *Optics Express*, vol. 9, no. 13, pp. 821–830, 2001.

[84] W. Gbel, J. N. D. Kerr, A. Nimmerjahn, and F. Helmchen, "Miniatured two-photon microscope based on a flexible coherent fiber bundle and a gradient-index lens objective," *Optics Letters*, vol. 29, no. 21, pp. 2521–2523, 2004.

[85] T. Xie, D. Mukai, M. B. S. Guo, and Z. Chen, "Fiber-optic-bundle-based optical coherence tomography," *Optics Letters*, vol. 30, no. 14, pp. 1803–1805, 2005.

[86] J. Han, X. Liu, C. Song, and J.U.Kang, "common path optical coherence tomography with fibre bundle probe," *ELectronics Letters*, vol. 45, no. 22, pp. 1110–1112, 2009.

[87] J. Han, J. Lee, and J.U.Kang, "Pixelation effect removal from fiber bundle probe based optical coherence tomography imaging," *Optics Express*, vol. 18, no. 7, pp. 7427–7439, 2010.

[88] J. Knittel, L. Schnieder, G. Buess, B. Messerschmidt, and T. Possner, "Endoscope-compatible confocal microscope using a gradient index-lens system," *Optics Communications*, vol. 188, no. 5-6, pp. 267–273, 2001.

[89] R. G. Cucu, M. W. Hathaway, A. G. Podoleanu, and R. B. Rosen, "Active axial eye motion tracking by extended range, closed loop opd-locked white light interferometer for combined confocal/en face optical coherence tomography imaging of the human eye fundus in vivo," *Proceedings of SPIE*, vol. 73721, 2009.

[90] D. S.Greenberg and J. N. Kerr, "Automated correction of fast motion artifacts

for two-photon imaging of awake animals," *Journal of Neuroscience Methods*, vol. 176, no. 1, pp. 1–15, 2009.

[91] K. Zhang, W. Wang, J. Han, and J. U. Kang, "A surface topology and motion compensation system for microsurgery guidance and intervention based on common-path optical coherence tomography," *IEEE Transaction on Biomedical Engineering*, vol. 56, no. 9, pp. 2318–2321, 2009.

[92] K. Venkateswaran, A. Roorda, and F. Romero-Borja, "Theoretical modeling and evaluation of the axial resolution of the adaptive optics scaning laser phthalmoscope," *Journal of Biomedical Optics*, vol. 9, no. 1, pp. 132–138, 2004.

[93] A. Ahmad, S. Adie, E. Chaney, U. Sharma, and S. Boppart, "Cross-correlation-based image acquisition technique for manually-scanned optical coherence tomography," *Optics Express*, vol. 17, no. 10, pp. 8125–8136, 2009.

[94] B. Becker, R. MacLachlan, and C. Riviere, "State estimation and feedforward tremor suppression for a handheld micromanipulator with a kalman filter," *IEEE/RSJ, International Conference on Intelligent Robots and Systems*, pp. 5160–6165, 2011.

[95] S. Boppart, B. Bouma, C. Pitris, G. Tearney, and J. Fujimoto, "Forward-imaging instruments for optical coherence tomography," *Optics Letters*, vol. 22, no. 21, pp. 1618–1620, 1997.

[96] W. Jung, J. Zhang, L. Wang, P. Wilder-Smith, Z. Chen, D. McCormick, and N. Tien, "Three-dimensional optical coherence tomography employing a 2-axis microelectromechanical scanning mirror," *IEEE Journal of Selected Topics on Quantum Electronics*, vol. 11, no. 4, pp. 806–810, 2005.

[97] S. Han, M. Sarunic, J. Wu, M. Humayun, and C. Yang, "Handheld forward-imaging needle endoscope for ophthalmic optical coherence tomography inspection," *Journal of Biomedical Optics*, vol. 13, no. 2, p. 020505, 2008.

[98] L. Huo, J. Xi, Y. Wu, and X. Li, "Forward-viewing resonant fiber-optic scanning endoscope of appropriate scanning speed for 3d oct imaging," *Optics Express*, vol. 18, no. 14, pp. 14 375–14 384, 2010.

[99] H. Park, C. Song, M. Kang, Y. Jeong, and K. Jeong, "Forward imaging oct endoscopic catheter based on mems lens scanning," *Optics Letters*, vol. 37, no. 13, pp. 2673–2675, 2012.

[100] X. Liu, Y. Huang, and J. U. Kang, "Distortion-free freehand-scanning oct implemented with real-time scanning speed variance correction," *Optics Letters*, vol. 20, no. 15, pp. 16 567–16 583, 2012.

[101] S. Singh and C. Riviere, "Physiological tremor during retinal microsurgery," *Proc. 28th Annual Conf. IEEE Eng. Med. Bio. Soc.*, pp. 171–172, 2002.

[102] N. Iftimia, B. Bouma, J. de Boer, B. Park, B. Cense, and G. Tearney, "Adaptive

ranging for optical coherence tomography," *Optics Express*, vol. 12, no. 17, pp. 4025–4034, 2004.

[103] G. Maguluri, M. Mujat, B. Park, K. Kim, W. Sun, N. Iftimia, R. Ferguson, D. Hammer, T. Chen, and J. de Boer, "Three dimensional tracking for volumetric spectral-domain optical coherence tomography," *Optics Express*, vol. 15, no. 25, pp. 16 808–16 817, 2007.

[104] Y. Huang, K. Zhang, J. Kang, D. Calogero, R. James, and I. Ilev, "Noncontact common-path fourier domain optical coherence tomography method for in vitro intraocular lens power measurement," *Journal of Biomedical Optics*, vol. 16, no. 12, p. 126005, 2011.

[105] K. Tan, M. Mazilu, T. Chow, W. Lee, K. Taguchi, B. Ng, W. Sibbett, C. Herrington, C. Brown, and K. Dholakia, "In-fiber common-path optical coherence tomography using a conical-tip fiber," *Optics Express*, vol. 17, no. 4, pp. 2375–2380, 2009.

[106] K. Zhang and J. Kang, "Common-path low-coherence interferometry fiber-optic sensor guided micro-incision," *Journal of Biomedical Optics*, vol. 16, no. 9, p. 095003, 2011.

[107] C. Song, P. Gehlbach, and J. U. Kang, "Active tremor cancellation by a smart handheld vitreoretinal microsurgical tool using swept source optical coherence tomography," *Optics Express*, vol. 20, no. 21, pp. 23 414–23 421, 2012.

[108] J. Ha, M. Shishkov, M. Colice, W. Oh, H. Yoo, L. Liu, G. Tearney, and B. Bouma, "Compensation of motion artifacts in catheter-based optical frequency domain imaging," *Optics Express*, vol. 18, no. 11, pp. 11 418–11 427, 2010.

[109] J. Lee, V. Srinivasan, H. Radharishnan, and D. A. Boas, "Motion correction for phase-resolved dynamic optical coherence tomography imaging of rodent cerebral cortex," *Biomedical Optics Express*, vol. 19, no. 22, pp. 21 258–21 270, 2012.

[110] E. Swanson, J. Izatt, M. Hee, D. Huang, C. Lin, J. Schuman, C. Puliafito, and J. Fujimoto, "In-vivo retinal imaging by optical coherence tomography," *Optics Letters*, vol. 18, no. 21, pp. 1864–1866, 2012.

[111] M. Kraus, B. Potsaid, M. Mayer, R. Bock, B. Baumann, J. Liu, J. Hornegger, and J. Fujimoto, "Motion correction in optical coherence tomography volumes on a per a-scan basis using orthogonal scan patterns," *Bimedical Optics Express*, vol. 3, no. 6, pp. 1182–1199, 2012.

[112] D. Duncan and S. Kirkpatrick, "Processing algorithms for tracking speckle shifts in optical elastography of biological tissues," *Journal of Biomedical Optics*, vol. 6, no. 4, pp. 418–426, 2001.

[113] R. McLaughlin, B. Quirk, A. Curatolo, R. W. Kirk, L. Scolaro, D. Lorenser, P. Robbins, B. Wood, C. Saunders, and D. Sampson, "Imaging of breast cancer

with optical coherence tomography needle probes: feasibility and initial results," *IEEE Journal of Selected Topics on Quantum Electronics*, vol. 18, no. 3, pp. 1184–1191, 2012.

[114] D. Lorenser, X. Yang, and D. Sampson, "Ultrathin fiber probes with extended depth of focus for optical coherence tomography," *Optics Letters*, vol. 37, no. 10, pp. 1616–1618, 2012.

[115] V. Roger, A. Go, D. Lloyd-Jones, E. Benjamin, J. Berry, and W. B. et al, "Heart disease and stroke statistics–2012 update: A report from the american heart association," *Circulation*, vol. 125, no. 1, pp. e2–e220, 2012.

[116] "Beneficial effect of carotid endarterectomy in symptomatic patients with high-grade carotid stenosis. north american symptomatic carotid endarterectomy trial collaborators," *The New England Journal of Medicine*, vol. 325, no. 7, pp. 445–453, 1991.

[117] "Endarterectomy for asymptomatic carotid artery stenosis. executive committee for the asymptomatic carotid atherosclerosis study," *Journal of the American Medical Association*, vol. 273, no. 18, pp. 1421–1428, 1995.

[118] P. Rothwell, J. Slattery, and C. Warlow, "A systematic comparison of the risks of stroke and death due to carotid endarterectomy for symptomatic and asymptomatic stenosis." *Stroke*, vol. 27, no. 2, pp. 266–269, 1996.

BIBLIOGRAPHY

[119] M. Burnett, S. Stein, S. Sonnad, and E. Zager, "Cost-effectiveness of intraoperative imaging in carotid endarterectomy," *Neurosurgery*, vol. 57, no. 3, pp. 478–485, 2005.

[120] T. Riles, A. Imparato, G. Jacobowitz, P. Lamparello, G. Giangola, and M. A. et al, "The cause of perioperative stroke after carotid endarterectomy," *Journal of Vascular Surgery*, vol. 19, no. 2, pp. 206–214, 1994.

[121] C. Rockman and E. Halm, "Intraoperative imaging: Does it really improve perioperative outcomes of carotid endarterectomy?" *Journal of Vascular Surgery*, vol. 20, no. 4, pp. 236–243, 2007.

[122] C. Lee, Y. Jung, H. Yang, Y. Son, and S. Lee, "An innovative method for detecting surgical errors using indocyanine green angiography during carotid endarterectomy: A preliminary investigation," *Acta Neurochirurgica*, vol. 154, no. 1, pp. 67–73, 2012.

[123] I. Jang, B. BOuma, D. Kang, S. Park, S. Park, and K. S. et al, "Visualization of coronary atherosclerotic plaques in patients using optical coherence tomography: Comparison with intravascular ultrasound," *Journal of the American College of Cardiology*, vol. 39, no. 4, pp. 604–609, 2002.

[124] J. Johnson, K. Carson, H. Williams, S. Karanam, A. Newby, and G. A. et al, "Plaque rupture after short periods of fat feeding in the apolipoprotein e-

knockout mouse: Model characterization and effects of pravastatin treatment," *Circulation*, vol. 111, no. 11, pp. 1422–1430, 2005.

[125] Y. Nakashima, A. Plump, E. Raines, J. Breslow, and R. ROss, "Apoe-deficient mice develop lesions of all phases of atherosclerosis throughout the arterial tree," *Arteriosclerosis and Thrombosis*, vol. 14, no. 1, pp. 133–140, 1994.

[126] J. Kang, Y. Huang, K. Zhang, Z. Ibrahim, W. A. Lee, G. Brandacher, and P. Gelhbach, "Real-time three-dimensional fourier-domain optical coherence tomography video image guided microsurgeries," *Journal of Biomedical Optics*, vol. 17, no. 8, pp. 081 403–1, 2012.

[127] S. Tahara, T. Morooka, Z. Wang, H. Bezerra, A. Rollins, and D. S. et al, "Intravascular optical coherence tomography detection of atherosclerosis and inflammation in murine aorta," *Arteriosclerosis, Thrombosis, and Vascular Biology*, vol. 32, no. 5, pp. 1150–1157, 2012.

[128] I. Jang, G. Tearney, B. MacNeill, M. Takano, F. Moselewski, and N. I. et al, "In vivo characterization of coronary atherosclerotic plaque by use of optical coherence tomography," *Circulation*, vol. 111, no. 12, pp. 1551–1555, 2005.

[129] M. DeBakey, "Successful carotid endarterectomy for cerebrovascular insufficiency. nineteen-year follow-up," *Journal of the American Medical Association*, vol. 233, no. 10, pp. 1083–1085, 1975.

[130] D. Samson, H. Batjer, G. Bowman, L. Mootz, W. Krippner, and Y. M. et al, "A clinical study of the parameters and effects of temporary arterial occlusion in the management of intracranial aneurysms," *Neurosurgery*, vol. 34, no. 1, pp. 22–28, 1994.

[131] H. Yabushita, B. Bouma, S. Houser, H. Aretz, I. Jang, and K. S. et al, "Characterization of human atherosclerosis by optical coherence tomography," *Circulation*, vol. 106, no. 13, pp. 1640–1645, 2002.

[132] G. Ughi, T. Adriaenssens, W. Desmet, and J. DHooge, "Fully automatic three-dimensional visualization of intravascular optical coherence tomography images: Methods and feasibility in vivo," *Biomedical Optics Express*, vol. 3, no. 12, pp. 3291–3303, 2012.

[133] D. Perlmutter and A. Rhoton, "Microsurgical anatomy of the anterior cerebral-anterior communicating-recurrent artery complex," *Journal of Neurosurgery*, vol. 45, no. 3, pp. 259–272, 1976.

[134] B. Hoh, W. Curry, B. Carter, and C. Ogilvy, "Computed tomographic demonstrated infarcts after surgical and endovascular treatment of aneurysmal subarachnoid hemorrhage," *Acta Neurochirurgica.*, vol. 146, no. 11, pp. 1177–1183, 2004.

[135] A. Rothwell, "Alexis carrel: innovator extraordinaire," *Journal of Perioperative Practice*, vol. 21, no. 2, pp. 73–76, 2011.

[136] E. I. Chang, M. G. Galvez, J. P. Glotzbach, C. Hamou, S. Elftesi, C. Rappleye, K. Sommer, J. Rajadas, O. J. Abilez, G. Fuller, M. Longaker, and G. Gurtner, "Vascular anastomosis using controlled phase transitions in poloxamer gels," *Nature Methods*, vol. 17, no. 9, pp. 1147–1152, 2011.

[137] L. Levin and D. Erdman, "Primary and secondary microvascular reconstruction of the upper extremity," *Hand Clinics*, vol. 17, no. 3, pp. 447–455, 2001.

[138] C. Y. Ahn, W. W. Shaw, S. Berns, and B. Markowitz, "Clinical experience with the 3m microvascular coupling anastomotic device in 100 free-tissue transfers," *Plastic and Reconstructive Surgery*, vol. 93, no. 7, pp. 1481–1484, 1994.

[139] R. Sucher, C. H. Lin, R. Zanoun, K. Atsina, M. Weinstock, B. Pulikkotil, S. Schneeberger, X. Zheng, J. Pratschke, W. A. Lee, and B. Gerald, "Mouse hind limb transplantation: a new composite tissue allotransplantation model using nonsuture supermicrosurgery," *Transplantation*, vol. 90, no. 12, pp. 1374–1380, 2010.

[140] J. Chen, M. Manning, A. Frazier, J. Jeudy, and C. S. White, "Ct angiography of the cardiac valves: normal, diseased, and postoperative appearances," *RadioGraphics*, vol. 29, no. 5, pp. 1393–1413, 2009.

[141] W. Swartz, R. Izuierdo, and M. Miller, "Implantable venous doppler microvascular monitoring: laboratory investigation and clinical results," *Plastic and Reconstructive Surgery*, vol. 93, no. 1, pp. 152–163, 1994.

[142] J. Ehlers, Y. Tao, S. Farsiu, R. Maldonado, J. Izatt, and C. Toth, "Integration of a spectral domain optical coherence tomography system into a surgical microscope for intraoperative imaging," *Investigative Ophthalmology Visual Science*, vol. 52, no. 6, pp. 3153–3159, 2011.

[143] A. Eckly, B. Hechler, M. Freund, M. Zerr, J.-P. Cazenave, F. Lanza, P. Mangin, and C. Gachet, "Mechanisms underlying fecl3-induced arterial thrombosis," *Journal of Thrombosis and Haemostasis*, vol. 9, no. 4, pp. 779–789, 2011.

[144] X. Liu, Y. Huang, J. Ramella-Roman, S. Mathews, and J. Kang, "Quantitative transverse flow measurement using optical coherence tomography speckle decorrelation analysis," *Optics Letters*, vol. 38, no. 5, pp. 805–807, 2013.

[145] O. Zhernovaya, V. Tuchin, and M. Leahy, "Blood optical clearing studied by optical coherence tomography," *Journal of Biomedical Optics*, vol. 18, no. 2, p. 026014, 2013.

Vita

Yong Huang was born in Jiangsu Province, P.R. China on September 4th, 1987. He received the Sc. B. degree in Physics from Peking University, P.R.China in 2009 and enrolled in the Electrical and Computer Engineering Ph.D. program at Johns Hopkins University in 2009. He received National Scholarship from China Scholarship Council in 2009 for four years. He worked as a graduate research assistant in the biophotonics lab and his research focuses on Fourier domain optical coherence tomography (FDOCT) and its clinical application and high performance computing using graphics processing unit.He also worked as a Oak Ridge Institute for Science and Education (ORISE) research fellow to study the method of using common path OCT in in-vitro intraocular lens power measurement. center for devices and radiological health (CDRH) at U.S. Food and Drug Administration, Silver Spring from December,2010 to October, 2011. He is a student member of the optical society of America (OSA) and the international society for optics and photonics (SPIE).